UNIVERSITY OF CALIFORNIA
Los Angeles

Stabilization, gate control and ultrafast dynamics of microresonator optical frequency combs

A dissertation submitted in partial satisfaction
of the requirements for the degree
Doctor of Philosophy in Electrical Engineering

by

Abhinav Vinod

2021

ABSTRACT OF THE DISSERTATION

Stabilization, gate control and ultrafast dynamics of microresonator optical frequency combs

by

Abhinav Vinod
Doctor of Philosophy in Electrical Engineering
University of California, Los Angeles, 2021
Professor Chee Wei Wong, Chair

An optical frequency comb (OFC) is a light source whose spectrum comprises of several sharp, equally spaced lines. They were originally developed more than two decades ago to simplify the measurement of optical frequencies in terms of precise atomic standards. OFC technology has progressed remarkably since the first demonstration and OFCs are now the cornerstones of modern-day frequency metrology, precision spectroscopy, astronomical observations, ultrafast optics and quantum information. While the current bulk mode-locked laser frequency comb has had great success in extending the scientific frontier, its use in real-world applications beyond the laboratory setting remains an unsolved challenge due to the relatively large size, weight and power consumption. Recently microresonator-based frequency combs have emerged as a candidate solution with chip-scale implementation and scalability. Microresonator platforms for comb generation are the subject of significant research efforts, which are primarily focused into three areas – comb stabilization, control over comb state generated and evolution paths and study of the comb formation dynamics. In this dissertation we focus on each of these three different areas. First, a novel internal phase-stabilized frequency microcomb that does not require nonlinear second-third harmonic generation nor optical external frequency references is demonstrated. It is shown that the optical frequency can be stabilized by control of two internally accessible parameters: an intrinsic comb offset ξ and the comb spacing f_{rep}. Second, direct electrical control of microresonator parameters is achieved by coupling the gate-tunable optical conductivity of graphene to a silicon nitride photonic microresonator, and modulating its second- and higher-order chromatic dispersions by altering the Fermi level. This is then used to produce charge-tunable primary comb lines from 2.3 terahertz to 7.2 terahertz, coherent Kerr frequency combs, controllable Cherenkov radiation and controllable soliton states, all in a single microcavity. In addition, voltage-tunable transitions between soliton crystal states with defects with defects is demonstrated and mapped via ultrafast second-harmonic optical autocorrelation. Finally, novel ultrafast spectral and temporal measurement techniques are characterized and used to directly capture snapshots of the microresonator field at resolutions of less than 1 ps. These methods are applied to study spectral energy transfer, complex breathing dynamics, collective motion in soliton ensembles and the occurrence of extreme events from a chaotic background.

The dissertation of Abhinav Vinod is approved.

Wes Campbell

Sudhakar Pamarti

Mau-Chung Frank Chang

Chee Wei Wong, Committee Chair

University of California, Los Angeles

2021

To my parents & brother . . .

TABLE OF CONTENTS

LIST OF FIGURES

LIST OF TABLES

ACKNOWLEDGMENTS

I would like to express my sincere gratitude to Professor Chee Wei Wong for supervising my PhD. Professor Wong was a remarkable advisor, and his passion and energy for science has inspired me throughout my time working with him. In addition, I am also indebted to Professor Wong as he has always pushed me to look for novel ideas to solve the intricate problems during my research.

My special thanks go to Dr. Shu-Wei Huang for teaching me the ropes of optics experiments in general and microcomb experiments in particular. I spent many many hours discussing ideas and experiments with him and I will always be grateful to have had the opportunity to work with such an excellent scientist. I would also like to thank Dr. Wenting Wang for sharing his knowledge and expertise regarding nonlinear optical systems and providing help and advice in several measurements. We also spent time discussing my research and future and his advice has proven invaluable several times over. I am glad to have met and worked with him over these several years. I am also thankful to Futai Hu, whom I worked with for this past year. Our interests in various subjects aligned most of the time and our discussions always inspired me to delve deeper into the subject and understand things on a more fundamental level. I've learned much during our collaboration and am glad to have worked with him, as a colleague and and as a friend.

I am also thankful to Dr. James Mcmillan for helping me with my experiments, his remarkable grasp of the subject and excellent engineering skills, lead me to ask for his advice and help when I hit roadblocks. His insight and expertise have been very helpful in nearly every problem I've stumbled on. I would also like to thank Jaime Flor Flores for being a great friend throughout my PhD and for inspiring me with his extensive knowledge in a wide range of topics. Thanks also to Hao Liu, Dr. Jinghui Yang, Dr. Jinkang Lim, Prof. Baicheng Yao, Kai-Chi Chang, Xiang Chen, Dr. Yujin Cho, Zhangji Zhao, Jin Ho Kang, Murat Sarihan, Talha Yerebakan, Jiahui Huang, Dr. Wei Liu, Dr. Hangbo Yang, Tristan Melton, Hyunpil Boo and the other group members I worked with over the years for always being available and sharing their knowledge and thoughts regarding my research work. It was a wonderful experience to work with such talented scientists and engineers.

I am also grateful to Li-Yang Chen from Professor Ken Yang's group for several discussions and collaborations over the years.

I would like to thank Professor Wes Campbell, Professor Frank Chang and Professor Sudhakar Pamarti for serving on my committee and their invaluable advice. I would also like to thank Deeona Columbia and Ryo Arreola, for helping out during the entirety of my PhD. I also could not imagine finishing this without the support of my friends, they've been with me through hard times and good times, and I am deeply grateful to them. Finally, I would like to thank my parents, for their love and support throughout my life. I owe this and every other success in my life to them. Without their unfailing support this achievement would not be possible. I would also like to thank my younger brother, for all the love and support and for being a true friend.

VITA

2010–2014	B.E. (Electrical Engineering), Indian Institute of Technology (IIT), Bombay, India.
2014–2016	M.S. (Electrical Engineering), University of California, Los Angeles, USA.
2017	Ph.D. Candidate (Electrical Engineering), University of California, Los Angeles, USA.

CHAPTER 1

Introduction

An optical frequency comb (OFC) is a light source whose spectrum usually comprises 10^3 to 10^5 harmonically related optical lines. Both the spectral and temporal aspects of the comb find a multitude of diverse applications. As an example, their remarkable functionality in providing a phase-coherent link bridging microwave and optical frequencies enables their use in precision optical metrology, optical frequency division and optical frequency synthesizers. In the time domain they function as sources for ultrashort pulses spaced at precise intervals and find use in spectroscopy, ranging and coherent control in field dependent processes. More broadly they form a cornerstone for scientific breakthroughs in precision metrology, spectroscopy, time-frequency transfer, molecular fingerprinting and quantum information.

While the current bulk mode-locked laser frequency comb has had great success in extending the scientific frontier, its use in real-world applications beyond the laboratory setting remains an unsolved challenge due to the relatively large size, weight and power consumption. To this end, microresonator based OFCs have emerged as a candidate solution with chip-scale implementation and scalability. In particular planar ring cavities fabricated in CMOS compatible materials are attractive due to their robust coupling mechanism, small mode volume and potential for electronic-photonic integration. In this dissertation we use microring cavities fabricated in Si3N4, a CMOS integrable platform. The focus of this dissertation will be on novel ways to stabilize OFCs, control resonator parameters, and observe ultrafast comb dynamics. The thesis is thus organized as follows :

Chapter 2, describes an approach to stabilize optical combline frequencies of appropriately generated comb statescomb stabilization scheme using only internally accessible comb-parameters such as f_{rep} and offset frequency ξ. Existence of microcombs with only one set of primary comb lines, critical for the new stabilization method, is a consistent property of these nonlinear microresonators and have been found in devices across multiple chipsets with very different dispersion, Q and f_{rep}. It is further shown that the frequency microcomb has frequency instability of 2×10^{-11} at 20- second gate time, bounded by the external microwave reference. An avenue in which this method might prove useful, namely in the generation of low noise microwaves is discussed and a proof-of-principle experiment showing this is demonstrated.

Chapter 3, demonstrates the gated intracavity tunability of graphene-based optical frequency combs, by coupling the gate-tunable optical conductivity to a silicon nitride photonic microresonator, thus modulating its second- and higher-order chromatic dispersions by altering the Fermi level. Preserving cavity quality factors up to 10^6 in the graphene-based comb, a dual-layer ion-gel-gated transistor to tune the Fermi level of graphene across the range 0.45-0.65 electronvolts, under single-volt-level control is implemented. This is used to produce charge-tunable primary comb lines from 2.3 terahertz to 7.2 terahertz, coherent Kerr frequency combs, controllable Cherenkov radiation and controllable soliton states, all in a single microcavity. Further, voltage-tunable transitions from periodic soliton crystals to crystals with defects are demonstrated and mapped by our ultrafast second-harmonic optical autocorrelation.

Chapter 4, utilizes a novel technique, parametric spectro-temporal analysis to study and characterize various ultrafast phenomenon in Kerr microresonators. This method makes it possible to capture capture spectral features as low as -30 dBm and provides a spectral resolution of over 22 pm. This method is used to study in detail, the occurrence, spectral characteristics and statistics of extreme events in chaotic comb states and in the chaotic transition to stable low-noise breather combs. The comb line dependent breathing intensity and relative phase is experimentally measured and a further study of this could elucidate the complex energy transfer mechanisms in frequency combs generated in cavities with mode interaction. In addition, for the first time, the transition between different breathing frequency combs and measured the rapid loss of power followed by bursts of revival during the transition process is mapped out.

In Chapter 5, the collective dynamics of soliton crystal ensembles is studied for the first time in a Kerr-microresonator platform. The observed spatially breathing crystals, are distinct in comparison to normal breather solitons and arise from the relative motion of individual solitons in relation to the ensemble. The above mentioned soliton crystals are generated via deterministic approaches in different microresonators. It is also show that the breathing phase of two solitons near the defects can be controlled by engineering multiple mode-crossing points. A real-time FWM based time-lens is also used to map out cavity field evolution during breathing cycles.

in Chapter 6, a novel panoramic-reconstruction temporal imaging (PARTI) system is used to study the evolution of the intracavity field in the chaotic regime. Specifically, rogue events in microresonators are studied, which allow for an in-depth analysis of field evolution on the length scale of the pumped cavity, which by its nature is much shorter than a fiber cavity. The system achieves a high temporal resolution along with a long temporal recording length simultaneously, which allows for a comprehensive understanding of these intriguing ultrafast optical phenomena that evolve over a timescale much longer than their fine temporal details. Rogue event persistence in 19, 66, and 90 GHz microresonators is recorded and the distribution of RW persistence in the cavity is studied and correlated to RW intensity.

CHAPTER 2

Frequency microcomb stabilization via dual-microwave control

2.1 Introduction

Phase-stabilized optical frequency combs, with the multitude of coherent and stable spectral lines, bridges the research frontiers in ultrastable laser physics and ultrafast optical science [1–6]. Phase stabilization requires two-dimensional feedback control on the comb's intrinsic two degrees-of-freedom, the comb spacing and one of the comb line optical frequencies. While the comb spacing can be readily measured with a high-speed photodetector, assessment of the comb line optical frequency fluctuations often requires non-trivial and/or nonlinear processes. One approach is to compare the optical frequency comb (OFC) against an external optical reference, and previous phase stabilization of Kerr frequency comb has been predominantly demonstrated with schemes based on this approach [7, 8]. The requirement of an external optical reference, however, limits the achievable compactness of Kerr frequency comb and impairs its integration of chip-based photonics with electronics. Another approach is to devise a nonlinear optical interferometry which reveals the optical frequency instability through the so-called carrier-envelope-offset frequency f_{ceo}, an internal OFC property resulting from difference in the phase and group velocities [9]. Knowledge of f_{rep} and f_{ceo} fully determines the optical frequencies of a mode-locked laser-based OFC, and phase locking them to stable microwave references ensures the intricate stability of the optical frequency synthesizer. Figure 2.1a shows the schematic of a state-of-the-art *f-2f* nonlinear interferometer widely adopted to measure the f_{ceo} [10]. First, the output pulse from a mode-locked laser is spectrally broadened in a highly nonlinear photonic crystal fiber such that its optical spectrum spans more than an octave. Then the octave-level spectrum is separated into two parts: the lower-frequency end undergoes second-harmonic generation in a nonlinear crystal while the higher-frequency end only experiences free-propagation. Finally, the two beams are put together in both transverse and longitudinal coordinates for them to interfere on a photodetector and generate a beat note at f_{ceo}. For the nonlinear processes to work properly, spectral broadening in particular, few-cycle pulses with peak powers in the 10-kW level are required [6].

While the microresonator-based OFC, or Kerr frequency microcomb, is approaching the performance of mode-locked laser-based OFC in many aspects [11–35], its output pulse duration and peak power are still lower by orders of magnitude. Application of *f-2f* and *2f-3f* nonlinear interferometer technique to the Kerr frequency comb is thus challenging and power demanding. The pulse duration can potentially be improved by finer dispersion engineering, but the peak power is fundamentally limited by the bandwidth-efficiency product [36] and the large comb spacing. On the other hand, the 10 to 100 GHz comb spacing of Kerr frequency comb is considered an advantageous feature for applications like coherent Raman spectroscopy [37], optical arbitrary waveform generation [38], high bandwidth telecommunication [39, 40], and astrospectrograph calibration [41–43]. In a recent pioneering demonstration of self-referenced Kerr frequency comb where *f-2f* nonlinear interferometer technique is adopted [27, 44], a hybrid approach was utilized with two interlocking combs, a THz spacing comb with dispersive waves at f and *2f* is used to calculate f_{ceo} while a second relatively closely spaced comb is simultaneously generated to measure f_{rep}. This approach is successful, however, the experimental setup includes several components including lasers at different wavelengths, frequency shifters and a thulium amplifier. In addition, in recent years there have been several experiments attempting to facilitate stabilization and reduce the size, weight and power (SWaP) impact of peripherals via more compact control [45], electro-optic modulation of large spacing combs [46], and micromachined atomic cells [47, 48].

In this work we attempt to extend current stabilization techniques using the unique generation mechanism of Kerr frequency microcombs. We demonstrate comb stabilization using only internal degrees of freedom in a single resonator with no external nonlinear processes and achieve an Allan deviation (AD) of 2×10^{-11} at a 20-second gate time for the stabilized comblines. After the stabilization of f_{rep}, we show that ξ resembles f_{ceo} in gauging the optical frequency instability without the need of an external optical reference. ξ is specifically sensitive to the fluctuation in pump frequency, which is at the same time the 0th comb line frequency. Phase locking of f_{rep} and ξ to low noise microwave oscillators thus guarantees the optical frequency stability of the microcomb. This method has potential for chip-scale integration, while circumventing the need for a large number of peripherals, thereby preserving the key SWaP advantage of frequency microcombs.

2.2 Breather comb generation

Kerr comb formation in the microresonator is illustrated in Figure 2.1b. The intracavity power is gradually increased by decreasing the frequency of an initially blue-detuned pump. As coupled cavity power crosses a threshold, modulation instability (MI) gain dominates over cavity loss forming primary comb lines via degenerate four-wave mixing (FWM). The frequency difference between the primary lines (Δ) is determined by dispersion, pump power and mode-interaction. In general however, Δ need not be an integer multiple of the cavity repetition rate f_{rep}. Thus, on formation of subcombs with secondary comb lines spaced by f_{rep}, around the primary lines, the generated comb exhibits an intrinsic offset frequency ξ, that may be directly detected by a photodetector [13–16]. While in general the comb state can be complex with multiple offset beats or chaotic (see Section A.1), with detuning and pump power control it is possible to generate just a single set of primary lines (unique Δ) and therefore a microcomb with a well-defined ξ uniquely. Figure 2.1c shows the optical spectrum of such a comb in the C-band, the particular phase locked breather state generated necessitates a modulated comb spectrum since we do not have full merging of the subcombs. Figure 2.1d zooms in to a 3 nm bandwidth showing the spacing Δ and the merging of subcombs. In Figure 2.1e, we see the resultant RF beat notes at ξ = 523.35 MHz and f_{rep} = 17.9 GHz, as detected by a high speed photodetector. We further confirm the existence of only one primary comb family and the uniformity of f_{rep} and ξ across the comb by measuring the beat notes at different spectral segments with a tunable 0.22-nm bandpass filter, in Figure 2.1f and 2.1g respectively. The breather state is stable and exists across a range of powers and detuning. In our specific instance, we see a stable breather over a detuning span of over a GHz and with a power tolerance of 1 dB. In addition to being of use in locking, such phase-locked breather Kerr combs have also recently come under some scrutiny for their rich cavity dynamics [49].

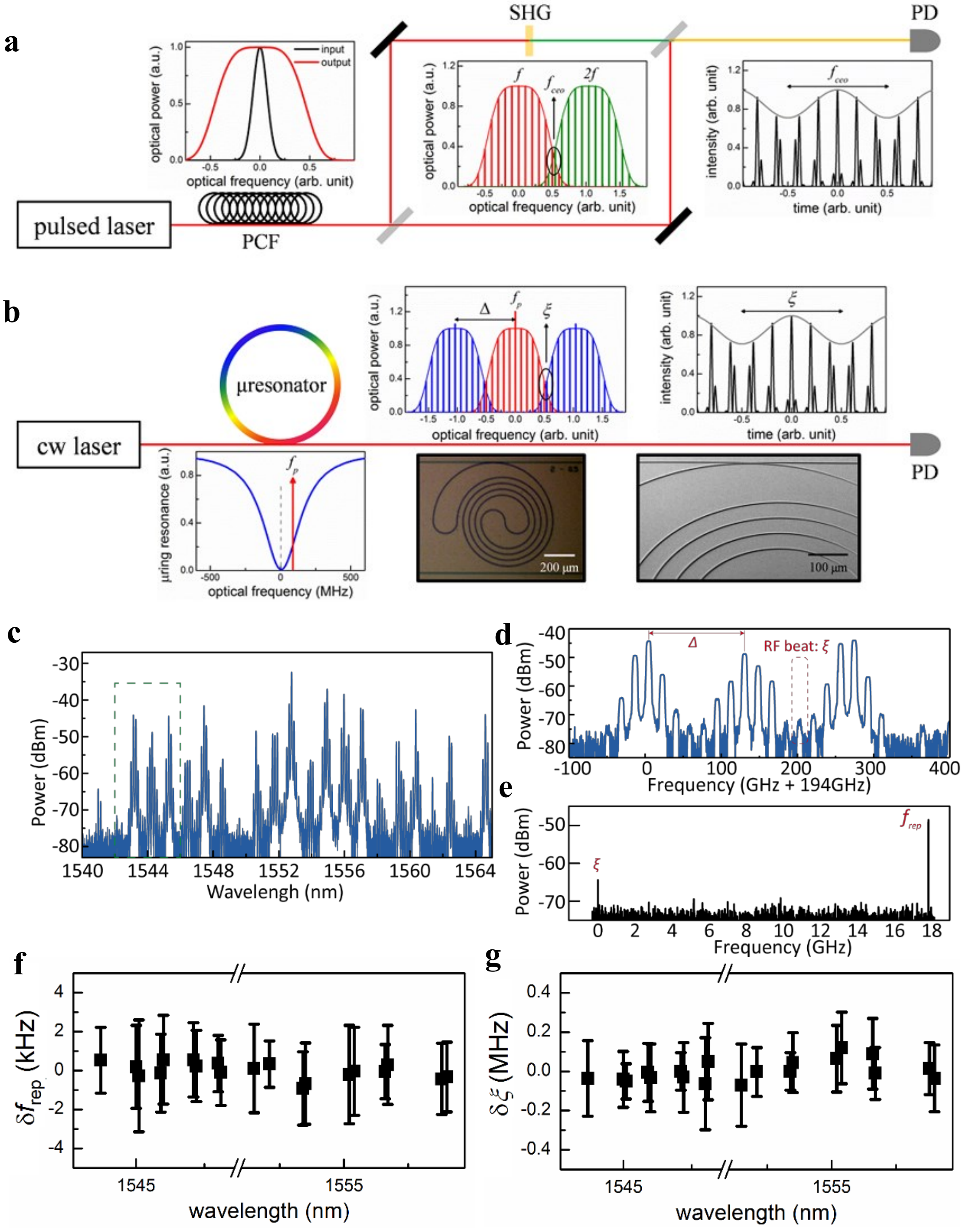

Figure 2.1. **(a)** Schematic of the current f-$2f$ nonlinear interferometry to measure f_{ceo}. By comparing the higher-frequency comb segment and the second-harmonic of the lower-frequency segment, a beat note at f_{ceo} with sufficient signal-to-noise-ratio (SNR) is generated on a photodetector (PD). This often requires comb spectral broadening in a highly nonlinear fiber and/or a broad octave-level comb span. **(b)** The unique generation mechanism of frequency microcombs provides an alternative full stabilization route that does not require external nonlinear processes. Modulation

instability and four-wave mixing then generates the initial comb lines with Δ spacing, and subsequently secondary lines with f_{rep} spacing. Often, Δ is not an integer multiple of f_{rep}. The frequency microcomb therefore has an offset frequency ξ innately. As elaborated later, ξ resembles f_{ceo} in directly gauging the optical frequency instability. **(c)** Example frequency microcomb spectrum showing subcombs around primary lines yet to fully merge **(d)** Primary comb lines are formed with a spacing (Δ) of 1.1 nm and then generate overlapping subcombs **(e)** Electrical spectrum measures two distinct beat notes of f_{rep} = 17.9 GHz and ξ = 523.35 MHz, confirming the presence of a unique ξ **(f)** and **(g)** Free-running change in f_{rep} and ξ at different spectral regions are measured to be the same within error bars of $\approx$ 2 kHz and $\approx$ 200 kHz, respectively. At wavelengths where the beat notes have SNR higher than 10 dB (100 kHz RBW), 10 measurements are taken to determine the mean values of the comb spacing and offset frequencies. Measurement error bar is the peak-to-peak deviation from 10 measurements.

2.3 Characterization of proposed stabilization technique

Figure 2.2a depicts the frequency microcomb setup for stabilization [50]. Detailed descriptions of the chip fabrication and measurement setup are included in the Sections A.2 and 2.7 respectively. The Si_3N_4 microresonator is fabricated with CMOS-compatible processes and the spiral design ensures that the relatively large resonator fits into a tight field-of-view to avoid additional cavity losses introduced by photomask stitching and discretization errors. The resonator has a quality factor *Q* of 1.2 million intrinsically in the transverse-electric mode polarization, with near critical coupling for a 600,000 loaded *Q*. The waveguide width of 2m (725 nm height) allows for significant mode overlap between the fundamental and first order TE modes, and thereby the resonator exhibits periodic mode-interaction spaced by 4 nm. Free-space to chip coupling is implemented by a 600 μm long adiabatic coupler which allows, with our coupling free-space lens, a total chip coupling loss not more than 5.5 dB. In order to suppress environmental temperature fluctuations from the microcomb, the resonator chip is placed on a thermoelectric cooler for thermal control and placed in a box with two layers of thermal foam insulation. We note that the box is not entirely sealed, which gives little convective currents within the box or between the external environment and the box, leading to some temperature fluctuations. The entire setup including the optics is then placed in an acrylic chamber. Acoustic noise is dampened by placing the enclosed setup on a sorbothane sheet and then placing it on an active optical table.

The comb spacing of 17.9 GHz is directly measurable by sending the output to a high-speed photodetector. The comb spacing is then phase locked and stabilized to a microwave oscillator by controlling the pump power through a fiber electro-optic modulator (primary loop) and either the gain of the erbium-doped fiber amplifier (slow loop marked in yellow) or temperature of the chip mount (slow loop marked in green). Quality of the f_{rep} stabilization is detailed in the Section 2.7. Of note, the free-running offset frequency ξ is much noisier than the comb spacing f_{rep} due to the additional multiplier in the constitutive equation that is proportional to the spacing between the primary comblines and pump (Δ) divided by the repetition rate (the brackets in Eq. 2.1 correspond to the floor operation):

$$\xi = \Delta - \left\lfloor \frac{\Delta}{f_{rep}} \right\rfloor f_{rep} \tag{2.1}$$

To this end, f_{rep} stabilization loop is always engaged before measurements on the offset frequency is conducted. Comparison between free-running and post-f_{rep} stabilization ξ is included in the Section 2.7. As the offset frequency is localized to the spectral region where secondary comb lines overlap, a 0.22 nm optical bandpass filter is used to select the overlapped comb lines around 1553.5 nm for detection. The beat note is thus improved to 50 dB above the noise floor with a resolution bandwidth (RBW) of 10 kHz, sufficient for a reliable feedback stabilization (more than 45 dB with 10 kHz RBW). The offset frequency is divided by 15 before it is phase locked and stabilized to a microwave synthesizer. The pre-scaling reduces the phase fluctuation, while preserving the instability of the oscillator frequency, and thus it makes the ξ phase-locked loop more robust against noise. The high-bandwidth feedback on ξ is achieved by direct current modulation of the external cavity diode laser (ECDL), and the slow feedback is done through piezoelectric transducer control of the ECDL. We heterodyne beat our Kerr frequency comb with a stabilized fiber frequency comb (FFC) to measure out-of-loop stability.

All microwave oscillators and frequency counters are commonly referenced to a rubidium-disciplined crystal oscillator with a 5×10^{-12} frequency instability at 1 second integration time. Kerr frequency comb generation mechanism can be described by the nonlinear Schrödinger equation and the cavity boundary condition [51–53]:

$$\frac{\partial E^n(z,t)}{\partial z} = -\frac{\alpha}{2}E^n(z,t) - i\frac{\beta_2}{2}\frac{\partial^2 E^n(z,t)}{\partial t^2} + i\gamma|E^n(z,t)|^2 E^n(z,t) \tag{2.2}$$

$$E^{n+1}(0,t) = \sqrt{1-T}E^n(L,t)\exp(i\varphi_0) + \sqrt{T}E_i \tag{2.3}$$

where $E^n(z,t)$ is the electric field envelope function at the n^{th} cavity round-trip, *z* is the propagation, *t* is the retarded time, α is cavity round-trip loss, β_2 is the group velocity dispersion (GVD), γ is the nonlinear coefficient, *T* is transmission coefficient of the coupler, and φ_0 is the phase accumulated in a round-trip. Here the microresonator is assumed to be critically coupled, for simplicity. Under the mean-field approximation and the good cavity limit, the primary comb spacing, which depends on the optimal frequency where modulation instability gain reaches its maximum, can be solved as (Section A.3):

$$\Delta = \frac{1}{\sqrt{\pi c|\beta_2|}}\sqrt{\eta\left(n_g f_p - N\frac{n_g^2}{n_0}f_{rep} - \frac{\gamma c P_{int}}{\pi}\right)} \tag{2.4}$$

where $\eta = \frac{\beta_2}{|\beta_2|}$ is the sign of the GVD, n_g is the group index, n_o is the refractive index, *N* is the longitudinal mode number, *c* is the speed of light in vacuum, f_p is the pump frequency, and P_{int} is the intracavity pump power. This picture of comb formation is illustrated in the schematic Figure 2.2b.

Equations 2.1 and 2.4 explicitly show the dependence of ξ on f_p, f_{rep}, and P_{int}. In the high-*Q* Si_3N_4 microresonator, P_{int} is resonantly enhanced to be as high as 30 W and it is the dominant heat source to change the cavity temperature and subsequently the comb spacing [29]. For instance, a pump power variation of 0.12% results in a microcomb line-to-line frequency spacing of 1.6×10^{-5} fluctuation, corresponding to a large cavity temperature fluctuation of 1 K. While f_{rep} is directly dependent on cavity temperature and P_{int} [54], we note that f_{rep} is only indirectly dependent on f_p. This indirect dependence is eventually attributable to a change in P_{int} since a change in detuning changes the power coupled to the cavity.

Theoretically this can be understood by noting that the usual way f_p directly contributes to changes in f_{rep} is via Raman self-frequency shift [54], however since our comb is not a soliton, this effect is negligible. Thus, we expect the f_{rep} stabilization will effectively eliminate the P_{int} fluctuation. Under this assumption, the offset frequency is reduced to just a function of pump frequency

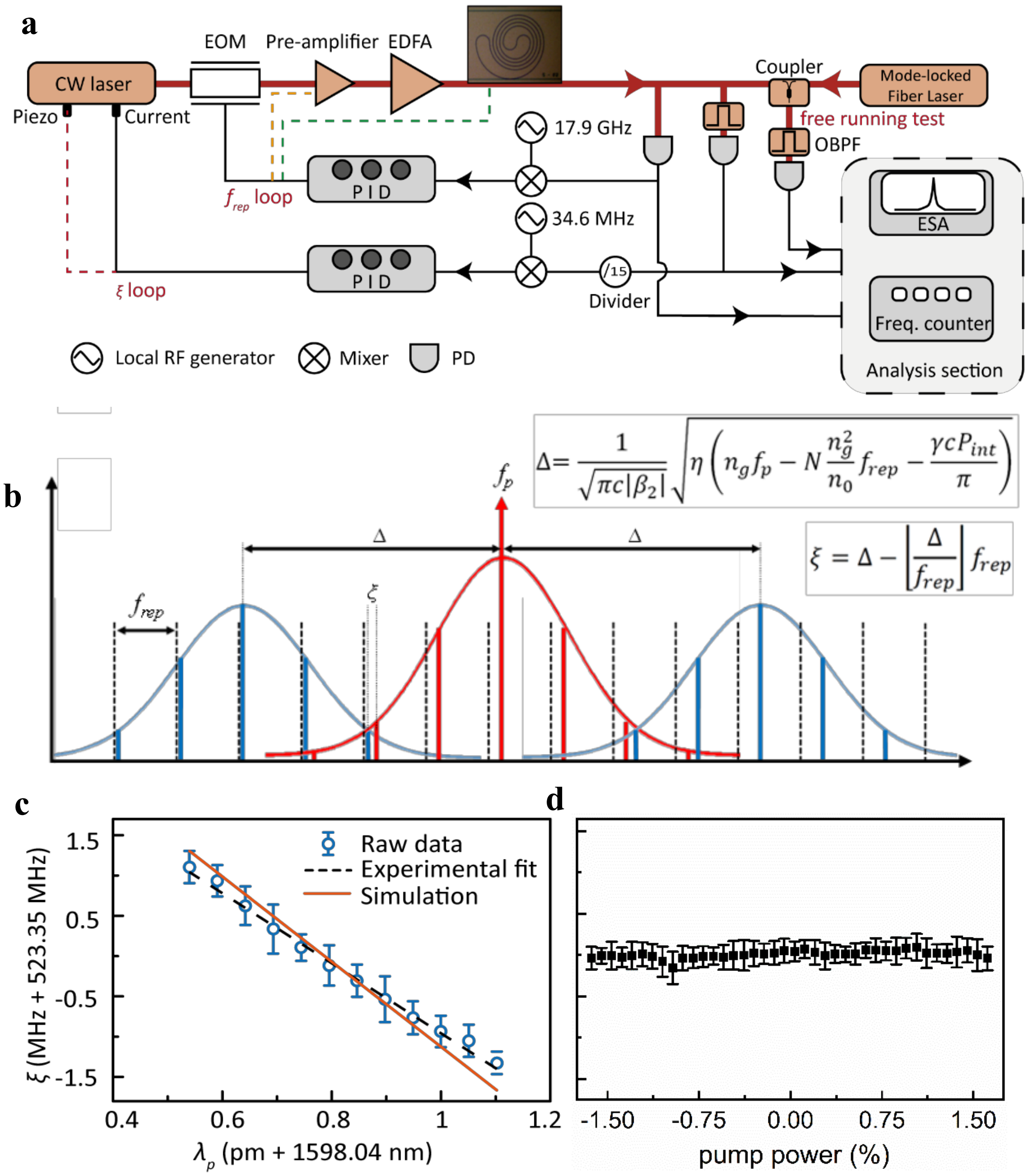

Figure 2.2. **(a)** Frequency microcomb setup for stabilization. Here EOM, Electro-optic modulator; EDFA, Erbium doped fiber amplifier. For ξ and f_{rep} stabilization, an EOM controls the pump power and the ECDL diode current controls the pump laser frequency, through two phase locked loops. We also note that, in place of the EOM, a polarization rotator with a PBS can also serve for intensity modulation. To increase the locking duration, we implemented slow control of the ECDL PZT (red dashed line) and the EDFA gain (yellow dashed path). The slow feedback to the EDFA gain may also alternatively be replaced by sending the feedback signal to the temperature controller on the chip holder (which controls device temperature) instead (green dashed path). This reduces loop dynamic range but also

mitigates the effects of ambient temperature drift. The stability of the locked microcomb is interrogated out-of-loop by beating with an independently stabilized fiber frequency comb. **(b)** Frequency domain illustration of the demonstrated full-stabilization technique. Here the offset frequency, ξ, is linked with the primary comb line spacing, Δ, by the constitutive relation $\xi = \Delta - \left\lceil \frac{\Delta}{f_{rep}} \right\rceil f_{rep}$. Furthermore, $\Delta = \frac{1}{\sqrt{\pi c|\beta_2|}} \sqrt{\eta \left(n_g f_p - N \frac{n_g^2}{n_0} f_{rep} - \frac{\gamma c P_{int}}{\pi} \right)}$ where β_2 is the group velocity dispersion (GVD), $\eta = \frac{\beta_2}{|\beta_2|}$ is the sign of the GVD, n_g is the group index, n_0 is the refractive index, N is the longitudinal mode number, c is the speed of light in vacuum, γ is the nonlinear coefficient, and P_{int} is the intracavity pump power. **(c)** Subsequent to f_{rep} stabilization, the offset frequency shows strong linear correlation with pump wavelength (blue circles) with a slope of about 4.5 MHz per picometer shift of pump. The simulated slope (plotted in orange) also shows good agreement with measured data. **(d)** Measured offset frequency as a function of applied pump power, after f_{rep} stabilization. The pump power is stepwise changed by a total of 3.4% via the EFDA gain. The offset frequency remains constant within the error bar, verifying that f_{rep} stabilization effectively eliminates the intracavity pump power fluctuation. For **(c)** and **(d)**, 10 measurements are taken to determine the mean value, and the error bars are defined as the peak-to-peak deviations from the 10 measurements. Here the pump frequency is not yet stabilized, resulting in the error bars in the offset frequency measurements.

once the comb spacing is stabilized. Control of f_{rep} and ξ is thus equivalent to regulation of f_{rep} and f_{ceo} in full stabilization of the Kerr frequency comb. Figure 2.2c plots the measured and simulated offset frequency as a function of pump wavelength after the f_{rep} stabilization (The simulated slope in Figure 2.2c is described in detail in Section A.3). We observe that the offset frequency scales linearly with the pump wavelength at a slope of 4.5 MHz per picometer shift of pump (corresponding to a sensitivity of 3.7×10^{-2}). In addition, in Figure 2.2d, we introduce an out-of-loop perturbation to pump power after f_{rep} stabilization, but observe no change in the breather tone. If the f_{rep} lock had not entirely eliminated the introduced power change, the P_{int} dependence of (and hence ξ) would have caused a change in the breather frequency. The measurements therefore validate the assumption that f_{rep} stabilization effectively eliminates the intracavity pump power fluctuation and reduces the dependence of ξ to just a function of pump frequency. Mode hybridization in the current multi-mode Si_3N_4 microresonator leads to abrupt increase of local GVD and results in the pinning of primary comb lines [55, 56]. The effect reduces the slope, *i.e.* sensitivity, of offset frequency in gauging the pump frequency fluctuation Eq. 2.4). Nevertheless, the sensitivity is already more than two orders of magnitude larger than the optical frequency division ratio, $\frac{\partial f_{rep}}{\partial f_{opt}} \sim 10^{-4}$, where f_{opt} is the optical frequency of any the generated comblines. The fluctuations of the Kerr frequency comblines $\delta f_{opt} = \frac{1}{\partial f_{rep} \backslash \partial f_{opt}} \delta f_{rep} + \frac{1}{\partial \xi \backslash \partial f_{opt}} \delta \xi$ ($\delta\xi$ is under constant f_{rep}) are thus bounded by the residual error and the local oscillator of the f_{rep} stabilization loop (Section 2.7), when both f_{rep} and ξ are stabilized. We must note here that although the coefficient of the $\delta\xi$ term is relatively small, if ξ is not locked then the pump is still free to drift (in this situation $\delta\xi$ will be orders of magnitude larger than δf_{rep}) and f_{opt} is no longer stable.

2.4 Kerr comb stabilization

Figure 2.3a and 2.3b show the quality of the ξ stabilization (after f_{rep} stabilization is engaged). To minimize the crosstalk between the two phase-locked loops, here the proportional-integral corner frequency is set lower than that of the f_{rep} stabilization loop. On the other hand, a second integrator at 500 Hz is included to better suppress low frequency noise. Compared to the unstabilized beat note, the stabilized ξ shows a clear resolution limited coherent spike (Figure 2.3a). The noise oscillation at 205 kHz is the remaining crosstalk derived from the corresponding noise peak in the f_{rep} stabilization loop (Section 2.7). Figure 2.3b. plots the single sideband phase noise of the reference oscillator as well as the residual error of our feedback loop from 1 Hz to 1 MHz. While the low frequency noise is well suppressed to below the reference, excessive phase noise above 2 kHz from carrier is observed. The root mean square phase error integrated from 6 Hz to 600 kHz is 55 mrad. To verify the uniformity of the offset frequencies, ξ are measured at two distinct spectral regions other than 1553.5 nm where the beat note is used for stabilization. The selected spectral segments (marked red in Figure 2.3c) are representative as each ξ is generated from the overlap of different groups of secondary comb lines. Counter results and the corresponding histogram analysis are summarized in Figure 2.3d and 2.3e. The mean values at 1544.72 nm and 1547.86 nm are 523349999.84 Hz and 523349999.92 Hz respectively, while the beat note at 1553.5 nm is stabilized to 523350000 Hz. Offset frequencies at different spectral regions are identical within a sub-Hz error, confirming the uniformity of ξ across the Kerr frequency comb. Phase locking of f_{rep} and ξ to low noise microwave oscillators is complete and it should guarantee the optical frequency stability of Kerr frequency comb.

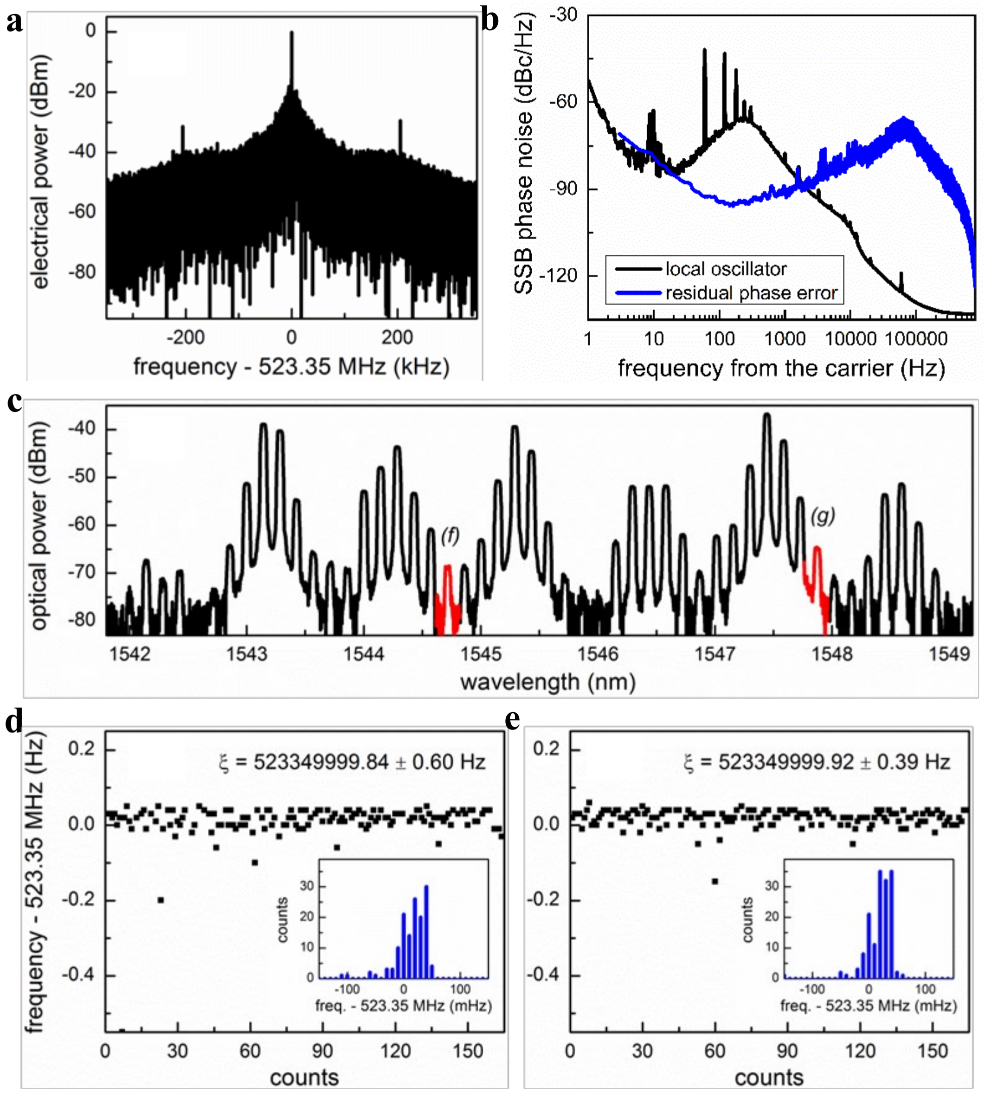

Figure 2.3. **(a)** Electrical spectrum of the stabilized beat note of ξ with a resolution band-width (RBW) of 10 Hz. To minimize the crosstalk between the two phase-locked loops, here the proportional-integral corner frequency is set lower than that of the f_{rep} loop. Furthermore, a second integrator at 500 Hz and a differentiator at 100 kHz are included to better suppress low frequency noise and improve the loop stability respectively. **(b)** Single-sideband (SSB) phase noise of the reference 523.35 MHz local oscillator and the residual loop error, showing excess phase noise of the stabilized ξ above 2 kHz from carrier. **(c)** To verify the uniformity of the offset frequencies, ξ are measured at two other spectral regions (marked in red; 1544.72 nm and 1547.86 nm) beside the 1553.5 nm region where the beat note is stabilized to 523350000 Hz in the phase-locked loop. The selected spectral segments are representative as each ξ is generated from the overlap of different groups of secondary comb lines. **(d)** and **(e)** Counter results and the corresponding histogram analysis (insets). The mean value at 1544.72 nm is 523349999.84 Hz, the standard deviation over 160 measurements is 600 mHz, and the interquartile range is 50 mHz. The mean value at 1547.86 nm is

523349999.92 Hz, the standard deviation over 160 measurements is 390 mHz, and the interquartile range is 40 mHz.

2.5 Stabilization parameters

The PI^{2}D control servos we use for feedback in both f_{rep} and ξ phase-locked loops have a full bandwidth of 10 MHz and can be set to have two PI corners, to effectively suppress low frequency noise, in addition to a PD corner to increase the loop stability. To ensure minimal crosstalk between the loops, the PI corners are set at very different frequencies. For the f_{rep} stabilization, the PI corner for the first integrator is set to 200 kHz while the second integrator is switched off. For the ξ stabilization, the PI corners are set to 500 Hz and 50 kHz to achieve higher suppression for low frequency noise. In addition, the PD corners are set to 200 kHz and 100 kHz respectively with a differential gain of 10 dB. The derivative control is important in our system to make the feedback loop more stable and achieve optimal noise suppression. Due to alignment drift in the optics, the mean level of the servo output keeps increasing until the lock is lost in a few minutes. To increase the operation time, we also include in each loop a slow feedback where the feedback error signal is generated by integrating the servo output for 1 second. The control units of the slow feedback loops are the EDFA gain and the piezoelectric transducer (PZT), which have larger dynamic ranges than the EOM and the diode current. For out-of-loop analysis, the beat frequency between the Kerr frequency comb and the fiber laser frequency comb is counted with a 10-digit, Λ -type frequency counter and the Allan deviation is estimated using the equation $\sigma_A\left(\tau\right) = \sqrt{\frac{1}{N}\sum_{i=1}^{i=N}\frac{\left(\overline{y}_{i+1}-\overline{y}_i\right)^2}{2}}$, where τ , $\overline{y}_i$, and $N = \min\left\{20, \left[\frac{200}{\tau}\right]\right\}$ are the gate times, the fractional frequencies, and the number of samples respectively. The grating-based filter critically removes the unwanted reference fiber laser frequency comb teeth such that clean heterodyne beat notes with more than 30 dB signal to noise ratio (measured with a 100 kHz RBW), sufficient for reliable counting measurements, can be routinely obtained.

2.6 Details of the measurement setup

The measurement setup is shown in Figure 2.2 in the main text. The comb spacing is measured by sending a section of the comb to a high speed photodetector to directly detect the beat note from the repetition rate f_{rep}. We then obtain the error signal for feedback by downmixing the output signal with a 17.9 GHz local oscillator. This error signal is the input to a PI^{2}D lock box with a bandwidth of 10 MHz, which sends the feedback signal to an EOM to modulate the input power of the 3W EDFA which pumps the microresonator. The EDFA is operated in the current control mode to achieve effective modulation of the output power, to within 1% and less than 0.1 dB. Even with the free-space alignment optics, the lock can be maintained for more than an hour in each measurement set. In a fully packaged system, the lock can likely be maintained for a longer time. We also note that, with higher microcavity Q, the microcomb threshold power can be lowered and microcombs, with the similar FSR as our demonstration, with tens of milliwatt pump power has been implemented entirely on chip [57, 58].

In addition to power modulation via the EOM, we also have a secondary feedback signal (derived by integrating the primary feedback control signal) to the EDFA which directly modulates the power, relatively slowly, primarily with the objective to increase the dynamic range of the lock (EDFA is not used as the sole feedback because it cannot be operated at the full feedback bandwidth). The feedback is designed in the above manner, with fast feedback via the EOM for high feedback bandwidth and slow feedback via the EDFA for high dynamic range, to preserve an optimal lock for a long period of time. Fig. 2.6 summarizes the quality of the f_{rep} stabilization. After the stabilization of the comb spacing, we notice that the offset beat ξ also becomes more stable as can be visually observed from Fig. 2.7. This is per our expectation of partial correlation between and f_{rep} as described in the main text. The offset frequency ξ can be used as an indicator of pump frequency after stabilization of f_{rep}, as explained in detail in the main text. We therefore use this signal to stabilize the pump frequency when the comb spacing is locked. To achieve a high SNR (which is required to lock effectively), we use an optical grating filter to select a 1-nm section of the comb where the beat frequency is strongest and then send that section to a photodetector to detect the beat (SNR is higher because of a strong beat note in the localized region and also because the

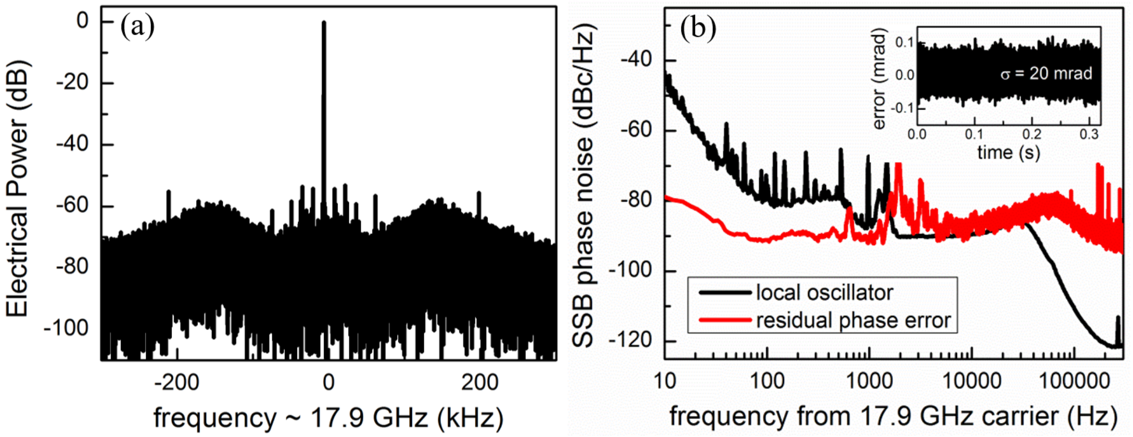

Figure 2.4. **(a)** RF spectrum of the stabilized beat note of f_{rep} with an RBW of 10 Hz. In the PI2D loop filter, the PI corner and differential frequency were both set at 200 kHz. The design provides a delicate compromise between noise suppression and loop stability. A remaining small noise oscillation at 205 kHz, however, is still present. b, Single-sideband phase noise of the reference 17.9 GHz local oscillator and the residual error from the f_{rep} phase-locked loop, showing an excess phase noise of the stabilized comb spacing above 40 kHz from carrier. Inset: rms phase error integrated from 6 Hz to 600 kHz is 20 mrad.

detector is not saturated by the f_{rep} beat note, which is much stronger when a larger region of the comb is considered). We send the output to a divide-by-15 frequency divider, and then downmix the signal with a local oscillator operating at 33 MHz to obtain the error signal. The offset beat ξ has more high frequency noise than f_{rep}, as we might expect, because it is affected not only by the pump frequency instability but also by high frequency noise in pump power that is not fully compensated by f_{rep} stabilization, the frequency divider is therefore necessary to reduce the high frequency noise and increase the efficacy of the lock. The error signal is sent to a PI^{2}D lock box which provides a feedback signal to modulate the diode current of our ECDL which stabilizes the pump frequency.

Similar to the feedback to lock f_{rep}, we use a slower secondary feedback (derived from the integrated primary feedback control signal) via the piezo controller of the ECDL to increase dynamic range and preserve the lock for a longer time. We have included a detailed discussion of the feedback locking mechanism in Section 2.5.

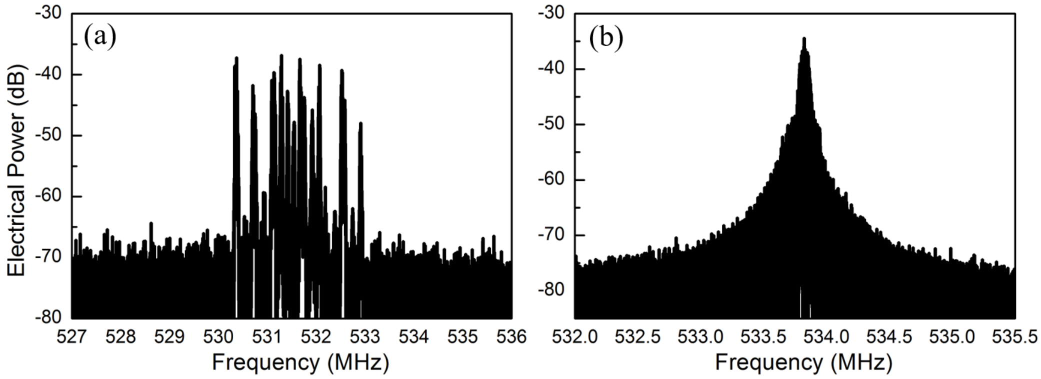

Figure 2.5. **(a)** The measured offset beat ξ at an RBW of 100 kHz when the f_{rep} is not stabilized. The high noise in the beat arises because the offset frequency Δ depends on pump frequency and intracavity power given by $\Delta = \frac{1}{\sqrt{\pi c|\beta_2|}}\sqrt{\eta\left(n_g f_p - N\frac{n_g^2}{n_0} f_{rep} - \frac{\gamma c P_{int}}{\pi}\right)}$ and since $\xi = \Delta - \left\lceil \frac{\Delta}{f_{rep}} \right\rceil f_{rep}$, fluctuations in both pump frequency and f_{rep} add to instability in ξ. b, The measured offset beat ξ at an RBW of 10 kHz after f_{rep} is stabilized. We observe an increase in stability of ξ after stabilization of f_{rep} (and thereby stabilization of pump power). Residual noise in the beat note is due to pump frequency noise (and residual noise in pump power after f_{rep} stabilization). ξ can therefore be used to sense pump frequency fluctuations and stabilize it via feedback.

2.7 Details of the measurement setup

The measurement setup is shown in Figure 2.2 in the main text. The comb spacing is measured by sending a section of the comb to a high speed photodetector to directly detect the beat note from the repetition rate f_{rep}. We then obtain the error signal for feedback by downmixing the output signal with a 17.9 GHz local oscillator. This error signal is the input to a PI^{2}D lock box with a bandwidth of 10 MHz, which sends the feedback signal to an EOM to modulate the input power of the 3W EDFA which pumps the microresonator. The EDFA is operated in the current control mode to achieve effective modulation of the output power, to within 1% and less than 0.1 dB. Even with the free-space alignment optics, the lock can be maintained for more than an hour in each measurement set. In a fully packaged system, the lock can likely be maintained for a longer time. We also note that, with higher microcavity Q, the microcomb threshold power can be lowered and microcombs, with the similar FSR as our demonstration, with tens of milliwatt pump power has been implemented entirely on chip [57,58].

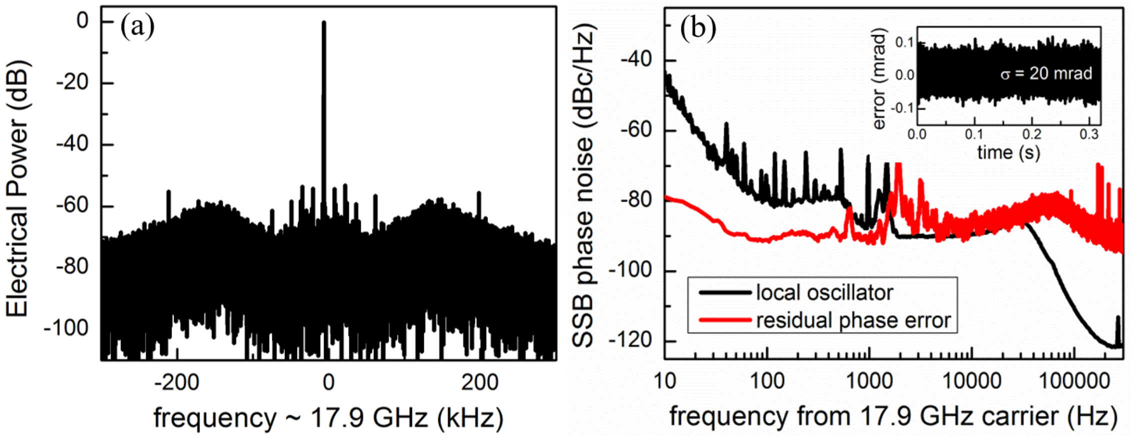

Figure 2.6. **(a)** RF spectrum of the stabilized beat note of f_{rep} with an RBW of 10 Hz. In the PI2D loop filter, the PI corner and differential frequency were both set at 200 kHz. The design provides a delicate compromise between noise suppression and loop stability. A remaining small noise oscillation at 205 kHz, however, is still present. b, Single-sideband phase noise of the reference 17.9 GHz local oscillator and the residual error from the f_{rep} phase-locked loop, showing an excess phase noise of the stabilized comb spacing above 40 kHz from carrier. Inset: rms phase error integrated from 6 Hz to 600 kHz is 20 mrad.

In addition to power modulation via the EOM, we also have a secondary feedback signal (derived by integrating the primary feedback control signal) to the EDFA which directly modulates the power, relatively slowly, primarily with the objective to increase the dynamic range of the lock (EDFA is not used as the sole feedback because it cannot be operated at the full feedback bandwidth). The feedback is designed in the above manner, with fast feedback via the EOM for high feedback bandwidth and slow feedback via the EDFA for high dynamic range, to preserve an optimal lock for a long period of time. Fig. 2.6 summarizes the quality of the f_{rep} stabilization. After the stabilization of the comb spacing, we notice that the offset beat ξ also becomes more stable as can be visually observed from Fig. 2.7. This is per our expectation of partial correlation between and f_{rep} as described in the main text. The offset frequency ξ can be used as an indicator of pump frequency after stabilization of f_{rep}, as explained in detail in the main text. We therefore use this signal to stabilize the pump frequency when the comb spacing is locked. To achieve a high SNR (which is required to lock effectively), we use an optical grating filter to select a 1-nm section of the comb where the beat frequency is strongest and then send that section to a photodetector to detect the beat (SNR is higher because of a strong beat note in the localized region and also because the detector is not saturated by the f_{rep} beat note, which is much stronger when a larger region of the comb is considered). We send the output to a divide-by-15 frequency divider, and then downmix the signal with a local oscillator operating at 33 MHz to obtain the error signal. The offset beat ξ has more high frequency noise than f_{rep}, as we might expect, because it is affected not only by the pump frequency instability but also by high frequency noise in pump power that is not fully compensated by f_{rep} stabilization, the frequency divider is therefore necessary to reduce the high frequency noise and increase the efficacy of the lock. The error signal is sent to a PI^{2}D lock box which provides a feedback signal to modulate the diode current of our ECDL which stabilizes the pump frequency.

Similar to the feedback to lock f_{rep}, we use a slower secondary feedback (derived from the integrated primary feedback control signal) via the piezo controller of the ECDL to increase dynamic range and preserve the lock for a longer time. We have included a detailed discussion of the feedback locking mechanism in Section 2.5.

2.8 Out-of-loop assessment of the stabilized Kerr frequency comb

We interrogated the locked microcomb by beating with an external stabilized FFC, and counting the beat frequencies with a 10-digit, Λ-type frequency counter. The FFC is independently stabilized with the *f-2f* interferometer technique (Section A.4). In Figure 2.8a an external perturbation is artificially introduced by disconnecting the slow feedback to the laser piezo control and instead using the piezo to induce a periodic 20 MHz frequency fluctuation. The inset shows clear suppression of the external perturbation ($>$ 20 dB) when both phase locked loops are engaged. In Figure 2.8b we plot the Allan deviations (ADs) of the comb lines under two different locking schemes. When slow feedback is provided to the EDFA and there is no ambient temperature stabilization (yellow path in Figure 2.2a), a $5\times10^{-11}/\sqrt{\tau}$ (at 1 s) frequency instability is observed, close to the 17.9 GHz reference oscillator. No apparent difference is observed between the ADs of the

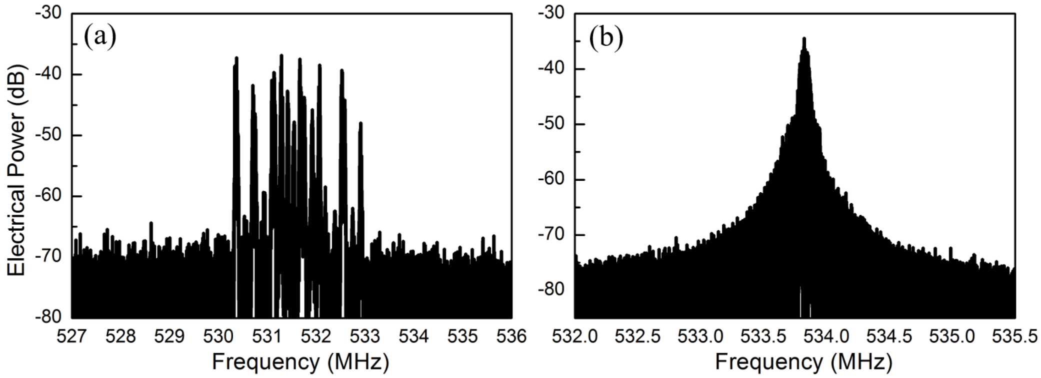

Figure 2.7. **(a)** The measured offset beat ξ at an RBW of 100 kHz when the f_{rep} is not stabilized. The high noise in the beat arises because the offset frequency Δ depends on pump frequency and intracavity power given by $\Delta = \frac{1}{\sqrt{\pi c|\beta_2|}}\sqrt{\eta\left(n_g f_p - N\frac{n_g^2}{n_0}f_{rep} - \frac{\gamma c P_{int}}{\pi}\right)}$ and since $\xi = \Delta - \left\lceil \frac{\Delta}{f_{rep}} \right\rceil f_{rep}$, fluctuations in both pump frequency and f_{rep} add to instability in ξ. b, The measured offset beat ξ at an RBW of 10 kHz after f_{rep} is stabilized. We observe an increase in stability of ξ after stabilization of f_{rep} (and thereby stabilization of pump power). Residual noise in the beat note is due to pump frequency noise (and residual noise in pump power after f_{rep} stabilization). ξ can therefore be used to sense pump frequency fluctuations and stabilize it via feedback.

two comb lines 43 nm apart, indicating a good coherence transfer across the Kerr frequency comb. For longer gate times, the ADs show a characteristic linear dependence on the gate time that can be attributed to the uncompensated ambient temperature drift. For instance, considering the current chip holder has a long term temperature stability of less than 10 mK which is limited by the resolution of the temperature sensor, a pump power proportional change of 1.2×10^{-5} is needed to keep the intracavity temperature and consequently the f_{rep} constant. Such pump power variation in turn results in a change of 13 kHz in the pump frequency ($\Delta f_p = \frac{\gamma c}{\pi n_g}\Delta P_{int}$ from Eq. 2.4). The frequency instability is gauged to be in the range of 7×10^{-11} when compared to optical carrier of 188 THz, in agreement with the asymptotic behavior of the measured AD. We can however partially compensate this ambient temperature drift via improved double-walled packaging along with slow feedback to a TEC on the chip holder that directly controls chip temperature (green path in Figure 2.2a). After implementing these improvements we achieve an improved Allan deviation of 2×10^{-11} at 20-sec gate time, and decreased the slope of AD increase from τ to $\tau^{0.23}$, marked as the blue line in Figure 2.8b.

The unique stabilization technique thus implemented can be used to stabilize the absolute frequency of each comb line in the Kerr frequency comb without the need of an octave-level comb spectrum and any external nonlinear process. We also confirm the universality of this method by finding comb states with unique ξ across multiple rings with widely varying f_{rep} and waveguide geometries (detailed in Section A.5). However, this method does not allow us to determine the precise optical frequency of each line without calibration via an optical reference. Despite this apparent limitation, the method described here can be used to extend the functionality of frequency combs to various applications while preserving a low SWaP as external non-linear processes are not required for comb stabilization. We briefly describe one such application and lay out a path for its achievement in the next section.

2.9 Generation of low noise microwaves

As another application of the correlation between f_p, pump power, f_{rep} and ξ, we propose the generation of low noise microwaves by stabilizing the pump frequency and ξ. The following method may also be applied to full-stabilization of combs with f_{rep} too large to directly measure. In prior literature low noise microwave generation via optical frequency division [59,60] has been accomplished with broad octave-level combs that allow for internal detection of f_{ceo} via f-2f interferometry and atomic transition or external cavity reference that may be used to stabilize a single comb line [61–65]. The comb f_{rep} instability would then be suppressed by a factor close to the optical frequency division ratio ($\approx 10^4$) when compared to the optical reference instability. We can however remove the requirement for the detection of f_{ceo} and hence for the comb spectrum to be across an octave in frequency if we instead use a modified method based on the stabilization of ξ described previously [66]. To generate low noise microwaves, we propose locking the pump to a stable optical reference and then locking the frequency ξ to a microwave LO, it can be shown that doing so stabilizes the f_{rep}. This is because ξ depends on both pump frequency and pump power and upon stabilizing the pump frequency to an optical reference, pump power is the sole factor determining the stability of both ξ and f_{rep} which are now directly correlated. Figure 2.8c shows the setup schematic for stabilization. The device is pumped with a high power EDFA and

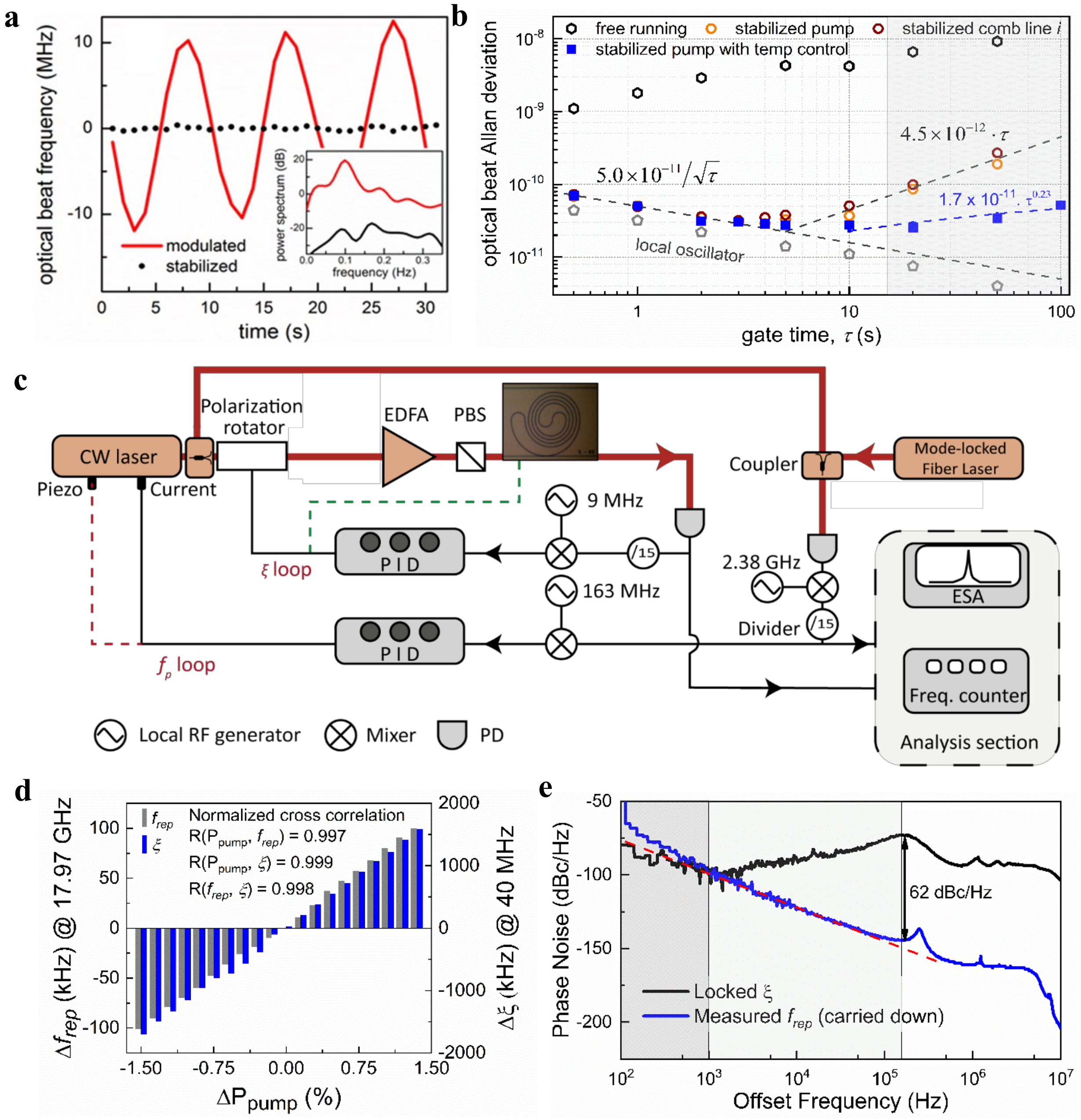

Figure 2.8. **(a)** Optical beat frequency between the pump and the stabilized fiber frequency comb (FFC). With both the f_{rep} and ξ phase-locked loops engaged, the artificially introduced pump frequency perturbation (red curve) is suppressed and the optical beat frequency remains constant (black curve). The inset plots the corresponding power spectral densities, showing a more than 20 dB pump frequency noise suppression by the stabilization loops. **(b)** Free running comb Allan Deviation (AD) is plotted with black hexagons. The orange and brown circles plot the AD of the pump and ith combline respectively when stabilized with slow feedback to the preamp (yellow path in Fig. 2.2a). No apparent difference is observed between the ADs of the two comb lines 43 nm apart, indicating

a good coherence transfer across the microcomb. Our measured values are close to the local oscillator AD (gray pentagons) used to stabilize f_{rep}. For longer gate times, ADs show a characteristic linear dependence on the gate time, attributed to the uncompensated ambient temperature drift. To mitigate this, improved environmental isolation and partial compensation of ambient temperature drift (via green path in Fig. 2.2a) is implemented and AD of stabilized pump with is plotted in blue squares. The AD is improved to 2×10^{-11} at 20-sec gate time, and slope of AD increase is reduced from τ to $\tau^{0.23}$. The shaded region on the right marks the point where slow thermal drift degrades the lock performance. **(c)** The setup schematic to generate low noise microwaves. The pump laser is directly locked to an optical reference, in this case, a fully-stabilized FFC referenced to an ultra-stable cavity. Subsequently the offset ξ is also locked via feedback to pump power (through the action of the polarization rotator and PBS). The above mentioned loops indirectly lock f¬rep due to suppression of both pump frequency noise and power fluctuations. Slow feedback is sent to the temperature of the chip mount via a TEC to partially suppress ambient thermal drift. **(d)** f_{rep} is plotted in the black bars and ξ is plotted in blue. Both f_{rep} and ξ are strongly correlated with pump power, with measured correlation greater than 0.997. The absolute and frequency sensitivity to pump power is respectively $\approx$ 15 and $\approx$ 6,700 times larger for ξ than f_{rep}. **(e)** Locking of both ξ and pump frequency allows for suppression of f_{rep} noise (also see Section A.5I). Here, the phase noise of the locked ξ (at 40 MHz) is plotted in black and the measured f_{rep}, after engaging both feedback loops (and carried down to 40 MHz), is plotted in blue. We observe a 62 dB suppression of noise at high offset frequencies matching well with our expectations, in the unshaded region to the right, however at lightly shaded region in the center uncompensated $1/f^2$ thermal noise (plotted in the dashed red line) begins to dominate and eventually surpasses the locked signal in the shaded region on the left. We can mitigate the effect of this thermal noise via better environmental isolation or passive cavity temperature feedback.

a comb state measured to have a unique offset ξ at 40 MHz frequency with over 50 dB SNR (at an RBW of 100 kHz) is generated. The pump is then locked to a fully-stabilized fiber frequency comb referenced to an ultra-stable cavity. The offset ξ is locked via feedback to a polarization rotator. Together with the PBS placed after the EDFA, this can modulate the input power to the device. To adjust the chip mount and resonator temperature, we feedback with slow bandwidth to the TEC. This partially suppresses ambient thermal drift and increases lock dynamic range. We confirm the strong linear correlation between pump power, f_{rep} and ξ in Figure 2.8d. We observe that for a 3% change in pump power, corresponding to a 200 kHz change in f_{rep}, there is a 3 MHz change in ξ. This implies that the frequency sensitivity of ξ to pump power fluctuations 15 times higher, and (due to the large difference in the carrier frequencies) the frequency sensitivity of ξ

to pump power is 6,700 times higher than that of f_{rep}. Locking ξ may thus suppress phase noise in f_{rep}, beyond what would be achieved by directly locking f_{rep} to a microwave reference. When f_{rep} is divided down (in the limit of no residual noise) to the carrier frequency of ξ, this would correspond to a phase noise suppression of 64.7 dB. f_{rep} before and after ξ lock is recorded on the ESA and plotted in Section A.5I, confirming that locking ξ suppresses f_{rep} noise. In Figure 2.8e we plot the phase noise of both the locked ξ and f_{rep} (divided down to 40 MHz), we see that at high offset frequencies the noise is suppressed by over 60 dB as per our expectations, however there is still uncompensated f^{-2} thermal noise due to the coupled ambient temperature fluctuations, that our loops cannot remove. This noise can however be further reduced by suppressing ξ's phase noise parameters, and increasing the thermal isolation or implementing passive temperature stabilization techniques such as an auxiliary laser [34].

2.10 Summary

Utilizing only internally accessible comb-parameters such as f_{rep} and offset frequency ξ, we have demonstrated an approach to fully stabilize combline frequencies of appropriately generated comb states. Existence of microcombs with only one set of primary comb lines, critical for the new stabilization method, is a consistent property of these nonlinear microresonators and have been found in devices across multiple chipsets with very different dispersion, Q and f_{rep}. The sensitivity for our device is measured as 3.7×10^{-2}, already more than two orders of magnitude larger than the optical frequency division ratio, and it can be improved by novel microresonator designs to suppress the mode hybridization [65]. Furthermore, having both f_{rep} and ξ phase-locked to low noise microwave oscillators concurrently enables the frequency microcomb optical stability. Simulation results of the correlation between ξ and pump frequency, needed for a successful lock, are also in good agreement with experiment. We further show the frequency microcomb has frequency instability of 2×10^{-11} at 20- second gate time, bounded by the external microwave reference. For gate times longer than 20 seconds, AD increases due to the uncompensated ambient temperature drift. Such long-term drift can be improved by a better thermal shield or a more effective temperature control [67]. We have also discussed an avenue in which this method might prove useful, namely in the generation of low noise microwaves, and we have also demonstrated a proof-of-principle experiment showing this. We believe our method could find use in a range of applications that require stable chip-scale optical frequency combs due to its advantages of low SWaP and potentially reduced need for optical peripherals.

CHAPTER 3

Gate-tunable frequency combs in graphene-nitride microresonators

3.1 Introduction

Chip-scale frequency combs, based on the Kerr and Raman nonlinearities in monolithic microresonators with ultrahigh quality factors [11,17,68], have recently led to progress in optical clockwork and observations of temporal cavity solitons [25, 28, 29, 39]. But the chromatic dispersion within a laser cavity, which determines the comb formation [20, 69], is usually difficult to tune with an electric field, whether in microcavities or fiber cavities. Such electrically dynamic control could bridge optical frequency combs and optoelectronics, enabling diverse comb outputs in one resonator with fast and convenient tunability. Arising from its exceptional Fermi-Dirac tunability and ultrafast carrier mobility [70–72], graphene has a complex optical dispersion determined by its optical conductivity, which can be tuned through a gate voltage [73, 74]. This has brought about optoelectronic advances such as modulators [75, 76], photodetectors [77] and controllable plasmonics [78, 79]. Here we demonstrate the gated intracavity tunability of graphene-based optical frequency combs, by coupling the gate-tunable optical conductivity to a silicon nitride photonic microresonator, thus modulating its second- and higher-order chromatic dispersions by altering the Fermi level. Preserving cavity quality factors up to 10^6 in the graphene-based comb, we implement a dual-layer ion-gel-gated transistor to tune the Fermi level of graphene across the range 0.45-0.65 electronvolts, under single-volt-level control. We use this to produce charge-tunable primary comb lines from 2.3 terahertz to 7.2 terahertz, coherent Kerr frequency combs, controllable Cherenkov radiation and controllable soliton states, all in a single microcavity. We further demonstrate voltage-tunable transitions from periodic soliton crystals to crystals with defects, mapped by our ultrafast second-harmonic optical autocorrelation. This heterogeneous graphene microcavity, which combines single-atomic-layer nanoscience and ultrafast optoelectronics, will help to improve our understanding of dynamical frequency combs and ultrafast optics.

3.2 Conceptual design

Figure 3.1a-c shows the concept and fabrication of our graphene gate-tunable Kerr frequency comb with source-drain and top gating. This is further detailed in section 3.7 and in sections B.1, B.2. To ensure transparency and minimal effect on the resonator quality factor (Q) for coherent comb generation, we top-gate the interacting graphene to pull the Fermi level up to 0.6 eV for reduced photon absorption in the nearly massless Dirac cone. An ion-gel capacitor is implemented on top of the graphene monolayer [80]. The electric double layer in the ionic liquid provides a capacitance up to about 7.2 $\mu F cm^{-2}$; this high value enables high doping control and comb tunability with a few-volt-level gating. This is important to produce sharp modulation of the cavity chromatic dispersion while keeping the cavity loss low. In addition to the optimized 300-nm gap between the Si_3N_4 waveguide and the graphene layer, we optimize the planar interaction length of the arc in which the graphene overlaps the nitride resonator to be about 80 μm. The grey ring shown in Fig. 1a is the nitride resonator. This offers substantial tunability of the frequency comb combined with minimal graphene absorption losses. Figure 3.1d plots the computed optical group velocity dispersion (β_2) and the computed third-order dispersion (β_3) for tuned Fermi levels from 0.2 eV to 0.8 eV of the graphene monolayer. For each Fermi level, we note the wavelength oscillations in both β_2 and β_3, arising from the lifetime of the carrier relaxation oscillations in graphene captured in the resonance of the monolayer sheet conductivity. As a result, the graphene β_2 can be tuned from anomalous to normal dispersion and then back to anomalous by means of the gate voltage, which is important for nonlinear phase-matching tunability. This enables wide and tunable frequency comb generation in the graphene-based microresonator (GMR). Based on the modelled overall graphene β_2 and β_3, we model the heterogeneous microresonator for Kerr frequency comb generation. Figure 3.1e shows the temporal map of the comb dynamics in the GMR, obtained by Lugiato-Lefever equation (LLE) modelling. At E_F = 0.2 eV, the Q factor is low, and hence there is no comb generation. At E_F = 0.5 eV, the GMR has $Q \approx 8 \times 10^5$, $\beta_2 \approx -50 fs^2\, mm^{-1}$ and $\beta_3 \approx 0$, resulting in slow comb generation. At E_F = 0.8 eV,, we observe rapid generation of a full comb in the numerical model, for $Q > 1 \times 10^6$, $\beta_2 \approx -30 fs^2\, mm^{-1}$ and $\beta_3 \approx -400 fs^3\, mm^{-1}$.

3.3 Gate-tuning the microresonator

Figure 3.2a shows the electrical tuning performance of graphene in the GMR. For a fixed source-drain voltage V_{SD} = 10 mV, the source-drain current I_{SD} is tuned with the gate voltage V_G. When V_G reaches 2.4 V, I_{SD} has a minimum of 6.5 μA. Here the carrier density of the graphene monolayer reaches the Dirac point. When V_G is less than 2.4 V, graphene is p-doped. In cyclic V_G tuning, a hysteresis loop is observed, owing to electronic trapping. The corresponding gate-tunable Fermi energy $|E_F|= \hbar|\nu_F|(\pi N)^{-1/2}$ [81] is plotted in the bottom panel of Fig. 2a and noted to be proportional to $(V_G)^{1/2}$; here N is the carrier density, while ν_F indicates the Fermi velocity. In our experiment, we tune V_G in the range -2 V to 0 V, thereby controlling the graphene $|E_F|$ between 0.65 eV and 0.45 eV. For V_G = 0 V, the graphene monolayer in our GMR is already heavily doped, which allows dispersion tuning with low loss.

Figure 3.2b maps the calculated real and imaginary parts of the GMR, varying with $|E_F|$ and wavelength λ. In the two maps, the blue curves denote the boundary where dispersion abruptly changes, and the yellow curve denotes the low-loss region. In our measurement, we apply a high-power continuous-wave pump at 1,600 nm. At this wavelength, when we tune $|E_F|$ from 0.45 eV to 0.65 eV, the effective refractive index n_{eff} is controlled from 1.789 + 0.058i to 1.781 + 0.001i. Figure 3.2c shows the measured transmission and free spectral range (FSR; the wavelength spacing between successive maxima) dependences of the GMR, at different gate voltages. In this measurement, a broadband tunable laser serves as the light source at less than 10 mW, below the comb generation threshold. For a selected resonance around 1,600 nm, when V_G is tuned from 0 V to -2 V, the extinction ratio increases from 63% to 84%, and the resonance linewidth decreases from 3.1 pm to 1.6 pm. The mode deviation from equidistance, $D_{FSR} = -\beta_2 c(2\pi f_{FSR})^2/n_{eff}$, is

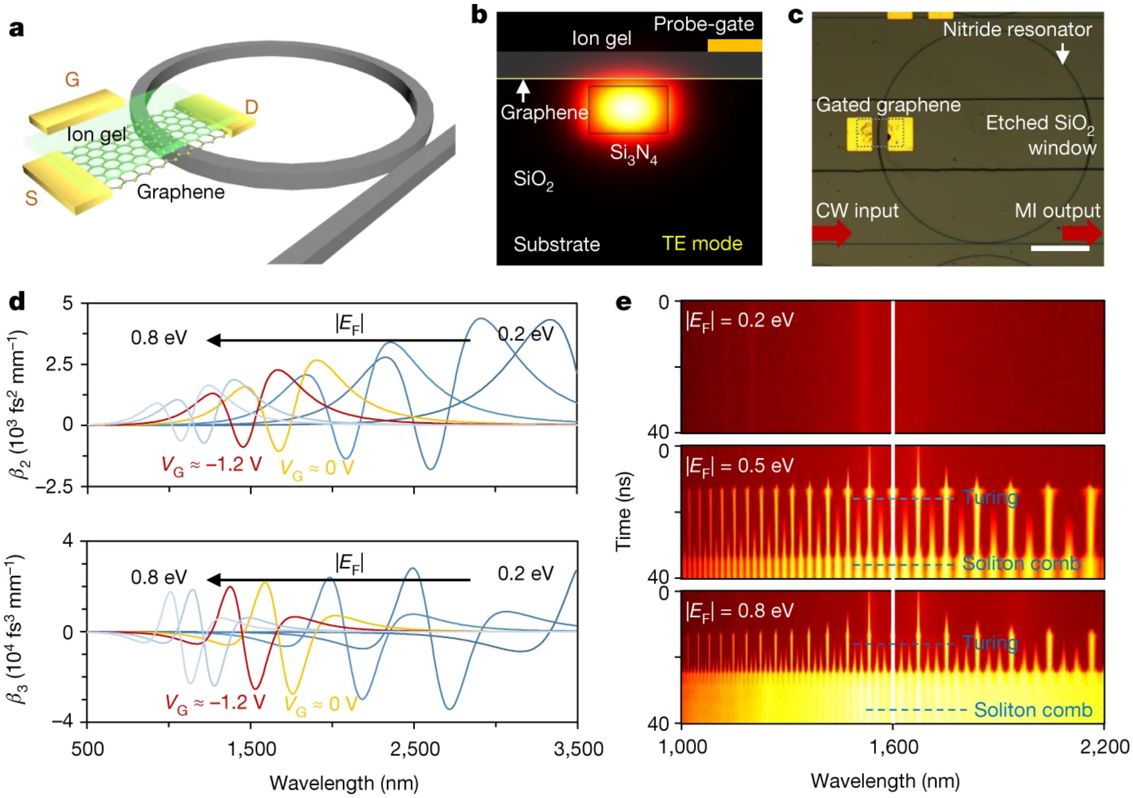

Figure 3.1. a, Schematic architecture of the GMR, with the silicon nitride indicated in grey. A graphene/ion-gel heterostructure is incorporated in the nitride microresonator. b, Electric-field distribution of the graphene-nitride heterogeneous waveguide, with a Si_3N_4 cross-section of $1.2 \times 0.8\mu m^2$. The distance between the Si_3N_4 waveguide and the graphene layer is 100 nm. The graphene and the top-gate probe are separated by 1 μm with the interlayer ion-gel capacitor. In this structure, transverse electric (TE) mode is applied. c, Optical micrographs show the bus waveguide (red arrows), ring resonator and Au/Ti metallized patterns. An etched window is designed to ensure both graphene-light interaction and reduced propagation loss. Here the graphene-covered area is marked by the grey dashed box; the etched window label refers to the whole horizontal area between the two central lines. CW, continuous wave; MI: modulated intensity. Scale bar, 100 μm. d, Calculated group velocity dispersion and third-order dispersion of graphene, depending on its Fermi level. Here, the curves with $|E_F|$ = 0.5 eV and $|E_F|$ = 0.6 eV, corresponding to the experimental conditions, are highlighted in yellow and red respectively. e, Simulated Kerr comb dynamics in the GMR, with different dispersion curves determined by the graphene Fermi level.

320 kHz per mode for $V_G \approx -1V$ (anomalous dispersion) but -45 kHz per mode for $V_G \approx -1.8V$ (normal dispersion), where c is the light velocity in vacuum and f_FSR is the frequency range of the FSR [30]. More details are shown in Figure 3.5.

Figure 3.2d shows the gate-tuning performance of the GMR. When the gate voltage is between 0 V and -2 V, the Fermi level remains higher than 0.4 eV, and thus graphene linear absorption in our working spectral range around 1,600 nm is strongly inhibited by Pauli blocking. As a result, the loaded Q factor of the GMR increases from about 6×10^5 to 10^6, enabling comb generation under a 1-W pump, which is critical for both protecting the graphene monolayer from damage and stabilizing the frequency combs. We also note that Q-factor deterioration is induced by both the etching process and the linear absorption of the graphene heterostructure (Figure 3.6). For applications that require a higher Q factor, other 2D materials such as transition metal dichalcogenides with intrinsic bandgaps (for example WSe2) could be used to construct the heterogeneous microcavities [82]. Simultaneously, the dispersion of the resonator is dynamically tuned, varying continuously from -62 $fs^2\,mm^{-1}$ anomalous dispersion to +9 $fs^2\,mm^{-1}$ normal dispersion. The group velocity dispersion tuning mainly results from the graphene's Dirac-Fermi dynamics [83], with smaller contributions from the ion transport and thermal effects in the ion gel.

3.4 Observations of the gate-tunable graphene Kerr frequency combs

Next, we pump the GMR with 2-W continuous-wave laser power, with the primary comb lines (the strongest frequency combs generated from modulation instability initiation) shown in Fig. 3.3a under different gate voltages. For applied V_G = -1 V, -1.2 V and -1.5 V, the frequency offsets between the primary comb line and the pump Δf_{pri}, proportional to $(1/\beta_2)^{1/2}$, are observed at 2.36 THz, 3.25 THz and 7.17 THz, respectively. When V_G = -1.8 V, the group velocity dispersion of the GMR becomes positive and hence it becomes harder to phase-match without local mode-crossing-induced dispersion. Figure 3.3b shows the optical spectra under carefully controlled laser-cavity detuning. In particular, at V_G = -1 V, $\beta_2 \approx -62\, fs^2\, mm^{-1}$ and $\beta_3 \approx -9\, fs^3\, mm^{-1}$, the Kerr comb has a span of about 350 nm, with highly symmetrical shape. Interestingly, with V_G = -1.2 V, $\beta_2 \approx -33\, fs^2\, mm^{-1}$ and $\beta_3 \approx -630\, fs^3\, mm^{-1}$, we observe a frequency comb spectrum spanning 600 nm, consistent with the general route of a smaller group velocity dispersion bringing about a broader comb spectrum. The comb spectrum is highly asymmetric, with the red-side comb line intensity contributions from Cherenkov radiation. The spectral peak of the Cherenkov

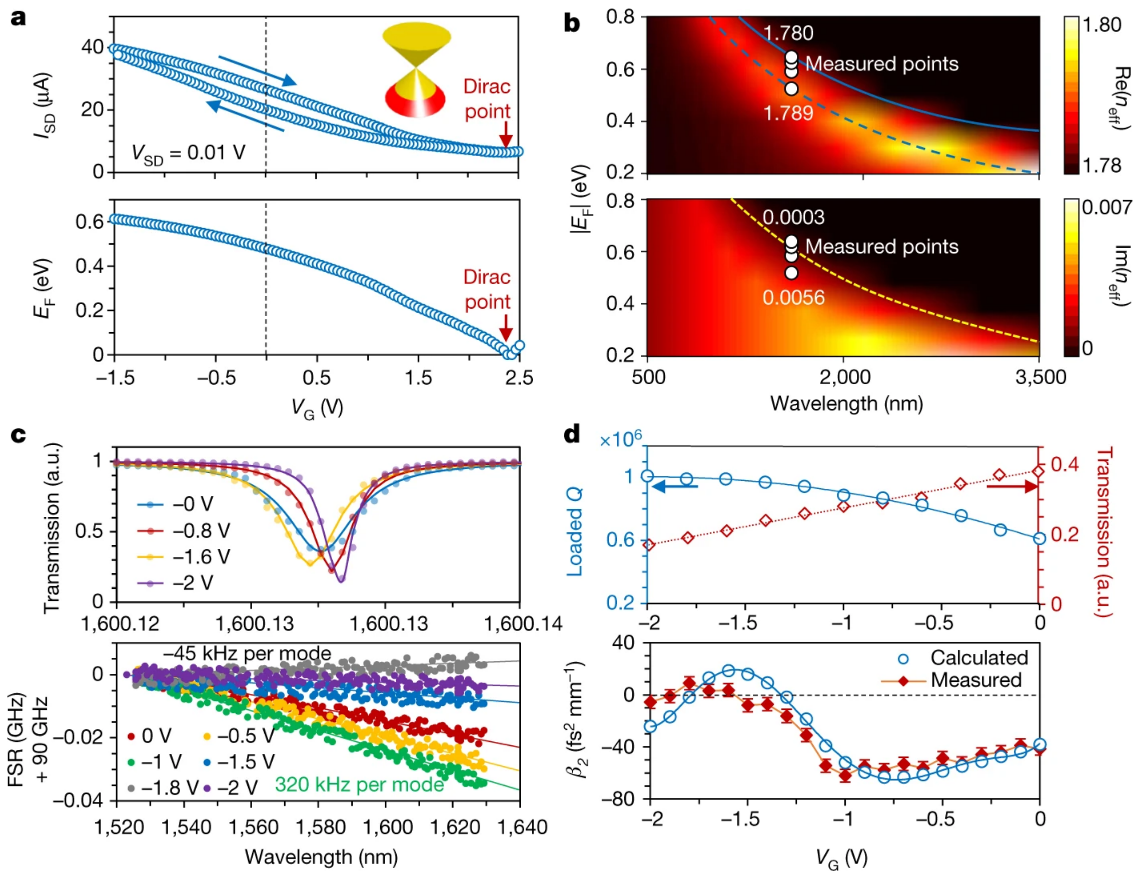

Figure 3.2. a, Electronic measurement of the graphene/ion-gel capacitor. At a source-drain voltage V_{SD} = 10 mV, the correlation between V_G and I_{SD} shows the Dirac point position and tunable Fermi level of the graphene layer. b, Theoretically modelled n_{eff} of the GMR as a function of Fermi levels and optical wavelengths, in which the dispersion and Q can be deduced from the real and imaginary components. Measured data points are shown in white, at a wavelength of 1,600 nm, with $|E_F|$ from 0.5 eV to 0.7 eV. c, Measured transmissions (top panel) and mode FSR (bottom panel; dots, measured; curves, linear fitting) of the GMR, under gate voltages V_G from 0 V to - 2 V. d, Tuned Q factor and dispersion, under various V_G. The]textitQ factor increases from 6×10^5 to 1×10^6 as the group velocity dispersion is controlled between - 62 $fs^2\,mm^{-1}$ and +9 $fs^2\,mm^{-1}$. Error bar is the measurement uncertainty estimated from FSR measurements under the same condition.

radiation is determined by $3\beta_2/\beta_3$, matching the measurement results. In addition, such soliton perturbation and energy transfer can be used to stabilize the Kerr frequency comb [28]. When V_G = -1.5 V, $\beta_2 \approx -8\,fs^2\,mm^{-1}$ while $\beta_3 \approx -213\,fs^3\,mm^{-1}$. Because β_2 here is small (less than $10\,fs^2\,mm^{-1}$), it does not support a stable Kerr comb, the observed comb lines are not even, and the Cherenkov peak in the spectrum is also indistinguishable.

Figure 3.3c summarizes the gate tunability of the graphene Kerr combs, with V_G from 0 V to -2 V. For primary comb lines, their relative spectral location $\Delta f_{pri} = |f_{pri} - f_{pump}|$ is strongly controlled, moving from 2.3 THz to 7.2 THz as V_G only changes from -1.0 V to -1.5 V. This modulation is also influenced by the slight nonlinearity enhancement introduced by the graphene. For the full-span combs generated without missing comb lines, we also demonstrate electric-field control of their spectral span, from 38 THz to 82 THz with V_G from -1.0 V to -1.3 V (for this device, $|V_G|>$ 1.3 V does not show a good coherent comb state). Moreover, we note that the gate-tuning changes the FSRs of the combs, from 89.6 GHz at -1.0 V to 89.9 GHz at -1.5 V. Such optoelectronic tunability enables different Kerr frequency combs with a variety of properties to exist in the same device. Figure 3.3d next illustrates the measured locations of the Cherenkov radiation peaks in comparison with the computed designs. In contrast to the primary comb lines, the third-order dispersion plays an important role in the Cherenkov radiation. We observed three Cherenkov peaks in the window from 1,400 nm to 2,000 nm, with spectral locations $\Delta f_c = |f_c - f_{pump}|$ at values of 26.3 THz (V_G = -1.2 V), 49.2 THz (V_G = -1.3 V) and 17.7 THz (V_G = -1.5 V). The measured results well match the analytic calculation. In Fig. 3c and d, results are collected in the region of -0.4 V to -1.6 V, because when V_G is more than -0.4 V, the Q factor of the GMR is too low for comb generation; and when V_G is less than -1.6 V, the group velocity dispersion is too small to ensure a stable comb.

We estimate the modulation speed of the GMR in Fig. 3e. With V_G tuning, the output comb line intensity within the filter window is modulated temporally. The modulation speed here is bounded by ion diffusion in the heterostructure, large ion-gel capacitance on the graphene, and the optical filter bandwidth. In our current proof-of-principle demonstration, to ensure that $|E_F|$ is sufficiently high, we use the ion-gel-based capacitor, the large capacitance (7.2 $\mu F\, cm^{-2}$) and slow ion diffusion (about $10^{-10}\, m^2\, s^{-1}$) of which limit the charge-discharge operation speed to less than hundreds of kilohertz. The optical filter bandwidth can be narrowed to improve the detection rate of the modulation by almost 7.5 times. In Fig. 3e, we show the modulated signal-to-noise ratio with a radio frequency spectrum analyser, by using optical filters with passband widths of

50 nm, 9 nm and 2 nm, respectively. Their corresponding bandwidths are 80 kHz, 200 kHz and 600 kHz (Figure 3.7). Although sub-megahertz modulation for the primary comb is successfully demonstrated, we note that fast modulation while preserving the full-grown Kerr comb across the entire modulation cycle could be much more challenging: with V_G tuning, not only the group velocity dispersion but also the FSR of the GMR is tuned. Compared with the primary combs shown in Fig. 3.3a, phase-matching of the full combs in Fig. 3.3b is much more sensitive: a slight variation in the FSR from the gate modulation may cause the Kerr comb to collapse. To achieve reliable, fast on-off switching in full-generated Kerr combs, inverse FSR compensation (for example, by temperature feedback) should be applied. Such sub-megahertz tunability for a Kerr comb could potentially be used in applications [84] such as precision measurements.

Dispersion is one of the most critical cavity parameters that defines the Kerr frequency comb dynamics. The broadband dispersion modulation controlled by the gate voltage of the graphene-nitride microresonator opens up the possibility of dynamically selecting the formation path of dissipative Kerr solitons and frequency combs. By using the gate-tunable GMRs, we can engineer the dispersion dynamically to form different soliton states through electrical control. With a fixed pump power of 2 W, Fig. 3f counts the soliton states achieved in measurements for gate voltages in the range -1.6 V to -1.1 V, with the experimental conditions otherwise kept constant. In total, we have found soliton states with soliton numbers of 12, 11, 9, 8, 6, 5 and 4. More theoretical calculations and simulations are discussed in section B.1.3.

3.5 Soliton crystals of the gated graphene-nitride microresonator

Figure 3.4 demonstrates four specific examples of soliton crystal states, under optimized gate voltages. Here the left panels show the measured intensity transmission, the middle panels demonstrate the optical spectra, and the right panels illustrate the frame-by-frame frequency-resolved second-harmonic autocorrelation maps. These soliton states with low RF noise are achieved following Turing patterns and chaotic states before transition into the soliton states (Figure 3.8). This is characterized by a transmission step, by tuning the pump laser gradually into the cavity resonance.

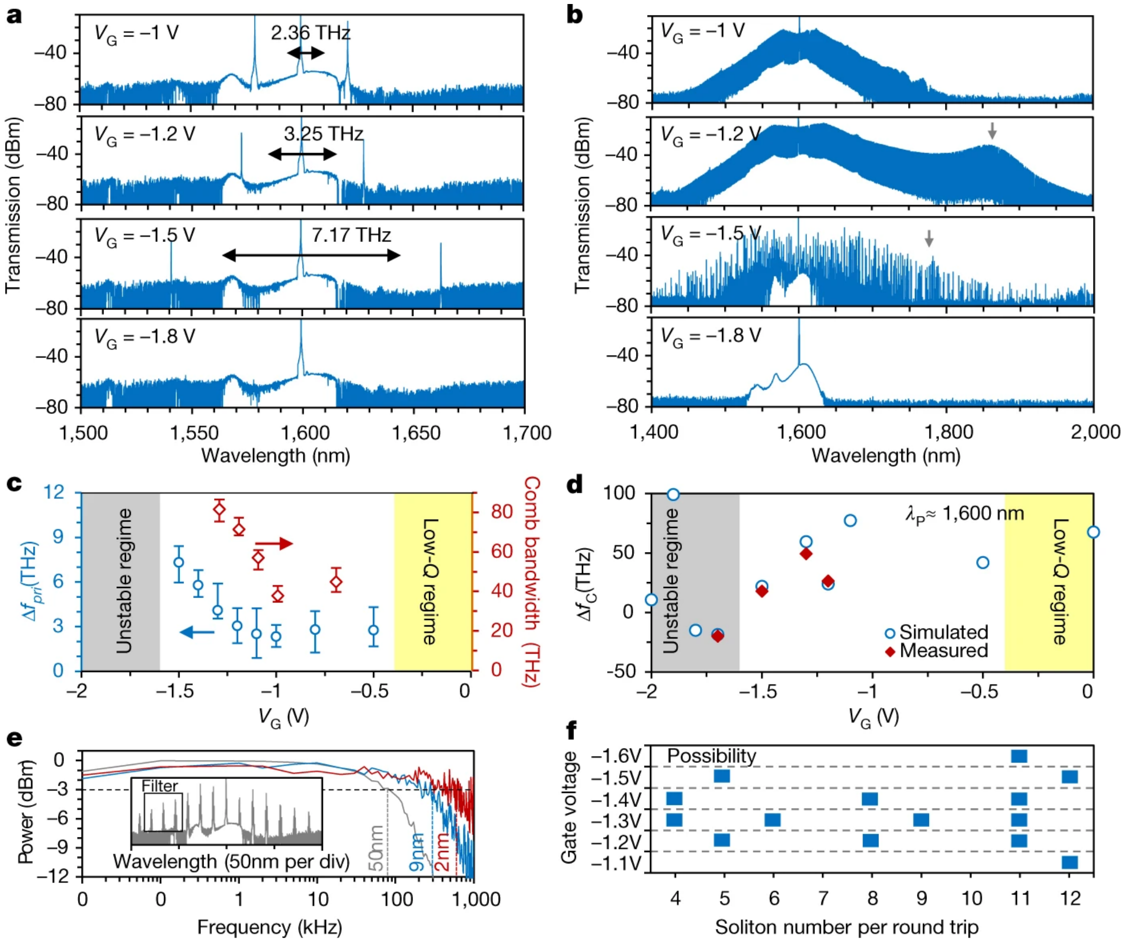

Figure 3.3. a, Primary comb lines at controlled gate voltages and Fermi levels of graphene. b, Full frequency combs generated under gate voltages of - 1 V, - 1.2 V, - 1.5 V and - 1.8 V. Here the launched pump power is fixed at 34.5 dBm. Kerr combs are generated by fine adjustment of the pump wavelength. Peaks of the Cherenkov radiation are marked by the grey arrows. c, Gate voltage tunes not only the primary comb line locations (blue circles) but also the full comb bandwidth (red diamonds). d, Frequency spacing between the continuous-wave pump and the Cherenkov radiation, which is proportional to β_2/β_3. e, 3-dB modulation bandwidths of 80 kHz, 200 kHz and 600 kHz are demonstrated by using optical filters with passband bandwidths of 50 nm, 9 nm and 2 nm respectively. The modulation speed is currently bounded by the ion-gel capacitance. f, Statistical distribution of the measured soliton states, with the same experimental parameters except for V_G which is tuned from - 1.1 V to - 1.6 V.

Figure 3.4a shows two examples of the soliton state with missing pulses, at a gate voltage of -1.2 V. The corresponding pump laser wavelength is around 1,600.2 nm. The optical spectra of these states are characterized by the apparent existence of groups of comb lines that are separated by multiple cavity FSRs. Within each comb group, weaker single-FSR comb lines are present, and they effectively connect all comb groups without any spectral gaps. For the examples shown in Fig. 3.4a and 3.4d, the comb groups are separated by 8 FSR, 5 FSR and 12 FSR respectively. In the time domain, the autocorrelation traces reveal the common features of missing pulses in the otherwise equally spaced soliton states with higher effective repetition rate. The self-organization of multiple soliton pulses into a train of equally spaced pulses resembles the crystallization process and is therefore termed a soliton crystal [85], and the missing pulse structure is analogous to defects in crystal lattices. Our graphene-nitride heterogeneous microresonator thus provides a platform for study of soliton physics that is tunable through the gate-voltage and Fermi level. We also note that when the soliton crystals are formed, the emitted soliton Cherenkov radiations are sharp and narrow, as marked by the grey arrows in Fig. 3.4.

Soliton crystals are formed because of the strong mode interaction and intracavity interferences, and thus their evolution dynamics depend critically on the exact dispersion profile of the microresonator. By further optimizing the group velocity dispersion and third-order dispersion through gate tuning, we demonstrate two periodic soliton crystal states. Figure 3.4b shows a four-soliton state with V_G = -1.3 V and pump laser at approximately 1,584.2 nm, while Fig. 3.4c shows a 11-soliton state with V_G = -1.4 V and pump laser at approximately 1,600.1 nm. Intriguingly, these soliton crystal states show remarkable stability, and they can robustly survive a pump power fluctuation up to ± 2 dB, or wavelength offset up to ± 300 pm. The soliton crystal formation is also akin to harmonic mode-locking in which a stable high-repetition-rate pulse train can be attained even in longer cavities, and it is of interest in applications such as high-speed communication, comb spectroscopy and data storage. This realization of a charge-tunable graphene heterostructure for controllable frequency combs and soliton dynamics opens a new architecture at the interface of single-atomic-layer nanoscience and ultrafast optoelectronics.

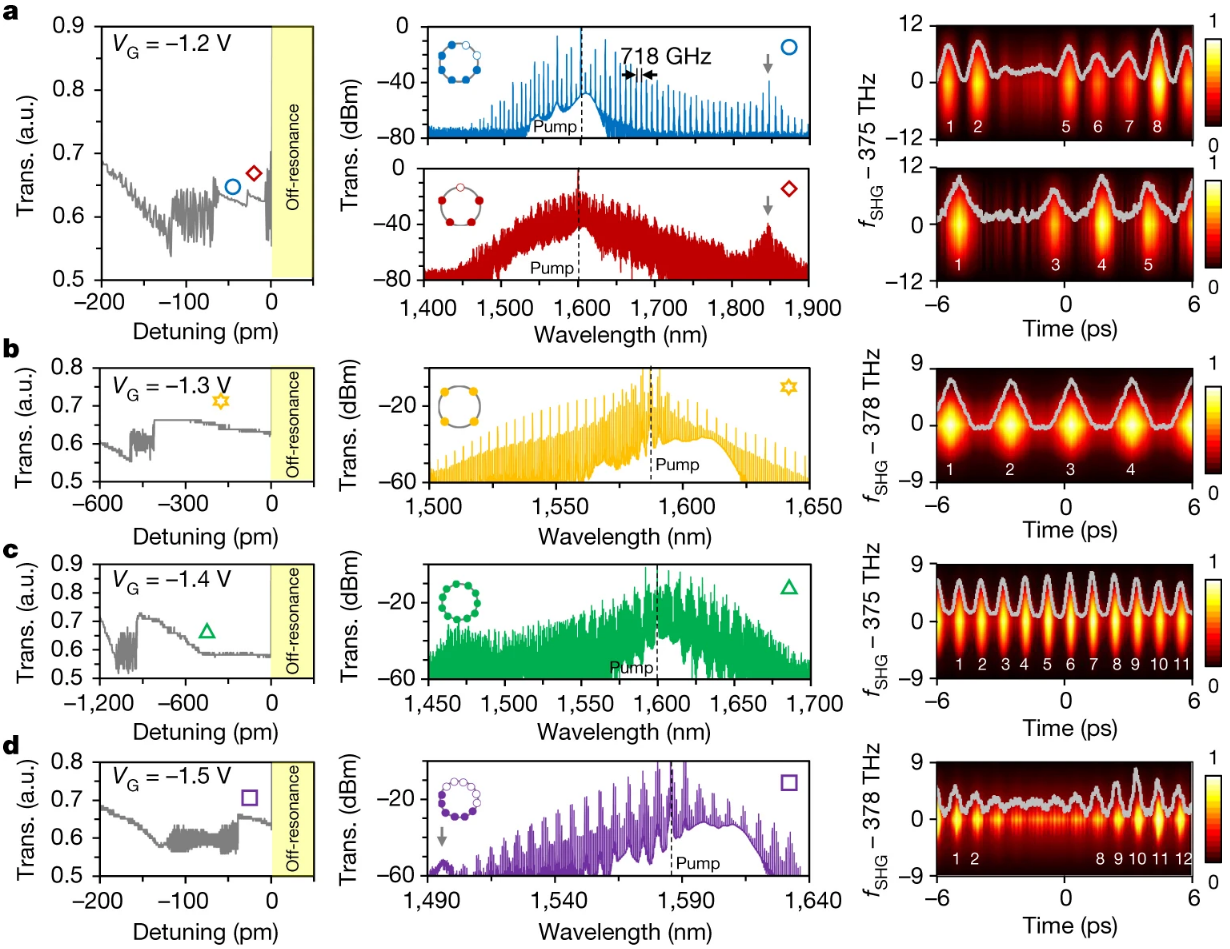

Figure 3.4. a, d, Soliton state with crystal-like defects including the single-soliton defect in a. b, c, Periodic soliton crystal states with equally spaced soliton pulses. Panels a to d are achieved with gate voltages V_G tuned at different values, ranging from - 1.2 V in a to - 1.5 V in d. Left panels: measured intensity transmission, illustrating the characteristic 'steps' associated with soliton formation. Middle panels: corresponding optical spectra measurements. The pump locations are marked by black dashed lines and the Cherenkov radiation peaks are marked by grey arrows. Right panels: frequency-resolved second-harmonic autocorrelation maps of the soliton pulses. Here the grey curves show the real-time autocorrelation intensity traces.

3.6 Extended Data

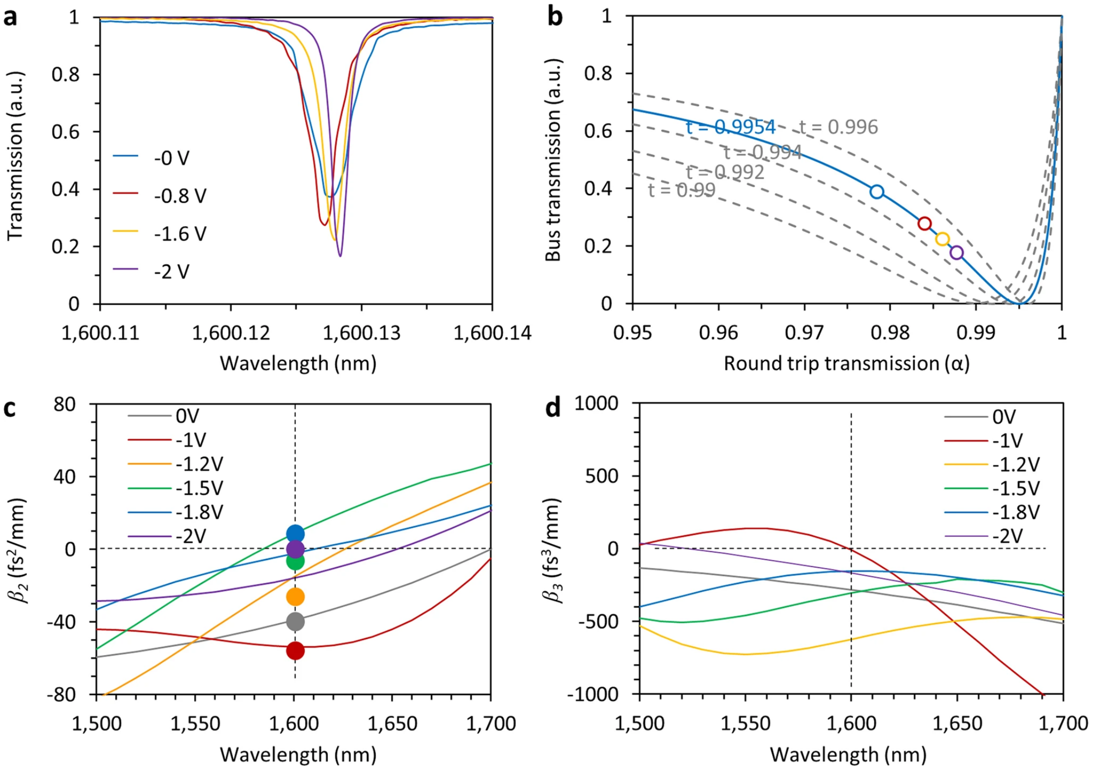

Figure 3.5. a, Dips at approximately 1,600 nm, with different V_G. b, Correlation of the round-trip transmissions and the bus transmissions for the resonator, obeying $T = (\alpha - |t|)^2/(\alpha - \alpha|t|)^2$. Here, $1 - \alpha$ is the cavity loss per round trip, and $1 - t$ is the bus-to-cavity coupling rate. In our experiment, the graphene ring resonator is under-coupled originally, as the blue dot shows. c, Group velocity dispersion in range of 1,500 nm to 1,700 nm. Here, the curves show the calculated results, while dots show measured data. d, Calculated third-order dispersion in range of 1,500 nm to 1,700 nm.

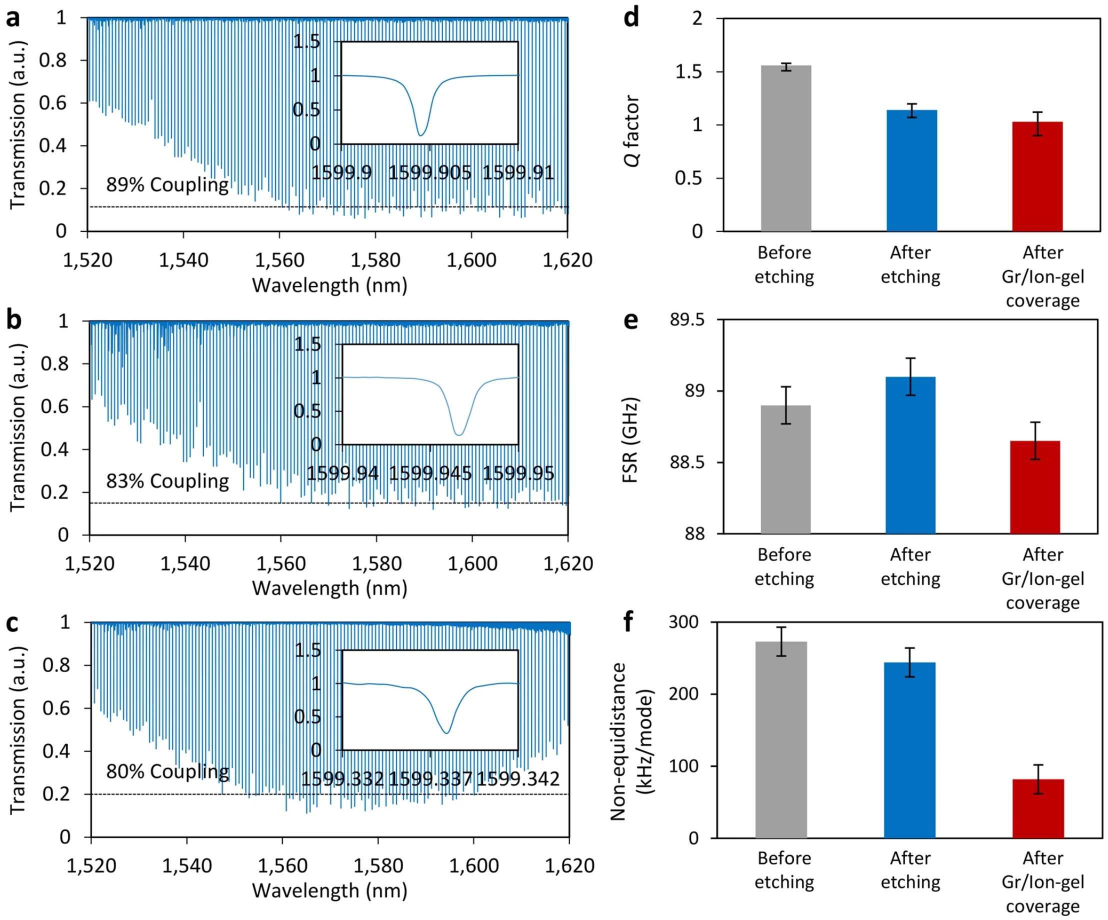

Figure 3.6. a, Spectral transmission of the silicon nitride ring resonator under the silica overcladding. b, Spectral transmission of the silicon nitride ring resonator after buffer-oxide etching to remove the silica overcladding. c, Spectral transmission of the graphene/ion-gel-based nitride ring resonator, heavily p-doped (V_G = -2 V). d, Loaded Q factor around 1,600 nm. e, FSR, which is sensitive to the geometry modification. f, Mode non-equidistances, D_2. d and e are measured at λ = 1,600 nm. In this figure, the error bars denote the typical system error.

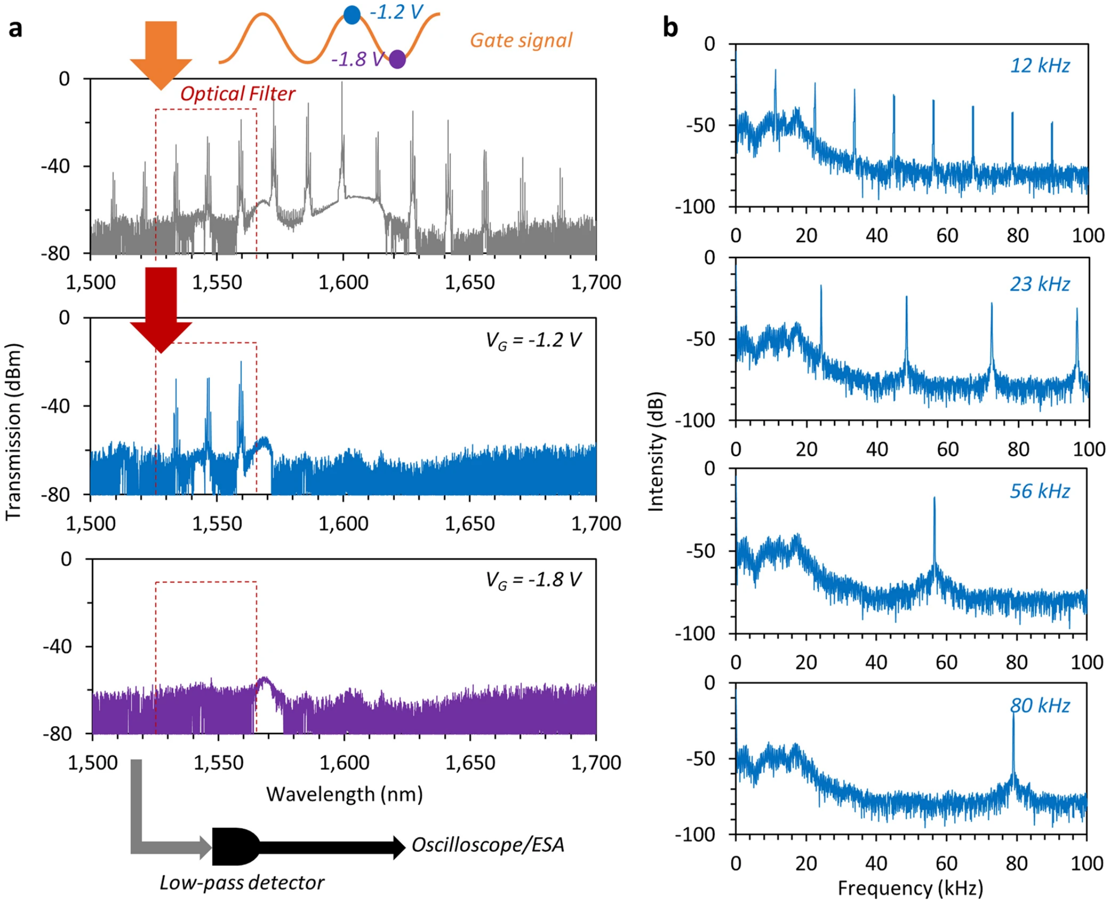

Figure 3.7. a, Method for measuring the modulated comb. Keeping bias VG = -1.2 V, we control the laser-cavity detuning to generate a primary comb such as the grey spectrum shown here. To filter off the 1,600-nm continuous-wave pump, we apply a C-band filter, selecting the comb lines in the C-band only. A signal generator (maximum amplitude of 2 V, HP3312) is applied to modulate the gate voltage between - 1.2 V and - 1.8 V. In this process, primary comb lines in the filter window are modulated by the gate signal; the modulation is monitored by using an oscilloscope (500 MHz, Rigol DS1054) and an electrical spectrum analyzer (ESA, 3 GHz, Agilent CXA9000A). b, Examples of radiofrequency spectra of the modulated combs, filtered by an optical filter (1,530 nm to 1,570 nm).

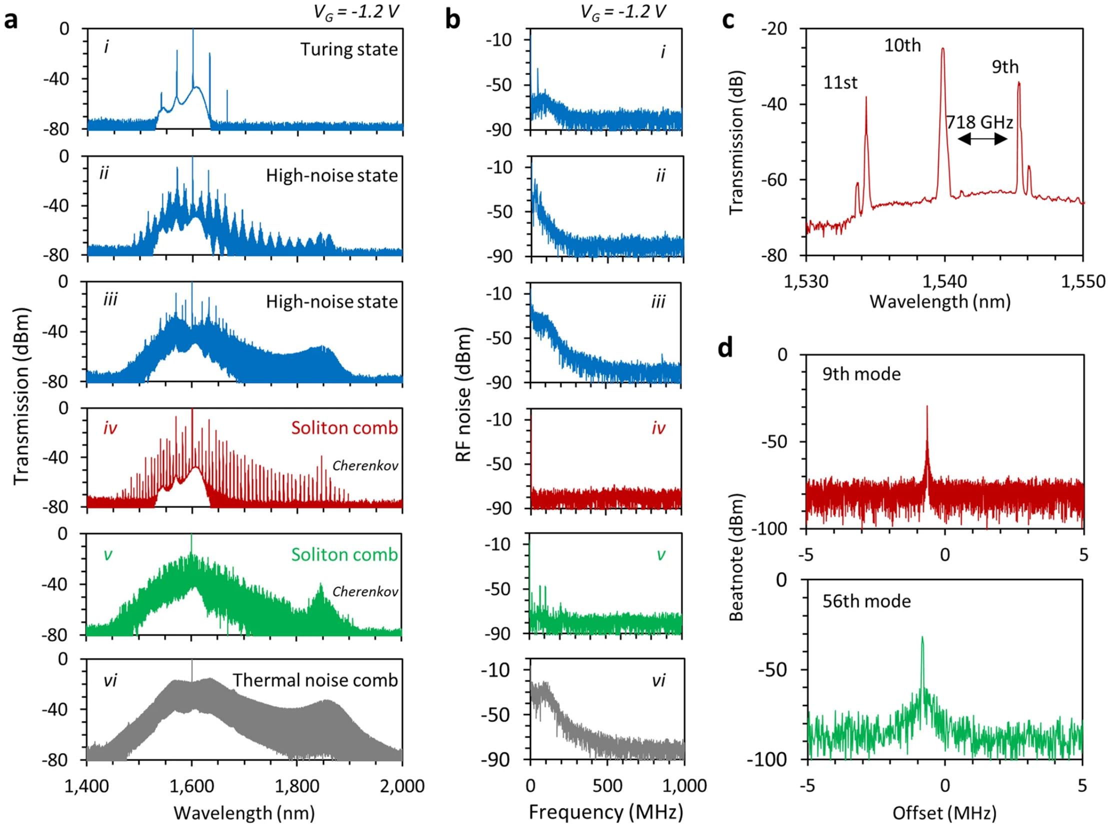

Figure 3.8. a, Under V_G = - 1.2 V (Fermi level 0.59 eV), when the wavelength of the pump (λ_p) is tuned from 1,600.00 nm to 1,600.23 nm, the Kerr frequency comb is generated gradually. When λ_p is tuned between 1,600.15 nm and 1,600.19 nm, two multi-soliton states with low phase noise are achieved (states iv and v). b, Corresponding radiofrequency (RF) amplitude noise of the six states. In a and b, the pump power is kept at 34.5 dBm. Cherenkov radiation of the multi-soliton comb is narrow and sharp. c, Zoom-in of the eight-soliton crystal spectrum. The FSR changes from 89 GHz to 718 GHz, owing to the soliton-crystal-based longitude mode interaction. d, Beat note for the comb lines of the eight-soliton state (red; ninth comb line offset from the pump) and the four-soliton state (green; 56th comb line offset from the pump).

3.7 Methods

3.7.1 Theoretical Analysis

The refractive index of graphene, n_G, is determined by its permittivity ε_G as $n_G = \varepsilon_G^{1/2}$, where $\varepsilon_G = \{-Im(\sigma_G) + iRe(\sigma_G)\}/\{2\pi f \Delta\}$ [73]; here σ_G is the conductivity of graphene, f is the optical frequency, and Δ = 0.4 nm is the thickness of the graphene monolayer. Particularly, $\partial^n Re(n_G)/\partial\lambda^n$ determines the n^{th}-order dispersion, while $Im(n_G)$ determines the waveguide loss. In section B.1.1, we describe in more detail how the transmission of graphene is determined by its quasi Fermi level E_F. By gating graphene via an external field, one can conveniently control both the group velocity dispersion β_2 and the third-order dispersion β_3 of a graphene monolayer. Kerr comb generation in the time domain is governed by the well-known Lugiato-Lefever equation in the GMR. In section B.1.2, we describe the third-order nonlinearity of graphene. In section B.1.3, we provide detailed simulations of the soliton generations in the GMR.

3.7.2 Device design

First, in a silicon foundry, we nanofabricated a high-Q silicon nitride microresonator with measured loaded $Q \approx 1.6 \times 10^6$ (intrinsic $Q \approx 1.8 \times 10^6$) and $FSR \approx 90GHz$ in a 350-μm-diameter ring structure. The nitride core has a $1,200 \times 800nm^2$ cross-section, a 600 nm gap to the input-output coupling waveguide of $1,000 \times 800nm^2$ cross-section, and a top oxide cladding. Next, single-atomic-layer graphene was grown using a chemical vapour deposition method and transferred onto the exposed region of the nitride ring (with etched SiO2 window). The monolayer graphene was then lithographically patterned and oxygen plasma etched into an $80\mu m \times 100\mu m$ sheet. Metallization of source-drain electrodes was achieved through standard photolithography, followed by electron-beam evaporation of Ti/Au (20/50 nm thick). Here the electrode pad size was $80\mu m \times 60\mu m$. Subsequently, we integrated an ionic liquid (DEME-TFSI, N,N-diethyl-N-methyl-N-(2-methoxyethyl)ammonium bis(trifluoromethanesulfonyl)imide) as the gate dielectric, resulting in an electric double-layer graphene transistor. More details are shown in section B.2 and figure B.9.

3.7.3 Experimental set-ups

We implemented a temperature-controlled optical set-up for the frequency comb generation. The spectral tunable range of our drive laser is 1,480 nm to 1,640 nm, and the maximum output power of our erbium-doped fibre amplifier (EDFA, BKtel) in the L-band is 3.16 W (35 dBm). The GMR transmission is measured by using the same tunable laser, swept through its full wavelength tuning range at a speed of 40 $nm\, s^{-1}$, to obtain dispersion and Q factors. A fibre-coupled hydrogen cyanide gas cell (HCN-13-100, Wavelength References Inc.) and an unbalanced fibre Mach-Zehnder interferometer are used for calibration. To measure the stability and soliton states of our frequency comb, heterodyne and autocorrelation measurements are implemented. For the heterodyne measurement, a stable continuous-wave laser with narrow linewidth (300 kHz, New Focus) is applied as the heterodyne reference for the beat notes. For the autocorrelation measurement, a fibre with zero group velocity dispersion, made of a 7-m dispersion-compensating fibre and a 15-m single-mode fibre, is used to guide the microresonator output to the autocorrelation set-up with minimal pulse broadening and distortion. More details about the experimental set-ups are shown in figures B.10, B.11, B.12, B.13.

3.7.4 Soliton-step evolution process in the graphene frequency comb

Complementary to Fig. 3.4, Figure 3.8 illustrates the soliton states at a gate voltage of -1.2 V, for different laser-cavity detunings. With the simultaneous optical and radiofrequency spectra measurements, the frequency comb initiates from the Turing pattern (state i) into the high-noise patterns (states ii and iii, with sub-comb competition) before settling down into the low-noise soliton comb (states iv and v). With further detuning, the soliton comb goes back into the high-noise regime (state vi), owing to the thermal instability in the cavity. We then beat the comb lines of the soliton states with a continuous-wave reference laser with two examples for the eight-soliton state (state iv) and the four-soliton state (state v). Here, the 9th mode and the 56th mode denote the offsets from the pump line. The beat notes show an intensity contrast ratio of more than 40 dB, with a linewidth of 200 kHz, verifying that there is clean and stable soliton generation.

3.8 Summary

Here we demonstrate the gated intracavity tunability of graphene-based optical frequency combs, by coupling the gate-tunable optical conductivity to a silicon nitride photonic microresonator, thus modulating its second- and higher-order chromatic dispersions by altering the Fermi level. Preserving cavity quality factors up to 10^6 in the graphene-based comb, we implement a dual-layer ion-gel-gated transistor to tune the Fermi level of graphene across the range 0.45-0.65 electron-volts, under single-volt-level control. We use this to produce charge-tunable primary comb lines from 2.3 terahertz to 7.2 terahertz, coherent Kerr frequency combs, controllable Cherenkov radiation and controllable soliton states, all in a single microcavity. We further demonstrate voltage-tunable transitions from periodic soliton crystals to crystals with defects, mapped by our ultrafast second-harmonic optical autocorrelation.

CHAPTER 4

Ultrafast spectral analysis of breathers and chaos in frequency microcombs

4.1 Introduction

The spontaneous formation of patterns from a homogenous background and from instability has always been a long-standing interest, in fields ranging from developmental biology [86], chemical kinetics far from equilibrium [87], active fluids [88], plasmas [31], ultracold atoms [89] and quantum gases [90], condensation of classical waves [91], free-electron lasers [92], and the formation of fractals and chaos [93, 94]. Arising from stochastic fluctuations, the underlying nonlinear dynamics for the spontaneous pattern formation span across a range of physical systems and, when driven above threshold, can be robust against perturbation and with persistent recurrence events. The Turing model universally casts the complexity of theses self-organized patterns into nonlinear reaction kinetics and diffusion characteristics [95], or equivalently in optics, the nonlinear Kerr medium and group velocity dispersion from space-time duality [96, 97]. In optics and optical physics, Lugiato and Lefever first theoretically proposed the symmetry-breaking instabilities [98] as part of the nonlinear Schrödinger framework [99]. These dissipative structures arise from nonlinear oscillators and chaos [100–102], in the mean-field model of optical bistability and termed as modulation instability [103], and can be described by super- and sub-critical regimes of pattern formations [104, 105] including solitary waves, solitons and rogue waves [106–108].

Recently ensemble measurements on soliton and non-soliton frequency microcombs [25, 35, 60, 109, 110] have reported remarkable progress in broadband spectral generation [12, 28, 32], ultrashort pulse generation [21], low-power operation [33], frequency stabilization [29, 30], and ultrawideband optical communications [39]. In this work we report the persistent formation of real-time chaos, breathers and rogue waves in the nonlinear dynamics of the resonator frequency microcombs, enabled by fast single-shot spectro-temporal metrology. We uncover the intrinsic fluctuations in these confined nonlinear microresonators, supported by the statistical distributions in the different regimes. First, in the frequency microcomb initialization, we examine the chaotic fluctuations and long-tail statistics over multiple parametric comb lines simultaneously. In these chaotic states, we observe the energy transfer through the comb spectrum, aided by the local mode interaction with 4 ns temporal resolution. Second, we unveil the line-by-line dynamical transitions of the breather frequency microcombs. We determined a distinct self-organized phase shift between the breather comb lines, ranging from 0 to $-\pi$ in the same microcomb set, as well as watched the controlled switching from breather-to-breathers along with comb line revivals in the initiation process. Third, we map out the evolution from the spontaneous background noise to microcomb initialization, in which a plethora of rogue waves and their stochastic burst distributions are observed. Under the Fermi-Pasta-Ulam-Tsingou recurrence framework, we analysed the evolution of the rogue wave thresholds and the burst interval asymptotics over more than 400,000 peak event occurrences. Furthermore, we uncover dominant mode spectro-temporal dynamics of giant rogue waves in these nonlinear rare event scenarios.

4.2 Chaotic states and dynamical breather combs in microresonators

Our examined nonlinear resonator is a high-Q silicon nitride microcavity, with intrinsic Q of $\approx 1.3 \times 10^6$, a free spectral range of 17.9 GHz, and a calculated group velocity dispersion of +3.5 fs^2/mm around 1595 nm (detailed characteristics in section A.2) [29]. In this nonlinear resonator, a range of dynamical comb states can be observed, as illustrated in Figure 4.1A and modelled by the time-dependent nonlinear Schrödinger equation under different laser-cavity detunings. The first comb lines are generated via degenerate four-wave mixing when the modulation instability gain exceeds the cavity loss. These comb lines then further mix with the pump to generate a periodic Turing pattern [84]. On further detuning the pump laser, the intracavity intensity evolves to exhibit chaotic fluctuations which then finally collapses to a set of dissipative solitons. In accordance with the time-domain dynamics, fast evolution thus also exists in the spectral domain. To examine the spectro-temporal dynamics, Figure 4.1B shows the schematic setup for the frequency microcomb spectral dynamics observation. First the comb is generated by pumping a silicon nitride spiral resonator with a continuous-wave (CW) tunable laser amplified to 3W with an erbium-doped fiber amplifier (EDFA).

The generated comb is launched into a parametric spectro-temporal analyzer (PASTA) for nanosecond spectral characterization, with spectral filtering to match the measurement system optical bandwidth. Inspired by Fourier imaging, PASTA is a temporal imaging system based on space-time duality, which describes the mathematical equivalence between the paraxial diffraction in the space and narrow-band dispersion in the time. Our PASTA implementation is based on the time-domain analog of a spatial $2f$ system (parameters detailed in section C.2). As shown in Figure 4.1B, if we assume that the signal-under-test consists of several spectral components, the time-lens in PASTA induces a quadratic phase modulation (linear chirp) onto each frequency component and the subsequent dispersive fiber provides an output group-delay dispersion (GDD) equal to the focal GDD. Thus, different wavelength components are focused into transform-limited short pulses with different time delays, realizing the wavelength-to-time mapping. The temporal output waveforms of the PASTA therefore provide a one-to-one mapped spectral information of the input optical signal, with a spectro-temporal metrology that can be obtained at high 250 MHz frame rates using a high-speed photodetector and a real-time oscilloscope. In contrast to prior studies based on dispersive Fourier transform [107, 111–113], our PASTA metrology has increased sensitivity due to its intrinsically energy-conserving process – an enhanced sensitivity that allows us to capture spectral features as low as -30 dBm with a spectral resolution of 22 pm.

We first characterize our PASTA system by measuring the wavelength-to-time mapping ratio, spectral responsivity, and spectral resolution. These parameters are measured by sampling a single-mode laser with the PASTA system and then tuning that laser over a range of wavelengths (further details in section C.3). The wavelength-to-time mapping ratio of the PASTA is measured to be 1.35 ns/nm and the spectral responsivity, which is determined by the conversion efficiency in both stages of FWM and the gain spectra of the EDFAs involved, is characterized over a 5 nm bandwidth.

The spectral resolution is primarily determined by the high-speed PD and oscilloscope. In our system this resolution is measured to be 22 pm (further details in section C.3). In addition, we also characterize the temporal intensity stability of the system, i.e. the intensity fluctuations in the time-mapped spectrum that are attributed to the PASTA system itself. The ratio between standard deviation to mean value of the intensity is measured to be 2% for the femtosecond MLL used to generate the swept pump and 8.6% for the entire PASTA system. The intensity fluctuations obey a clear gaussian distribution (details in section C.3).

Figures 4.1C and 4.1D show two example series of measurements resultantly performed by PASTA where a spectral span of $\approx$ 370 GHz is captured in a 4 ns time window and is refreshed at a rate of 250 MHz. In Figure 4.1C, the comb spectrum corresponds to a state which exhibits chaotic oscillations in time, with each comb line exhibiting distinct time-dependent fluctuations in intensity. In Figure 4.1D, the comb spectrum corresponds to a state with intensity varying periodically in time and at $\approx$10 MHz (much lower than the cavity repetition rate), referred to as a breathing comb. Observed previously in the quasi-steady state [13, 114–116], this state is an example of Fermi-Pasta-Ulam-Tsingou (FPUT) recurrence. In our microresonator, this spectrally-coherent breathing comb arises from modal interactions and sub-comb overlap [13, 115] and is generated with pump laser detuning on the blue side of the cavity resonance, prior to the intracavity field exhibiting chaotic oscillations but after the generation of a Turing pattern. The insets of Figures 4.1C and 4.1D illustrate the steady-state optical spectrum of chaotic and breather state for comparison, wherein the red boxes are the zoom-in spectral regions for detailed PASTA analysis.

4.3 Fast intensity fluctuations and long-tail statistics of the microresonator chaotic states

To extract data on the occurrence of extreme events we perform statistical analysis of the intensity fluctuation for each comb line of the chaotic state. As shown in the dashed trace of Figure 4.2A, the optical spectrum launched into the PASTA system is filtered with an $\approx$ 3 nm bandwidth around the center wavelength of 1544.5 nm, which consists of 15 comb lines. The inset is the RF spectrum

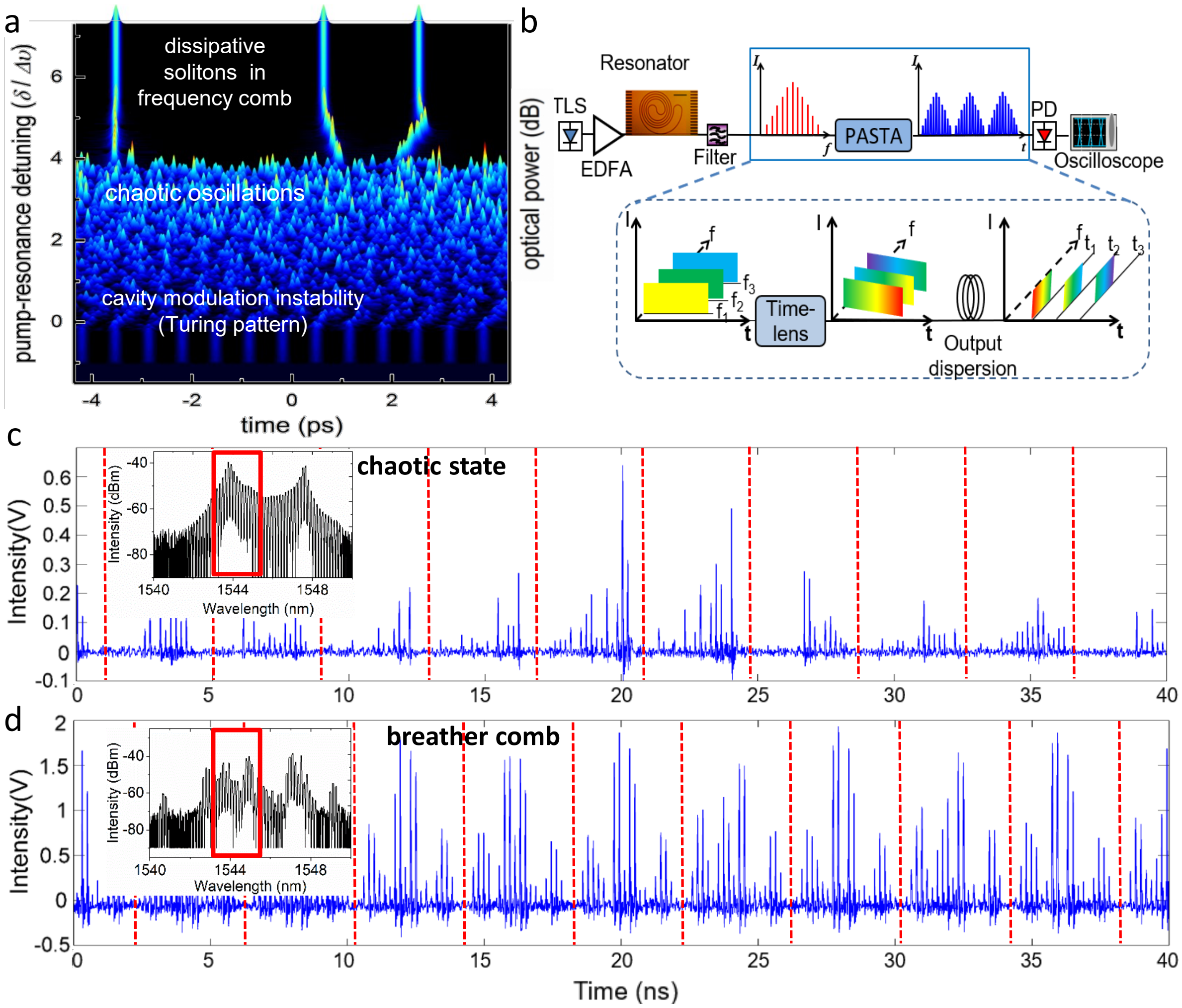

Figure 4.1. a, Nonlinear Schrödinger modeled dynamical evolution of the laser frequency microcomb from spontaneous Turing patterns to chaotic oscillations and dissipative soliton states. b, Real-time spectral mapping at 250-MHz clocking rates of the microresonator frequency combs. The parametric spectro-temporal analyzer (PASTA) is a time-domain analog of a spatial *2f* system, consisting of a time-lens, with a MLL acting as a swept pump to write a quadratic phase chirp onto the signal, and a dispersive fiber. The fiber dispersion is adjusted to be twice the effective 'focal length' of the time lens. This configuration lets us image the spectral information onto temporal waveforms so that spectral fluctuations can be observed in a fast real-time oscilloscope at high frame rates. The spiral microresonator for the dynamical comb formation is illustrated in the top-left. Scale bar: 250 μm. c, Real-time spectrum of chaotic bursts. The dotted red lines denote the temporal duration of each single 4-ns frame. Inset: long- and slow-time averaged spectrum from the same nonlinear microresonator under the same driving conditions, for comparison. The inset red box is the spectral bandwidth measured by our parametric spectro-temporal analyzer. d, Real-time spectrum of a low-noise phase-locked breather microcomb state, sampled at 4-ns frames. Inset: slow-time averaged spectrum, for comparison. The inset red box is the spectral bandwidth measured by our parametric spectro-temporal analyzer.

when the frequency spectrum of the same state is launched into a high-speed photodetector: The broadband RF noise below 500 MHz indicates fast intensity fluctuations of the spectrum, which cannot be resolved by the OSA. As shown in Figure 4.2B, our high spectro-temporal metrology via the PASTA samples the optical spectrum of the signal-under-test at 250 MHz, and thus the spectral shape is displayed on the waveform every 4 ns (as indicated by the red dashed line). In clear contrast to the steady-state OSA measurement, every comb line in the PASTA optical spectrum shows dramatic evolution in each frame. The long-term 1,000-frame-averaged PASTA spectrum, as shown in the red solid trace of Figure 4.2A, still matches the steady-state OSA spectrum quite well.

To visualize the spectral evolution more clearly, the temporal waveform trace in Figure 4.2B is sectioned according to the measurement period to generate a 2D spectral evolution portrait over 1 μs, as shown in Figure 4.2C. The evolution of each comb line is represented by a vertical line and the non-uniform color reflects the intensity fluctuations. In addition, the intensity fluctuation of individual spectral comb lines can be extracted from Figure 4.2C for further analysis. For example, the intensity histogram of nine comb lines around 1544 nm can be obtained and are resultantly shown in Figure 4.2D. Clearly, the intensity histograms of all nine comb lines deviate from the Gaussian-shaped white-noise distribution. Instead, the tails on the higher intensity side are significantly elongated to form an L-shaped distribution, which is an indicator of potential extreme events. Furthermore, the intensity statistics of each comb line exhibit significant differences; comblines which are closer to regions of mode interaction are not only intrinsically brighter but also exhibit more extreme events (longer tails), while comblines which are further away from the regions of mode interaction have a lower incidence of extreme events and shorter tails in the intensity distribution. For example, combline three (D-iii) which is the brightest and at the mode interaction region exhibits the longest tail, with a large number of extreme events (6.8% of recorded samples have a normalized intensity greater than 0.5 for combline 3). As we move to subsequent comblines away from combline three, the tail becomes correspondingly shorter and shorter (only 0.11% of events have a normalized intensity greater than 0.5 for combline 9) as observed in Figure 4.2D. This establishes that, in the presence of mode interaction, different modes experience dramatically different incidences of extreme events. The average cross-correlation between different lines in this state is 0.52, with the maximum cross-correlation of 0.58 between comb line 3 and line 1, indicating that while the combline intensities are moderately correlated, they still exhibit phase incoherence consistent with chaotic oscillations.

4.4 Statistics and dynamical transitions of breather frequency microcombs

We next examine the spectral evolution and dynamics of the breathing frequency comb. As observed in the black dashed curve in Figure 4.3A, the steady-state OSA-measured spectrum has a distinct shape compared with the previous chaotic comb, further details on phase-locked breather comb formation are given in section 2.2. In the corresponding RF spectrum, instead of broadband noise, isolated peaks are observed at specific frequencies, indicating periodic intensity fluctuations of the spectral intensity. To investigate the individual comb line intensity variations, the microresonator output is spectrally filtered with the same filter and launched into the PASTA for real-time observations. 19 comb lines of the breathing comb are observed simultaneously from the temporal waveform of PASTA output. In contrast to the chaos state, the optical spectrum shows much higher stability even under the 250 MHz detection frame rate as shown in the 2D spectral evolution portrait of Figure 4.3B. At around 1544 nm, four comb lines indicated by the two red dashed squares show the highest signal intensity. Unique intensity fluctuations with periodic patterns can be observed on these comb lines. A cross-correlation analysis of the comb lines shows 0.80 for comb lines 1 and 2, 0.88 for comb lines 2 and 3, -0.45 for comb lines 3 to 4, and -0.97 for comb lines 4 and 1. These cross-correlations, different from that above of the chaotic state, are indicative of breathing phase difference between different lines. The relative phase between combline 1 and comblines 2, 3 and 4 are calculated to be -176°, -56° and -36° respectively with combs lines 2 and 3 marching almost in-phase and comb lines 1 and 4 marching out-of-phase. Note that this breathing phase-locked frequency comb is distinct from phase locked states studied previously [117], where combline optical phases vary by multiples of $\pi/2$ or π radians. In this case, the quasi-stable nature of breather comb ensures that we do not require exact phase-matching in each cavity round trip

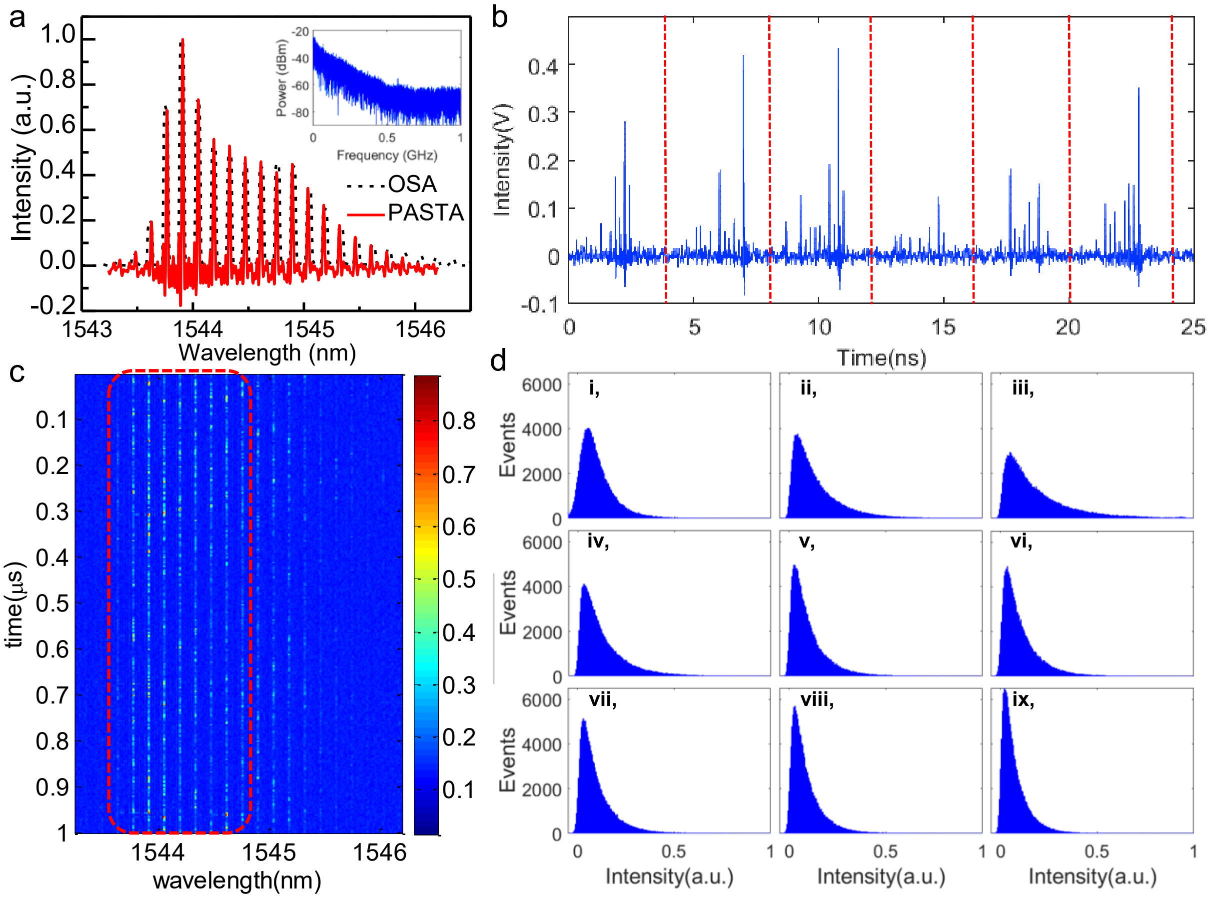

Figure 4.2. (A) Optical spectrum measured by a conventional OSA, with comparison to a post-processed time-averaged spectra of the PASTA system measuring the same chaotic state. The two spectra are in good agreement. Inset: corresponding RF spectrum of the chaotic state. (B) The chaotic spectrum in A sampled at 250 MHz, showing dramatic and rapid fluctuations between neighboring frames. (C) A two-dimensional spectral evolution portrait generated from the PASTA showing the rapid temporal intensity fluctuations of 18 parametric lines. The dotted red box denotes the nine parametric lines selected for further statistical analysis. (D) Normalized intensity histograms of nine parametric lines marked by the red box in C. The long-tails in the intensity distribution indicate an enhanced likelihood for rogue wave occurrence. Furthermore, the difference in intensity distributions between different comb lines, despite their spectral adjacency, indicate the presence of complex energy transfer relationships throughout the spectrum.

and hence generates a continuum of combline phases rather than discrete phase steps. To observe such fluctuations in more detail, the intensity evolution traces of the four selected comb lines are extracted from the 2D portrait and plotted in Figure 4.3C. Each trace is normalized respectively to the peak value. While all comb lines exhibit breather intensity fluctuations, the relative breathing intensity differs significantly. In this specific instance, even when similar periodic patterns can be observed across all of them, the two comb lines on the right (3 and 4) exhibit much higher breathing intensity in comparison to the comb lines on the left. This can be explained by noting the large change in combline phase across points of mode interaction and that breathing intensity is a function of both breathing phase, which determines the regions of the comb most involved in energy transfer to the line of interest, and combline intensity. This is described in further detail in section 4.6.

This periodic oscillation across different comb lines is characteristic of FPUT recurrence and has been observed before in various nonlinear systems governed by the NLSE [118–120] including in breather solitons in microcavities. In microresonator FPUT recurrence, differences in phase of the breathing frequency in distinct parts of the spectrum were attributed to stimulated Raman scattering (SRS). However, in our measurements, SRS is negligible due to the absence of intracavity solitons and we expect the mechanism of breathing to be linked to the strong dispersion disruption caused by mode interaction. The dispersion fluctuation causes a phase mismatch between different modes and affects the phase of the energy exchange during four-wave mixing, leading to distinct breathing phases and intensities for each comb line. This is a rather different mechanism for FPUT recurrence and to our knowledge this is the first time it has been measured in an experiment. Further analysis of the relationship of breathing intensity and phase between different comb lines over a wider spectral range would help to reveal the dynamics of energy transfer between different comb lines (section 4.6), in understanding the principles of microcomb formation.

Next, we examine the fast transition of the comb from a state with a 100 MHz breathing frequency to another state with 70 MHz breathing frequency via the spectro-temporal metrology and controlled by the pump laser-cavity detuning. This transition is shown in Figure 4.3D. As can be observed from Figure 4.3D, the transition between the two breathing comb states is characterized by a drop in energy across the whole spectrum, followed by short revivals in particular comb modes, and finally a sudden increase in intensity of the recorded comb modes, which exhibit intensity oscillations at the new breathing frequency. The mechanism responsible the breathing is depicted in Figure 4.3E. The breathing is due to the primary comb-line spacing not being an exact multiple of the FSR - this mismatch, referred to as a $\Delta - \delta$ mismatch, thus manifests as intensity fluctuations at the breathing frequency. The magnitude of the mismatch depends on both pump power and detuning, in addition the existence ranges of different comb solutions can overlap in power and detuning, while the exact state selected is due to thermal favorability [121]. Therefore as the laser-cavity detuning is changed, at a particular detuning, when the thermal favorability in the cavity shifts away from the current comb state to another simultaneously existing comb solution, there is a rapid phase-transition between the two breathing frequency combs. The breathing frequencies of the two distinct comb states are extracted directly from the Fourier transform of the comb line intensity fluctuations recorded by PASTA and are illustrated in Figures 4.3F-i and 4.3F-ii. The sideband breathers of each state can be understood from the higher harmonics of the breathing tone aliasing back into the range of 0-125 MHz. This aliasing occurs because we have a sampling frequency of 250 MHz and can therefore only directly observe breathing tones up to 125 MHz. Note that in Figure 4.3F-i the primary breathing tone is at 93.9 MHz, while the smaller sideband corresponds to the higher frequency from 187.8 MHz, which is aliased down to 62.2 MHz. Similarly, in Figure 4.3F-ii the primary breathing tone is at 77.9 MHz, while the smaller sideband corresponds to the higher frequency from 155.8 MHz, which is aliased down to 94.2 MHz.

4.5 Intensity distribution of distinct comblines during breather initialization

Figure 4.4A depicts breather comb initialization from the pump background as measured by PASTA. The x-axis is combline wavelength and y-axis is the timescale of evolution. As can be seen comb evolution is not smooth but happens in a series of intensity bursts till there is a final collapse to a stable phase locked breather. These intensity bursts exhibit several extreme events above the Rogue wave threshold calculated by the crest heights criterion. Figure 4.4B plots the number of events at each intensity occurring for 9 selected comb lines (marked in the red box in Figure 4.4A) during breather initialization. The y axis of each graph is plotted in the log scale to clearly show

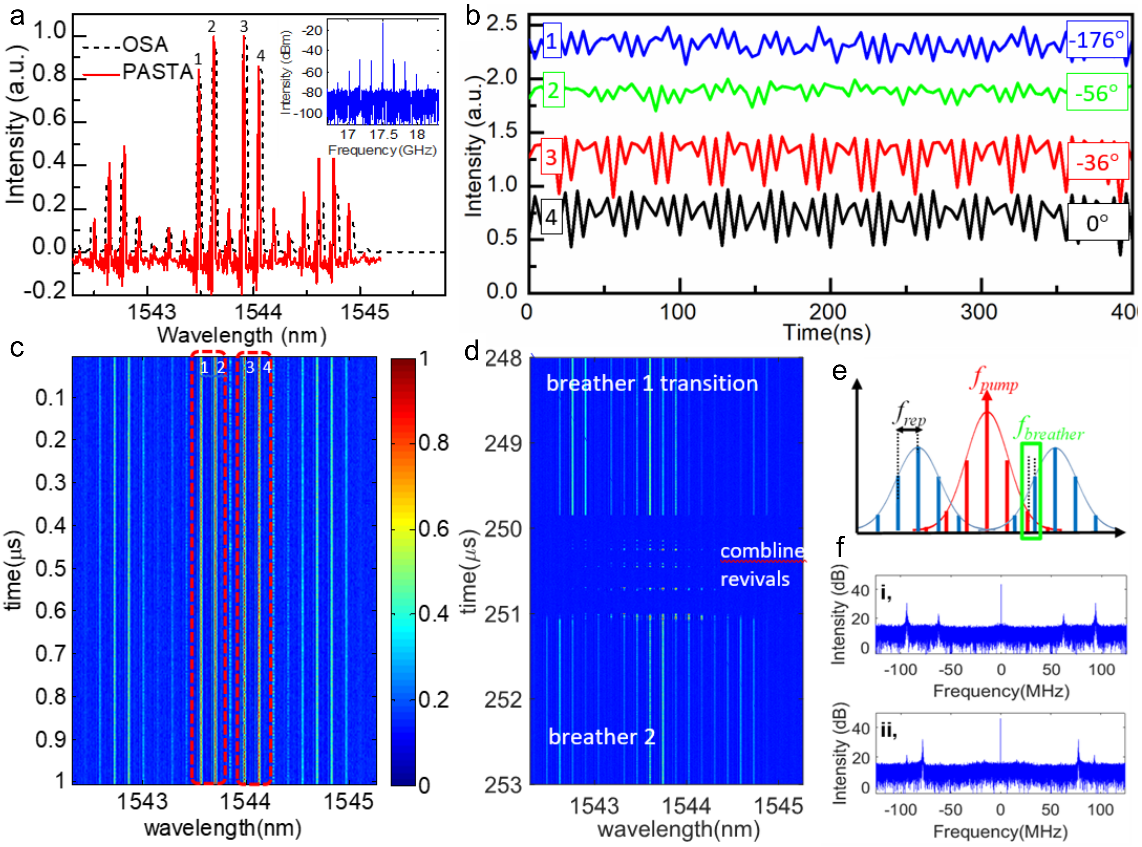

Figure 4.3. (A) Optical spectrum measured by conventional OSA, with comparison to a post-processed time-averaged spectra of the PASTA system measuring the same low-noise breather microcomb. Both spectra are in good agreement. Inset: corresponding RF spectrum of the breather microcomb. (B) A two-dimensional spectral evolution portrait generated from the PASTA showing the rapid temporal intensity variations of 20 comb lines. The dotted red boxes denote the four comb lines selected for further statistical analysis. (C) Example temporal intensity fluctuations for the four comb lines selected in B, illustrating that even adjacent comb lines have large differences in breathing intensities. In addition, there is also a significant phase shift between breathing tones of the selected lines. (D) Transitions between two low-noise breathing comb states, triggered by a change in detuning. The transition is characterized by a sudden loss of power in all measured comb modes followed by a brief revival of certain lines and then a fast transition to the second comb state with a different breathing frequency and optical spectrum. (E) Illustration showing the comb lines of a breather frequency comb with the subcomb around the pump marked in red and adjacent subcombs are marked in blue. Comblines within a subcomb are spaced by exactly FSR, but the spacing between subcombs themselves need not be an integer multiple of FSR, therefore overlap between subcombs generates a breather tone (marked in green). (F-i) An FFT analysis of the power fluctuation of a comb line in the first breather state, plotted in the top half of D, shows two distinct breathing tones. (F-ii) An FFT analysis of the power fluctuation of a comb line in the second breather state, generated after the transition and plotted in the bottom half of D, shows two different breathing tones compared

to the ones retrieved in (F-i), confirming the breather state change

high intensity events. We note the presence of a large peak close to zero, implying most events are of very low amplitude, however we also observe a long tail showing the rare occurrence of extreme events. These events correspond to the bright intensity bursts in Figure 4.4A. In addition we also note that each combline exhibits widely distributed statistics for the occurrence of extreme events, most notably comblines in Figure 4.4B-vi and 4.4B-vii exhibit significantly more large amplitude events than comblines 4.4B-i and 4.4B-ix.

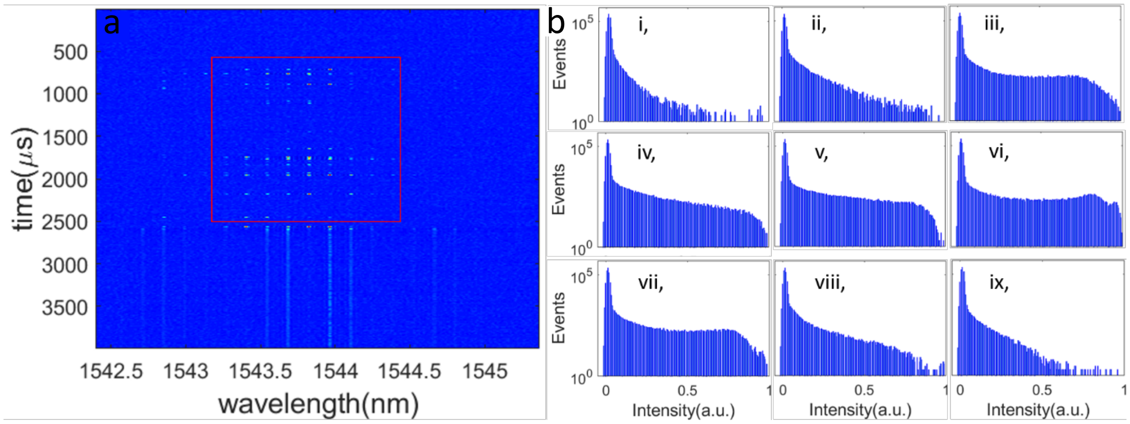

Figure 4.4. (A) The 2D map depicts combline intensity changing with time. The bright spots are high intensity while the low intensity background is blue. We see that a breather comb is initialized with bursts in combline intensity (these intensity bursts are also confirmed with a fast photo detector in the time domain in the main text in Fig. 4). The relatively stable comb state generated at 2500 μs is a breathing frequency comb. (B) depicts the normalized intensity distribution of each combline. The y-axis is in the log scale to clearly show the incidence of high intensity events for each combline.

4.6 Simulated intensity and phase distributions of breather comb lines

We simulate the breather frequency comb by solving the LLE via a split-step Fourier method and then analyzing the time domain evolution of each combline separately. In performing these simulations we also introduce a periodic mode-perturbation via mode shifts ([85]) every 20 modes, which corresponds closely to our experimental resonator profile. The periodic mode interaction seeds complex energy transfer profiles across the comb spectrum. Figure 4.5A, shows the full simulated comb spectrum, the strongest comb lines occur around points of mode-interaction, which leads to a highly modulated spectral profile. Figure 4.5B, shows the RF breathing frequency of the cumulative combline intensity (except the pump). We notice that this is a low noise state with a single breathing tone. To confirm that breathing occurs at different phases across the comb we extract the time domain evolution of three different lines, normalize the amplitude and plot in Figure 4.5C. We clearly see that while the breathing frequency remains the same, the phase changes significantly across these lines. Extending this analysis we plot the breather amplitude normalized to combline intensity in dB in Figure 4.5D, Note that even within subcombs there can be a drastic change in breathing intensity across the mode interaction point. The spectral asymmetry of breathing on either side of the pump is due to TOD in the simulated resonator. Breathing intensity is observed to be a function of combline intensity and breathing phase. In Figure 4.5E we analyze the spectral variation of phase of combline breathing relative to the pump. We confirm here our experimental observation that the phase does not change in steps of $\pi/2$ and π, as measured in prior phase-locked states [117], but rather changes across a continuum.

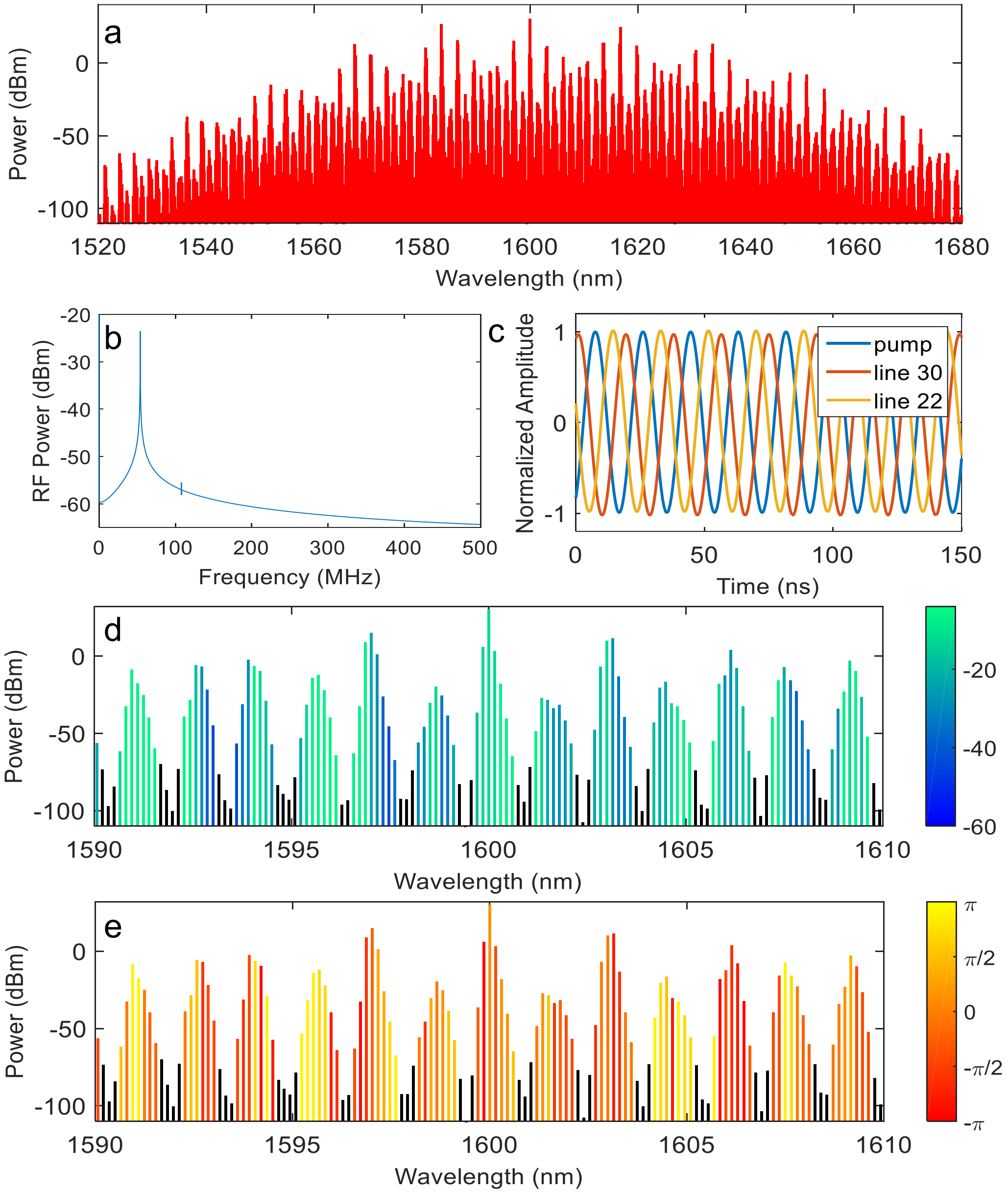

Figure 4.5. (A) Simulated comb spectrum with periodic mode interaction. (B) Comb breathing frequency with single RF tone. (C) Normalized time-domain evolution of three separate comb lines. (D) Distribution of combline breathing amplitude normalized to average combline intensity in log scale. (E) Distribution of combline breathing phase showing a continuum of states.

4.7 Rogue waves and their distributions during the breather microcomb initialization

Figure 4.6A shows a detailed example of the breather frequency microcomb transitions, in the real-time initiation of the breather state. As the pump detuning is increased, the generation of stable breather state is not achieved instantaneously. Instead, the temporal output goes through a stage consisting of large intensity bursts with random intensity and random temporal intervals. In this case, the first such burst is observed at an initiating time of 50 μs, before collapsing and converging into a stable breather state at a time stamp of around 470 μs. We note that such a burst stage is always observed before the breathing state microcomb is reached, and some common features are shared in these bursts. For example, the intervals between bursts, even though highly random initially, exhibits a gradual decrease towards the end of the stage and the duration of the burst usually ranges from hundreds of microseconds to about one millisecond.

We analyze the statistics of these dynamical bursts to understand the initiation process better and to look for extreme event occurrences in the temporal waveforms. The waveform is initially preprocessed to suppress the noise, and the location and intensity of the highest peak are extracted for analysis, with an example in Figure 4.6B (detailed in section C.3). Figure 4.6C subsequently presents the population density function (PDF) of heights extracted from Figure 4.6A and the black dotted line represents the threshold above which peaks correspond to extreme events. The PDF exhibits a long tail, with most events having rather low amplitudes while a small percentage of events (0.6% or less) have heights above 0.5. These are the extreme events. Since the occurrence frequency of events appears to increase over time, we studied the evolution of the pulse occurrence within a sliding window [122] of 20 μs, shifted in 5 μs steps. Figures 4.6D and 4.6E respectively present the evolution of the time intervals and peak height intensities between consecutive pulses. We note that as the pulses become more frequent over time (i.e. shortening time interval between pulses), the threshold for rogue waves increases. A large number of pulses are however still found above the rogue wave threshold, for example in the 500 μs and 1,000 μs time stamps. Interestingly, the interval between pulses, random at first, converges towards a value of 0.3 μs, which exactly corresponds to the time period for breathing oscillations. This chaotic breather has been observed previously in non-linearly coupled oscillator chains in multiple systems [123, 124] and is observed for the first time in microresonator frequency combs. This observation also indicates the deep link between phase-locked breather frequency combs and spatiotemporal chaos.

In order to obtain deeper insight into this process, our spectro-temporal metrology is applied to observe the burst process simultaneously in the spectral domain. Figure 4.6F shows a resulting 3D spectral evolution portrait during the breather frequency comb initialization. Approximately 16 comb lines are simultaneously tracked in the temporal evolution. The total output intensity, calculated by summing the time traces of all comb lines, mainly follows the dynamics of the dominant mode centered around mode 0, with a cross-correlation of 0.72. In this example, at the relative time stamp of 0 μs, all the modes generate pulses at the same time, resulting in a giant rogue wave 5.2 standard deviations above the rogue wave threshold. These large intensity rogue waves are extremely rare cares and rarely found even in our plethora of fast spectro-temporal data. These giant rogue waves are always measured to be correlated with synchronized pulsed energy output in several or all modes. Over the entire span before the breather frequency comb generation, we record 6 giant rogue waves out of 724 rogue events. The high Q of the microresonator we used to generate the breather comb also prevents the intracavity field from changing too quickly, thereby causing the rogue waves to persist for several cavity round-trips. Since we use a detection bandwidth (300 MHz) significantly lower than cavity FSR (17.9 GHz), we also integrate the intracavity field over several round trips and hence the giant rogue waves observed here are due to both higher event intensity coupled with increased extreme event persistence in the cavity.

4.8 Summary

In summary we have utilized a novel technique PASTA to study and characterize various ultrafast phenomenon in Kerr microresonators. This method allows us to capture capture spectral features as low as -30 dBm and provides a spectral resolution of over 22 pm. We have used this method to study in detail the occurrence, spectral characteristics and statistics of extreme events in chaotic

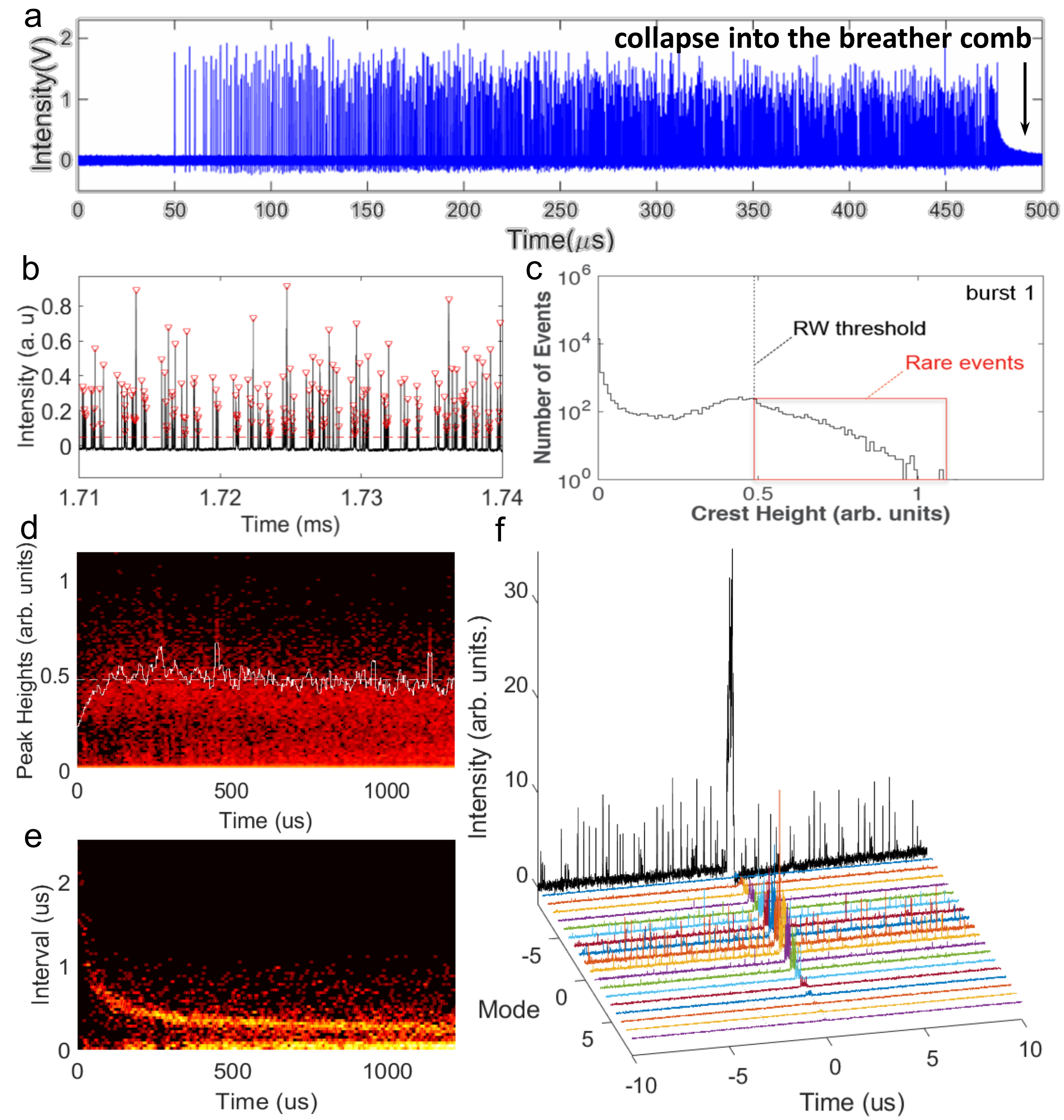

Figure 4.6. (A) Temporal waveform of the microresonator output, showing noise-like intensity bursts before a relaxation into the low-noise breather microcomb. (B) Identification of peak intensities and temporal locations in the burst waveform. The horizontal red-dashed line at the level of 0.05 is the time-averaged intensity threshold. (C) Burst intensity histogram of the waveform in A. The black vertical dashed line represents the crest height threshold of rogue wave formation when all bursts within the evolution are taken into consideration. (D) Evolution of the rogue wave threshold when only the bursts within a finite time window are considered. Red dots represent the normalized peak intensity of the noise burst while the white curve is the threshold value at different temporal positions. (E) Evolution of the burst interval between pulses (identified using the criteria described in B), showing a gradual decrease and convergence towards 0.3 μs. (F) Combline-resolved spectral evolution during the burst initiation. The total output intensity,

calculated by summing the time traces of all comblines, mainly follows the dynamics of the dominant mode, with a cross-correlation of 0.7. However, in extremely rare cases, very large events which we term as ‘giant rogue waves’ can be observed when all modes generate pulses at the same time, as shown at the center of the graph.

comb states and in the chaotic transition to stable low-noise breather combs. We have observed the comb line dependent breathing intensity and relative phase, a further study of which could elucidate the complex energy transfer mechanisms in frequency combs generated in cavities with mode interaction. In addition, we have mapped out for, the first time, the transition between different breathing frequency combs and measured the rapid loss of power followed by bursts of revival during the transition process. We have also measured the spectral correlation of intensity, with respect to a single mode designated as the primary, during the occurrence of rogue waves and observed intriguing non-linear phenomenon such as the occurrence of ‘giant rogue waves’ where the spectral correlation is significant higher than a ‘normal’ rogue wave. In all, we have observed and characterized a wide range of rich non-linear phenomenon which would aid in the deeper understanding of extreme events that arise in the Kerr microcavities, in addition to laying out a path for further study using the PASTA system.

CHAPTER 5

Dynamics of soliton crystal ensembles in microresonators

5.1 Introduction

A soliton is a localized wave packet that maintains its shape during propagation. Such self-reinforcing structures have been observed in different physical systems like condensed matter, atomic waves, fluid mechanics. Optical solitons are usually generated in optical resonators like semiconductor lasers, solid-state lasers, fiber resonators, and recently Kerr microresonators. Understanding the underlying spatio-temporal dynamics of optical solitons in different systems is essential to engineering required optical states. In microcavities soliton formation hinges on a double balance between gain and loss and nonlinear phase and dispersion. In the scenario under study in this paper, namely in the damped-driven NLSE, under the application of boundary conditions, the kinetics of solitons may be described by their velocity and instantaneous potential, analogous to particles in mechanics. The potential is largely governed by the background wave in the resonator. The background field is a wave complex affected by soliton tails, internal modulation and external forcing. Solitons can be trapped in local potential minima and may move with respect to the background when the potential is insufficient to trap them. The pining and unlocking of solitons has been realized recently in different resonator platforms. In addition to being pinned by the background, solitons may also lock into molecules, via interaction between soliton tails. Detailed spatio-temporal dynamics of these bound soliton molecules, such as molecular vibration and spacing jumps, have been predicted and recently observed.

A modulated background wave with a frequency of multiple FSR can provide a suitable periodic potential structure for the generation of soliton crystals in microresonators. Analogous to real crystals, soliton crystals may also possess Schottky and Frenkel defects. Soliton crystals have hitherto primarily been studied in slow time scale using spectral measurements via an OSA or temporal characterization as measured by intensity auto-correlation or cross-correlation. These methods are however unable to accurately capture dynamically evolving crystal states, such as breathing or quasi-chaotic soliton crystals. To record the dynamical temporal structure of these states in general, we might use methods such as large bandwidth oscilloscope, time lens and time-stretch dispersive Fourier transform (TS-DFT). In this paper we study crystal dynamics for the first time in a Kerr-microresonator platform. A self-interacting soliton ensemble such as a soliton crystal on a complex background could provide a suitable platform to study collective dynamics. The analog between optical solitons and real particles may form a bridge for the study of nonlinear dynamics in different physical systems. In this work, we show the dynamical breather and chaotic structure of soliton crystals in SiN microresonators. The periodic background is provided by the interference between pump and the enhanced frequency lines at mode-crossing points. The dynamical breather and chaotic structures are shown to be related to the collective dynamics of soliton ensembles. We generate above mentioned collective dynamics via deterministic approaches in different microresonators. The breathing frequency is linearly dependent on the pump detuning. Using a vector network analyzer, we also observe featured soliton (S), cavity (C), and breather (B) resonances. The spatial breather is topologically protected at high breathing frequency and turns chaotic at low frequency. We show that the breathing phase of two solitons near the defects can be controlled by engineering multiple mode-crossing points. The temporal structures of spatial breather and chaos are recorded by our promoted time-lens system. The stationary state is recovered by an auto-correlation measurement. Our simulations further confirm our experimental results and predict some interesting dynamics.

5.2 Generation of soliton crystal states

We generate various soliton crystals in Si3N4 Kerr microresonators with anomalous dispersion and free spectral ranges (FSRs) of about 64.6 GHz. Figure 5.1a depicts our experimental setup. A continuous wave (CW) laser and followed by an erbium-doped fiber amplifier (EDFA) provides the long-wavelength band (L band) pump. Two circulators are used to couple light in and out of the microresonators. The pump line is removed by a 7.5 nm bandstop filter (BSF), we then send the filtered optical spectrum to a PD and record the RF spectrum on an electronic spectrum analyzer (ESA). A vector network analyzer is used to study the cavity response with radiofrequency (RF) modulation applied on the pump light via an electro-optic phase modulator. The optical spectra spectrum, detected radiofrequency spectrum and cavity response are measured and recorded simultaneously with a forward sweeping (i.e., blue to red sweeping) laser, tuned via a piezo. The microscope image of the tested device is shown in Figure 5.1b. Pump power undergoes a 1 dB attenuation in the leading circulator and 3 dB coupling loss before being coupled into the bus waveguide.

The avoided mode crossings caused by the coupling between TE and TM modes introduce a spectrally local perturbation in the cavity dispersion, giving rise to strong frequency lines that interfere with CW background in the Kerr microresonator. The background wave is therefore modulated and forms a periodic sequence of potential wells for solitons in the cavity, enabling a crystal-like soliton ensemble. Figure 5.1c-f present the spatiotemporal evolution map of different soliton crystals with corresponding optical spectra and RF spectra plotted in Figure 5.1g-j and Figure 5.1k-n, respectively. All soliton crystals presented in Figure 5.1 are accessed with a EDFA output power of 27 dBm at 1593.1 nm and input power into bus waveguide of 23dBm. Figure 5.1c shows the evolution of the stationary soliton crystal two defects (2-defect SC) spaced by 15 solitons. The prominent comb lines in Figure 5.1f are spaced by 47 FSRs corresponding to a soliton separation of 1/47 roundtrip. The red arrow marks the dominant AMX resonance where a prominent comb line lies in that we can also directly observe from cavity transmission measurement. The flat RF spectra in Figure 5.1j shows good coherence of the 2-defect SC. Figure 5.1d-e shows the spatio-temporal dynamics of a 1-defect SC with spatial breathing (1-defect breather) and 2-defect breather. The propagating velocity of one soliton near the defect is slightly altered compared to the soliton crystal background, thereby causing it to be ‘unpinned’ from the background and drift with respect to the crystal ensemble. This drifting soliton occupies the vacant potential well and generate a new defect at it’s original position. This unpinning and subsequent occupation of the defects, by adjacent solitons repeat periodically, resulting in spatially breathing crystal and a periodic variation of intracavity power. The spatial breathing of solitons occurs due to a physically distinct mechanism when compared to traditionally observed soliton breathers where the pulse peak power and intensity vary periodically.

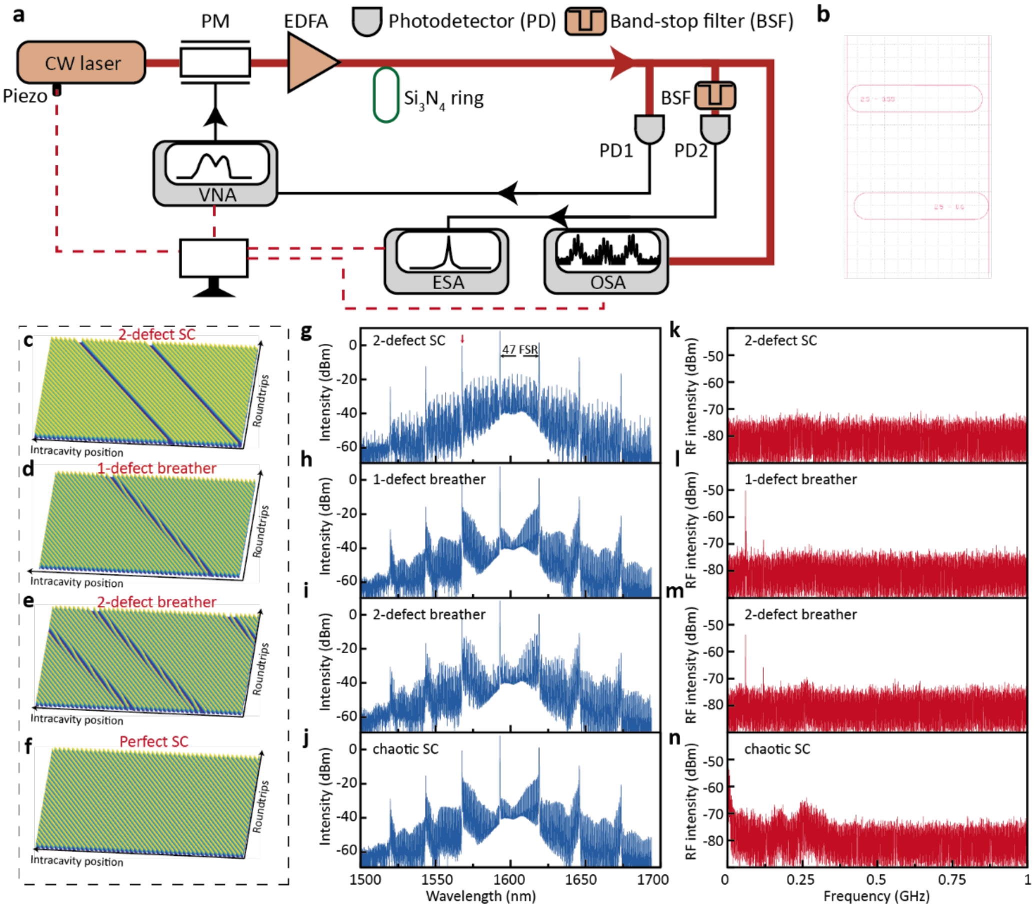

Figure 5.1. a, Experimental set-up for the generation of soliton crystals. A continuous-wave (CW) laser is used as the light source with the emitting wavelength tuned through the piezo. PM, phase modulator; EDFA, erbium-doped fiber amplifier; VNA, vector network analyzer; ESA, electronic spectrum analyzer; OSA, optical spectrum analyzer. b, image of microring resonator c-f, Schematic representations of 2-defect stationary SC (c), 1-defect SC with spatial breathing (d), 2-defect SC with spatial breathing (e), perfect soliton crystal (f) Presented 2-defect soliton crystals have 15 solitons between two defects. g-j, Experimental optical spectra of 2-defect stationary SC (g), 1-defect SC with spatial breathing (h), 2-defect SC with spatial breathing (i), perfect SC (j). The red arrow marks the currently dominant resonance that is 47 FSR away from the pump resonance. k-n, Experimental radiofrequency (RF) spectra of 2-defect stationary SC (k), 1-defect SC with spatial breathing (l), 2-defect SC with spatial breathing (m), perfect SC (n). 1-defect breather and 2-defect breather have the similar breathing frequency of about 60 MHz.

The mechanism is also distinct when compared to the vibration of soliton molecules, which occurs due to soliton interaction via their tails, since spatial breathing is a result of the many-body effect and the spatial motion is relative the soliton crystal background. The soliton behaves like a real particle rather than string or waveform. When defects and solitons move across each other, the waveform remains stable. The defect is analogous to a dark pulse in a soliton crystal, a kind of dark metasoliton. Here, the spectral envelop of the 1-defect breather and 2-defect breather are almost identical due to the similar breathing frequency of about 60 MHz. Interestingly, two defects can spatially move with a fixed phase difference. (Other defect numbers Supplementary material) Chaotic SCs have also been predicted and are observed experimentally for the first time. Figure 5.1f plots the chaotic pattern of the spatiotemporal dynamics in soliton crystals. The spatial breathing might be unstable during transition between the breather and stationary state, giving rising to chaotic soliton crystals that are identifiable from their RF spectra in Figure 5.1n.

5.3 Experimental comb state evolution pathways

We experimentally obtain several deterministic paths to access above-mentioned soliton crystals in several resonances (See supplementary material). Figure 5.1a shows the evolution of microcombs generated in our microresonator when forward sweeping the pump, at a pump power of 27 dBm. The soliton crystal generation has five qualitatively different regions: (a1) the spectral primary lines, i.e., temporal Turing pattern. (a2) the chaotic waveform leading to soliton crystals. (a3), 2-defect breather. (a4) 1-defect breather. (a5) the stationary 2-defect SC. The similar intracavity power of leading chaotic spectra and soliton crystals make it possible to access soliton crystals with slow forward sweeping and reversely transitions between leading chaotic waveform and soliton crystals. Another deterministic path is shown in Figure 5.1b, generated by forward sweeping the pump, at a pump power of 25.6 dBm. This path also includes five qualitatively different regions: (b1) primary lines. (b2) 1-defect breather. (b3) Perfect SC. (b4) 1-defect breather. (b5) 1-defect SC. An interesting point to note in this path is the transition between different soliton separations. The transition point is marked with a dashed white circle. This transition might be explained through following dynamics. The AMX in mode number -47 (from the pump) becomes dominant in determining the modulation of the background wave between state (b2) and (b4). Consequently,

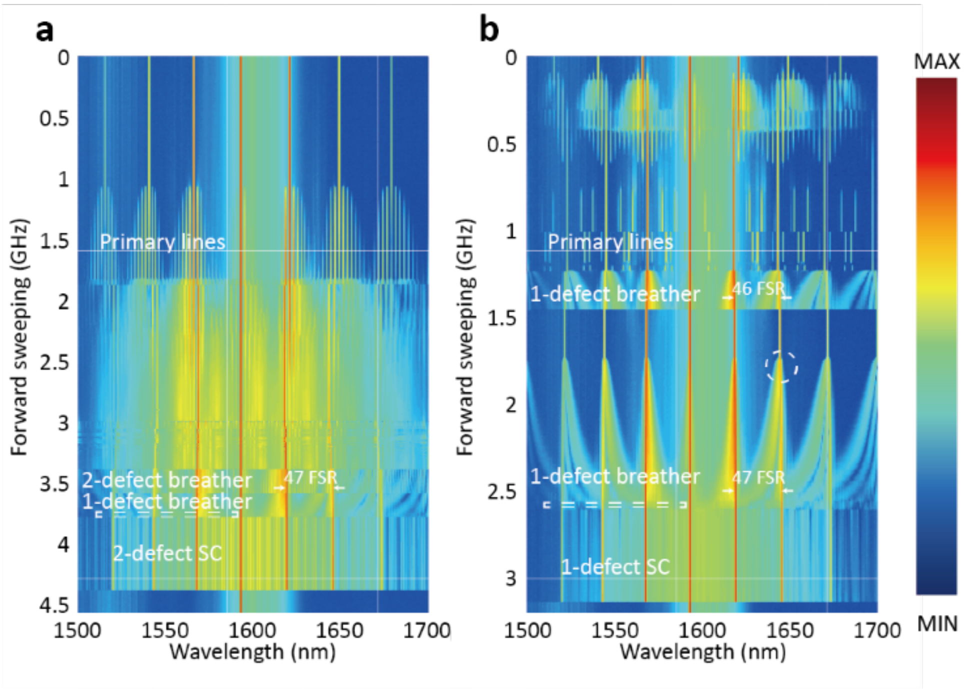

Figure 5.2. a-b, Experimental optical spectra of the generated microcombs from a 66 GHz Si_3N_4 microresonator using forward (blue-to-red) laser sweeping with 27 dBm (a) and 25.6 dBm (b) input powers, respectively. The white dashed rectangular marks the region where the chaotic soliton crystal may occur. The white dashed circle marks the region where the spacing between adjacent excess lines changes from 47 FSR to 46 FSR. a, the transition from primary lines to chaotic states then 2-defect breather, 1 defect breather and final stationary 2-defect SC. b, the transition from primary lines to 1-defect breather then perfect SC, another 1-defect breather with a different SC number and final stationary 1-defect SC.

the separation between two adjacent solitons in the perfect soliton crystal changes from 1/46 to 1/47 of the roundtrip and a defect is formed. The soliton separation is then 1/47 of the roundtrip. Similar to Figure 5.2a, the chaotic SC occurs when the breather evolving into a stationary SC. Different from the sudden jump between 1-defect breather and 2-defect SC and stochastically occurrence of chaotic SCs in Figure 5.2a, we experimentally observe continuous and reversable spectral evolution from 1-defect breather to chaotic SCs and final 1-defect SC. In Fig.3f, we further confirm that the spatial motions of solitons in the 1-defect breather actually slow down with forward wavelength tuning, and finally settle down to a stationary state in a gradual transition.

5.4 Characterization of soliton crystals

After studying the physical mechanism of the breather and chaotic crystals, we next characterize the dynamical properties of the cavity response and breathers. We obtain the cavity response to the phase modulation on the pump line using a VNA. Figure 5.3a plots the VNA magnitude in log scale of four different states corresponding to Figure 5.1. Similar to the stationary one soliton state and perfect soliton crystal, We observe two peaks in the VNA spectra of 2-defect SC, namely the cavity (C)-resonance and soliton (S)-resonance. C-resonance reflects the effective cavity resonance considering the frequency shift due to cross-phase modulation from background wave on the phase modulation sidebands. S-resonance reflects the effective soliton resonance which includes the frequency shift due to cross-phase modulation from solitons. The strength of S-resonance is dependent on the number of solitons within the cavity. Since we have 45 surviving solitons in a 2-defect SC, the corresponding S-resonance is much stronger than C-resonance. There exists a peak in both 2-defect breather and 1-defect breather induced by the dynamical breathing, named "breathing (B)-peak". The B-peak in the 2-defect SC is located at almost the same frequency as the 1-defect SC due to the similar breathing frequency. We expect the magnitude of the B-peak to be correlated with the number of spatial breather solitons at each instant (which in this study directly corresponds to the number of defects), and this is indeed observed in the experiment with the 2-defect SC having a higher B-peak. Figure 5.3b-c shows the evolution map of the VNA magnitude in linear scale with forward wavelength sweeping, corresponding to the region (a3) and region (a4) in Figure 5.2a.

The evolution map exhibits several clear B-peaks in both 2-defect breather and 1-defect breather, outlined by white lines in Figure 5.3b-c. The B-peaks red-shift with a forward pump sweeping and gradually decrease near transition points marked by black lines. Correspondingly, we observe a linear decrease in breathing frequency while forward tuning the pump wavelength and this trend agrees with VNA results Figure 5.3b-c. In addition, the intensity of breathing also linearly increases with forward tuning of the pump wavelength. The 1-defect breather has a steeper slope compared to 2-defect breather in relation to the evolution of both intensity and breathing frequency with forward pump tuning. Figure 5.3f plots the evolution of breathing frequency corresponding

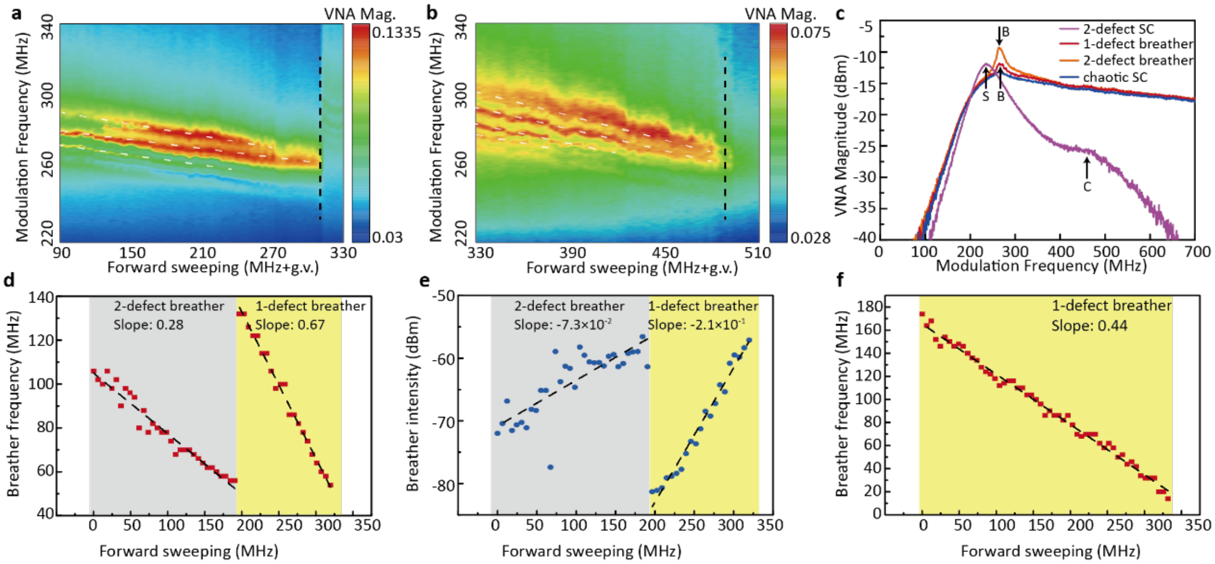

Figure 5.3. a-b, The evolution map of vector network analyzer (VNA) magnitude as a function of swept frequency and modulation frequency showing the modulation response (linear scale). a, 2-defect breather; b, 1-defect breather. The white dashed lines outline the traces of main peaks of VNA response. The white dashed rectangular marks the chaotic SC region where the peaks of VNA response quickly drop. c, The modulation response in different SC states. "B" represents the peak induced by the spatial breathing. "S" and "C" represents S-resonance and C-resonance, respectively. d-e, The experimental evolution of breathing frequency of the SC power filtering pump with the SC states changing from 2-defect breather (grey) to 1-defect breather (yellow). Red blocks represent the recorded breathing frequencies. Two black dashed lines are the linear fits of breathing frequencies at two different SC states. e, The experimental evolution of breathing intensity corresponding to d. Blue dots represent the recorded breathing intensities. Two black dashed lines are the linear fits of breathing intensities at two different SC states. f, The experimental evolution of breathing frequency of the 1-defect breather (yellow) power filtering pump.

to the region (b4) in Figure 5.2b. The breathing frequency can be tuned within a strikingly broad range, from 175 MHz to 10MHz. Such a broad tuning range has been observed for the first time in microresonator breather soliton states and is attributed to the unique breathing mechanism. Breathing frequencies under 10MHz are difficult to access because the state shifts to that of a chaotic SC at this point.

5.5 Ultrafast temporal observation of dynamical soliton crystals with defects

In prior sections, we have explored the deterministic generation, dynamical properties and physical mechanism of different soliton crystals. In this section, we further look into the temporal behavior of soliton crystals in three aspects: slow-time evolution recorded directly by the oscilloscope (OSC) with 22 GHz bandwidth, the fast-time evolution observed in an ultrafast temporal imaging system (details in supplementary) and spatial structure recovered through auto-correlation measurements.

Fig.4a shows the experimental set-up used for the observation of soliton crystals with spatial breathing. A soliton sequence with an angular breathing frequency of ω_B is generated from DUT and recorded in slow-time and fast-time scale separately. Figure 5.4b shows the schematic detailing the acquisition of the the full dynamics within one-round trip of a periodic signal with a high repetition rate f_B using a temporal imaging system with a low frame rate f_F. Here, the blue circle represents the repetition of frames in the temporal imaging system while the red circle represents the repetition of the periodic signal. The residual phase difference between the periodic signal and the frame after $\tau_F = 1/f_F$ is given by $\phi_{res} = 2\pi \left\lfloor f_B/f_F \right\rfloor)$ where mod is the remainder function. The frame length τ_L can also be expressed as a phase span of $\phi_L = 2\pi f_B \tau_L$ Considering ϕ_{res} in the range of $(0, \pi)$, the dynamics of the signal within one period is down sampled when $\phi_{res} > \phi_L$ and over sampled when $\phi_{res} < \phi_L$. Our temporal imaging system primarily consists of a FWM-based time lens and a buffer and to increase the record length of a single frame. The generated breathing soliton crystal first goes through BPF2 to match the bandwidth of FWM. The simulated waveform of 2-defect SC in one roundtrip after BPF2 is plotted in Figure 5.4c. The crystal-like structure of the soliton ensemble is masked due to the limited spectral bandwidth. However the spectral bandwidth is sufficient to resolve the dips corresponding to the soliton crystal defects. The filtered signal goes through AM1 locked to MLL, with a repetition rate of 2 MHz and a gate time of 5 ns. However, the maximum recording length for one shot is limited to around 500 ps. We use the optical buffer to effectively extend the recording length in one frame to 2 ns by generating

10 replicas and stitching their images with a fixed temporal shift. The additional 9 replicas are generated in the optical buffer. The frame rate of our temporal imaging system is therefore 2 MHz and the frame length is 2ns. Figure 5.4d shows the experimental 2D evolution map of 2-defect breather recorded by the above mentioned temporal imaging system. The breathing frequency of this state is about 56 MHz that corresponds to a temporal period of 18 ns. We therefore can use 9 frames or more to fully recover the breathing dynamics. We note that the solitons near the two defects move in different phases. The breathing frequency is quite stable, hence induce a nearly periodic pattern. In contrast, the breathing frequency of the 2-defect breather drifts obviously and the ϕ_{res} varies away from either 0 or 2π.

Figure 5.4f plots the temporal trace of comb power after BPF1 and EDFA. The prominent comb lines are filtered by BPF1 to increase the peak-to-peak contrast. We use PD3 with 1 GHz bandwidth to detect the slow-time signal and smooth dynamics beyond detection limits. The signal shape is not perfect sine function, which corresponds to the harmonic peak in RF spectra in Figure 5.4g. The noise may come from intracavity fluctuation and amplified spontaneous noise in EDFA. The finite span of the breathing frequency reflects the drift of the breathing frequency that qualitatively agrees with the evolution map in Figure 5.4e.

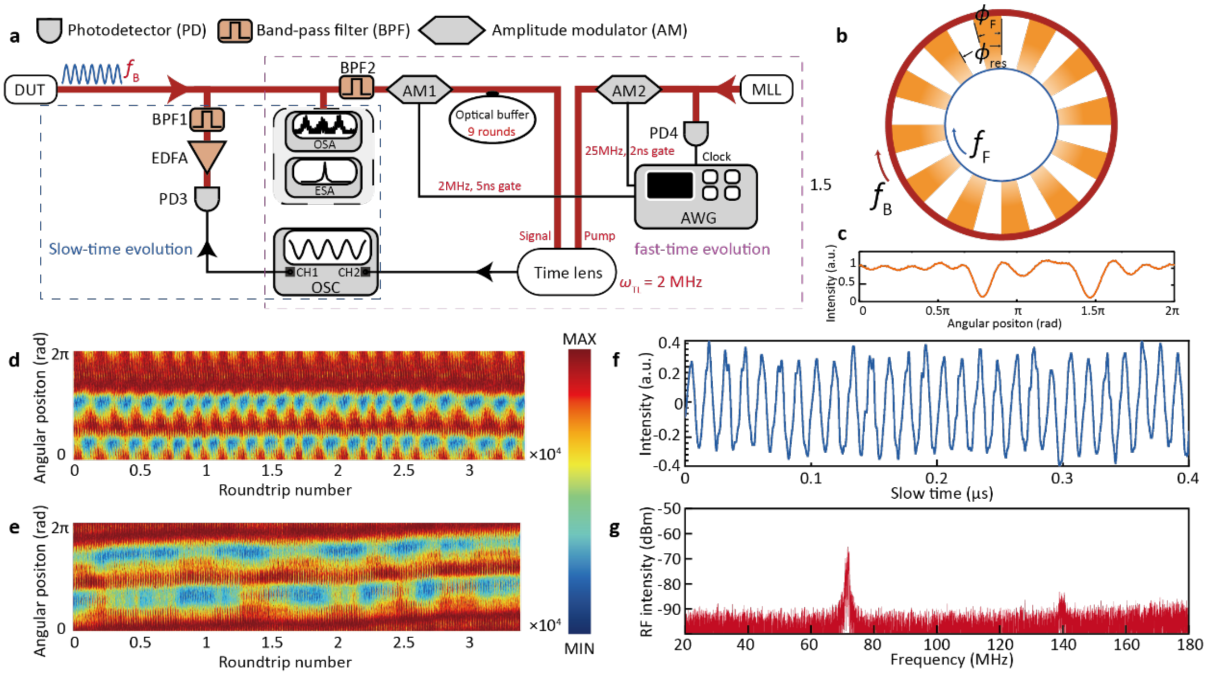

Figure 5.4. a, Schematic representation of the experimental set-up for the observation of the slow-time evolution (blue dashed rectangular) using oscilloscope directly and fast-time evolution using a improve time-lens imaging system (purple dashed rectangular). Measurements with two different time scales are recorded separately. The generated SC microcombs with a breathing angular frequency ω_B. BPF1 and BPF2 have the same bandwidth. Optical buffer effectively extends the one-shot length of time-lens system to 2 ns. EDFA, erbium-doped fiber amplifier; ESA, electronic spectrum analyzer; OSA, optical spectrum analyzer; OSC, oscilloscope; MLL, mode-locked fiber laser AWG, arbitrary waveform generator. b, the schematic representation of the operation principle of the phase-difference sampling method. The blue circle represents the time lens system and the angle of each orange region represents one-shot angular length ϕ_g. The red circle represents the SC breather. ϕ_{res} is the residual phase between the SC breather and time-lens system after 500ns. c, The simulated intensity with one roundtrip of the SC after BPF2 as a function of the angular position. d, The fast-time evolution of a stable breather recorded by the time-lens system. e, The fast-time evolution of a unstable breather recorded by the time-lens system. f, The slow-time evolution of a breather. g, The RF spectra corresponding to f.

CHAPTER 6

Persistence and statistics of Rogue events in microresonators

6.1 Introduction

Rogue waves are extreme events first theorized and observed in hydrodynamic systems [125] but later discovered to arise in solutions to a large class of nonlinear dynamic equations describing a range of physical processes. Optical rogue waves, generated by the nonlinear Schrodinger equation (NLSE) [107], are of particular interest as they can be easily generated, can be well characterized via advanced optical measurement techniques [107, 126] and as they share remarkable similarities with their hydrodynamic counterparts [99, 107]. Most prior research on optical rogue waves has hitherto focused on wave propagation in fiber and there is a conspicuous lack of sufficient experimental evidence of rogue waves in other optical systems governed by the NLSE. Here we study rogue events in microresonators which are distinct from their fiber counterparts, due to their short cavity round-trip time which enables persistence of the intracavity field over multiple round trips. In addition, microcavities also allow for an in-depth study of field evolution on the length scale of the pumped cavity, which by its nature is much shorter than a fiber cavity. However, state-of-the-art temporal imaging techniques cannot easily achieve high temporal resolution along with a long temporal recording length simultaneously, which hinders comprehensive understanding of these intriguing ultrafast optical phenomena that evolve over a timescale much longer than their fine temporal details.We therefore utilize a novel panoramic-reconstruction temporal imaging (PARTI) system [97] which consists of a high-fidelity optical buffer, a low-aberration time magnifier and synchronization-control electronics.The system allows for magnification of different parts of the input optical waveform sequentially, and the results are the stitched together during processing to allow for a long recording length. Our system achieves a temporal resolution of 1 ps, with a recording length of over 2 ns, allowing for a net time-bandwidth product of over 2000. This allows us to capture the full evolution of rogue events over several tens of cavity round-trips.

6.2 Rogue events and real-time analysis

Field evolution in Kerr microresonators is accurately described by the damped-driven NLSE under cvaity boundary conditions, under the good cavity limit, of high finesse, low pump power and slow cavity field evolution, the Lugiato-Lefever equation (LLE) functions as a highly accurate approximation. Fig. 6.1a plots the typical simulated transition dynamics for anomalous GVD mocroresonators as one detunes the laser frequency into the cavity resonance from the blue (high frequency) side. First we observe the occurrence of modulation instability and the formation of Turing rolls, in the frequency domain the state corresponds to a few equally spaced primary comblines several FSR apart. Then as the laser frequency is detuned further into the cavity resonance, secondary comb lines start to grow until the Turing pattern is spontaneously destabilized and the comb exhibits chaotic oscillations. It is this region of spatio-temporal chaos, and specifically the occurrence of extreme events herein, that is primarily the subject of study in this chapter. In the frequency domain, it corresponds to a broadband Kerr frequency comb with specific spectral features highly-dependent on the location of avoided mode crossings. Subsequently as the pump laser is further tuned into the cavity, till we are on the effectively red-detuned side of the resonance, we observe the collapse of chaotic oscillations into one or more dissipative solitons. Fig. 6.1b offers a closer look at the region of chaotic oscillations, the top panel plots the field evolution at each position in the cavity as the comb field evolves across 4000 roundtrips. Note the complex field structure with multiple pulse formation, collision and breather revival events. We identify extreme events via the strict crest heights criterion. The crest height of a pulse is defined as the amplitude of the maxima above the steady state intensity, and the criterion defines events with heights at least 8 standard deviations above the mean crest height as a rogue event. In the top panel of Fig. 6.1b we mark the extreme event in a red box, and zoom into the event on the bottom panel. The first point to note here is that the rogue event persists in the cavity for multiple round trips, i. e. for every intracavity rogue event there are multiple pulses at the output waveguide with crest height

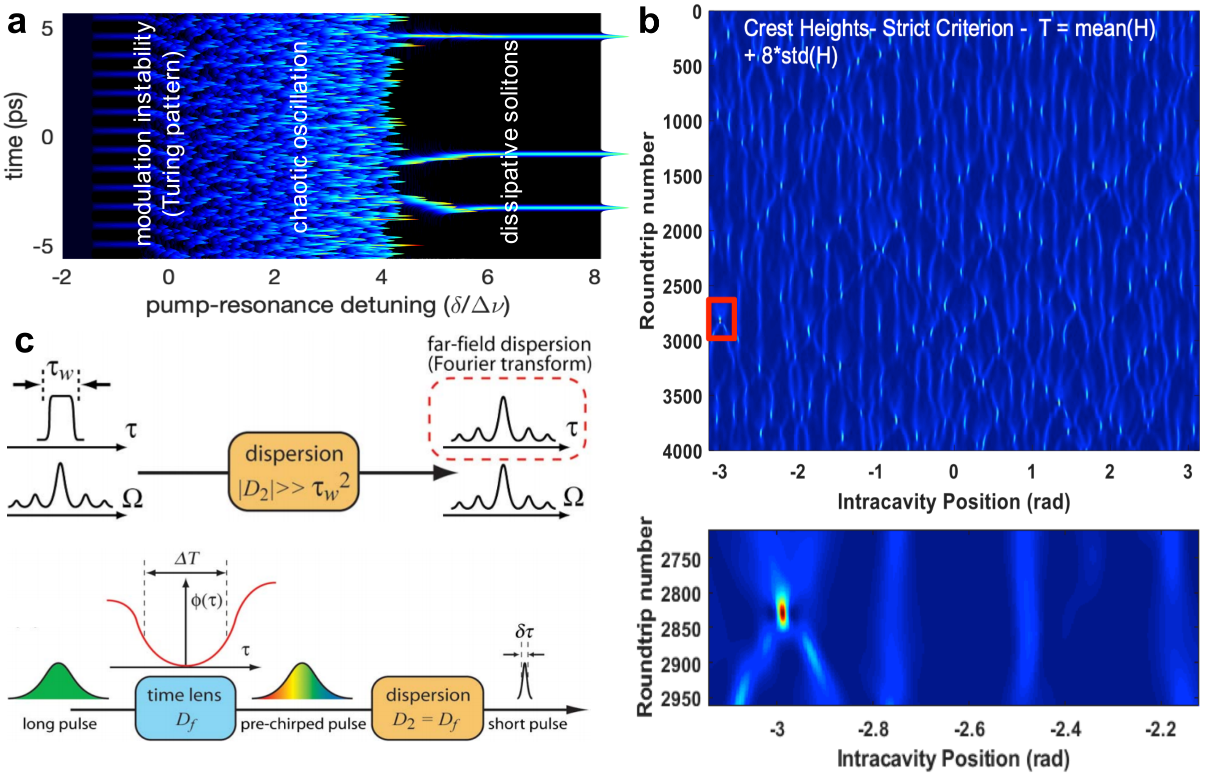

Figure 6.1. a, Simulated field evolution in a 90 GHz Si_3N_4 microresonator with anomalous GVD using forward (blue-to-red) laser sweeping showing the dynamical evolution of the field from Turing patterns to chaotic oscillations and finally dissipative Kerr solitons. b, Top panel: depiction of the intracavity field in the chaotic regime over 4000 round trips with a rogue event detection marked with red box. Bottom panel : zoom in of the rogue event showing rogue event persistence over multiple round trips. c, Depiction of the concept of spatio-temporal duality, with the equilence between paraxial diffraction and narrow band dispersion and quadratic phase modulation acting as an analogue to a spatial lens

above the rogue wave threshold. We note that microresonators are an ideal platform to study rogue wave persistence since field evolution is almost always occurs on timescales significantly longer than cavity roundtrip time.

Experimentally recording rogue wave formation and the detailed intracavity field necessitates the use of real-time field imaging techniques. Time lens techniques have previously been used in fiber systems to unveil the fascinating ultrafast phenomena in optics, such as the onset of mode-locking, soliton explosions, and optical rogue waves. The principle of the temporal imaging is based in space-time duality which establishes the two mathematical equivalences necessary for it's operation. The first is the equivalence between paraxial diffraction and narrowband dispersion, which shows how propagation of a waveform in a dispersive element in time is equivalent to propagation in free-space, this is shown in Fig. 6.1c on the top panel. Secondly there is the equivalence between the spatial quadriatic phase modulation of a waveform while passing through a lens in space and temporal quadriatic phase modulation as shown in Fig. 6.1c on the bottom panel.

6.3 Panoramic reconstruction temporal imaging (PARTI)

On the basis of space–time duality, quadratic phase modulation (time lens) and dispersion can be properly combined to significantly enhance the temporal resolution and a record value of 220 fs [127] has been demonstrated. On the other hand, just like there is always a limitation on the field-of-view in any spatial imaging systems, the single-shot recording length of temporal imaging systems has been hitherto limited to ¡ 300 ps [128]. Owing to this limitation, the time-bandwidth product (TBWP, the ratio between the recording length and the temporal resolution) of the state-of-the-art temporal imaging systems has not exceeded 450 [127]. Such a situation hinders the applications of temporal imaging systems to study many important optical nonlinear dynamics, where not only fine temporal details but also long evolution information are necessary for a comprehensive understanding of the phenomena, such as rogue wave persistence. To capture comprehensive portraits of these processes, as well as many other transient phenomena in nonlinear optical dynamics [99, 129, 130], a temporal imaging system with a TBWP much greater than 1000 is necessary.

To address this limitation, we used a panoramic-reconstruction temporal imaging (PARTI) system [97], in analogy with the wisdom of stitching multiple mosaic images to achieve larger-field-of-view. The PARTI system consists of a high-fidelity optical buffer, a low-aberration time magnifier and synchronization- control electronics and the schematic is depicted in Fig. 6.2. The Kerr soliton is modulated to only select the time period to be magnified, in practice this is a 3 ns slice of the waveform selected every 2 MHz and this slice forms the input singnal under test (SUT). Since the SUT is transient and non-repetitive, the concept of sample scanning in the spatial domain cannot be conveniently adopted in temporal imaging systems. To address this problem, a fibre-loop-based optical buffer is integrated with a time magnifier to realize temporal scanning using stroboscopic signal acquisition, a technique commonly adopted in sampling oscilloscopes. The optical buffer creates multiple identical replicas of SUT with a constant time interval, which will be subsequently measured by the following time magnifier, thus realizing the temporal scanning on a transient SUT. Using the optical buffer, SUT replicas can be generated with a pre-defined period of T_1. If the measurement period of time magnifier is T_2, then in each frame, the time magnifier captures a different section of the long waveform with a step size equal to $|T_1 - T_2|$ [97]. Furthermore, by matching the step size to the recording length of the time magnifier, seamless measurement of a long waveform can be realized. The output of the PARTI system represents the magnified waveform corresponding to different sections of the long SUT and is recorded by a high-speed real-time oscilloscope. After data processing, neighboring frames of magnified waveform will be stitched together to reconstruct a magnified panoramic image of the original SUT. Therefore, the effective single-shot recording length is scaled by the number of replicas without sacrificing the temporal resolution, thus substantially enhancing the TBWP to over 2000.

The signals from the buffer are then time-magnified via a time lens, The quadratic phase modulation or linear frequency chirp for temporal magnification may be achieved in different ways, but here we use four wave mixing (FWM). In Fig. 6.2 we see that the time lens consists of a pre-chirped MLL along with a highly nonlinear fiber (HNLF) to write a linear frequency chirp onto the signal. DCF2 which chirps the MLL, encodes the focal 'length' of the time lens. DCF1 placed at the output of the buffer acts as the 'object distance', while DCF3 acts as the 'image distance'. If the group delay dispersions are adequately matched, we can retrieve a temporally magnified version of the SUT with the magnification defined by the ration of the group delay dispersions of DCF3 and DCF2. All the electronics are synchronized with a common clock and the RF phases must be well adjusted so the SUT and MLL overlap in the HNLF. The final output is then detected by a high speed PD and recorded on a real time oscilloscope. Our system achieves an overall temporal magnification of 76, with a net temporal record length of over 2 ns in each frame (subtracting the overlap) and a resolution of 1 ps.

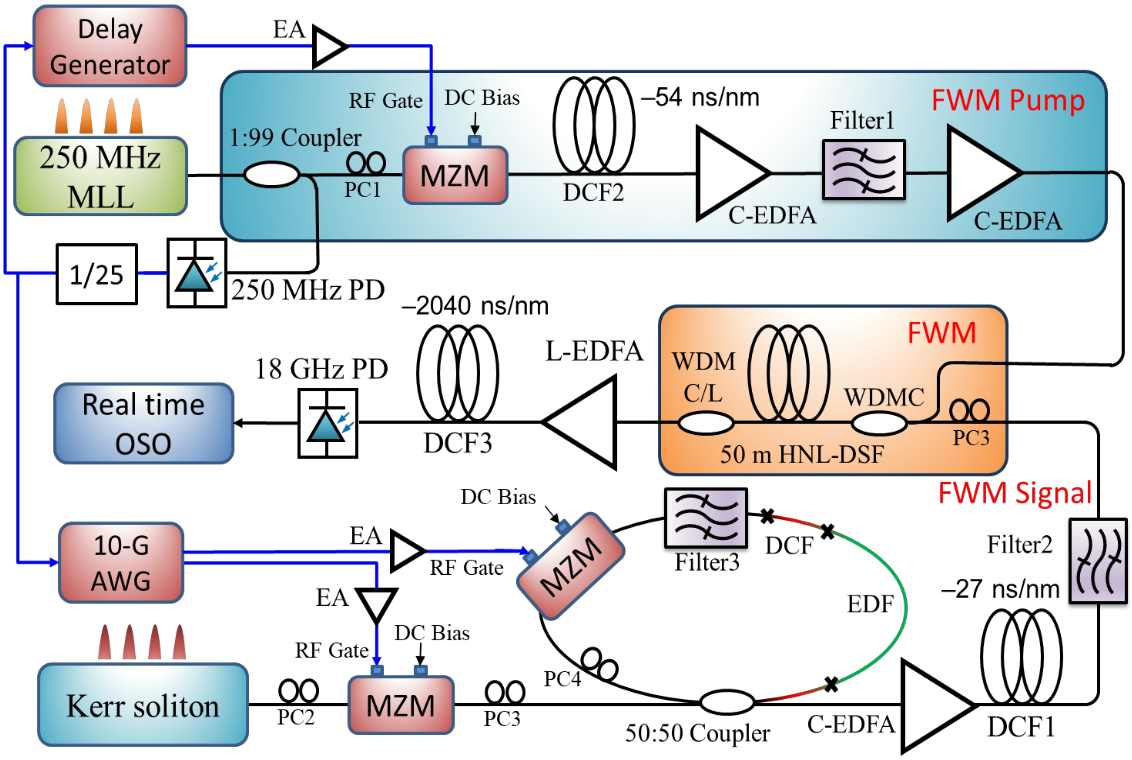

Figure 6.2. Schematic for the PARTI system with synchronization electronics, the system consists of a low aberration time lens along with a high fidelity optical buffer. The buffer stores the SUT and generates 10 replicas, of which a different slice is magnified in each replica. The final magnified frames are then stitched together to form an overall image with TBWP ¿ 2000. The time magnifier consists of a pre-chirped swept pump, a HNLF to write a quadratic phase chirp and input and output dispersions to form the magnified waveform

6.4 Chaotic combs

Fig. 6.3a shows the data acquisition setup. We generate the comb using an external cavity diode laser (ECDL), whose output is amplified by an erbium doped fiber amplifier (EDFA) to pump an Si_3N_4 microresonator. We pump 3 different microresonators with FSRs of 18, 66 and 90 GHz. We tune the pump laser across the cavity from the blue to red side. at each step of the detuning we directly send part of the comb spectrum to the electrical spectrum analyzer (ESA), optical spectrum analyzer (OSA) and record the RF and optical spectra. The remainder of the spectrum is sent to the PARTI setup to directly record the intracavity field and is also directly recorded onto the real-time oscilloscope. In Fig. 6.3b we plot different recorded comb optical spectra and their corresponding RF spectrum. The comb spectrum plotted in purple has an FSR of 90 GHz, The optical spectrum is that of a full broadband comb, but notice the presence of spectral irregularities with some lines exhibiting significant differences in power in comparison to the comb envelope. These mode interaction points may change the intracavity field evolution and hence the occurrence of rogue events. Note the broadband RF noise indicative of chaotic oscillations. The comb spectrum plotted in blue is retreived from the 66 GHz microcavity. We notice the presence of high intensity comb lines away from the pump, this is due to the effect of a strong avoided mode crossing in the cavity. This also significantly affects the RF spectrum, where we see a sharp drop-off of noise combined with localized noise at higher frequencies. At the bottom panel, plotted in red we plot an 19 GHz comb spectrum. The avoided mode crossings, while present, are weaker and do not alter the optical spectrum as significantly. The RF spectrum shows the presence of broadband noise.

Fig. 6.3c shows an example trace of the data recorded by PARTI in the panel on the left. The red box zooms in to a single frame, plotted in the panel on the right, where we see 10 individual windows recorded, which correspond to 10 consecutive positions on the buffered signal-under-test (SUT). The system is configured so that signal magnified in each window has some overlap with adjacent windows, allowing us to stitch the 10 windows to acquire a long time trace of the temporally magnified signal. The recoeded windows are not flat due to the non-flat temporal shape of the swept pump, as well as the slight differences in phase-matching condition of the FWM at

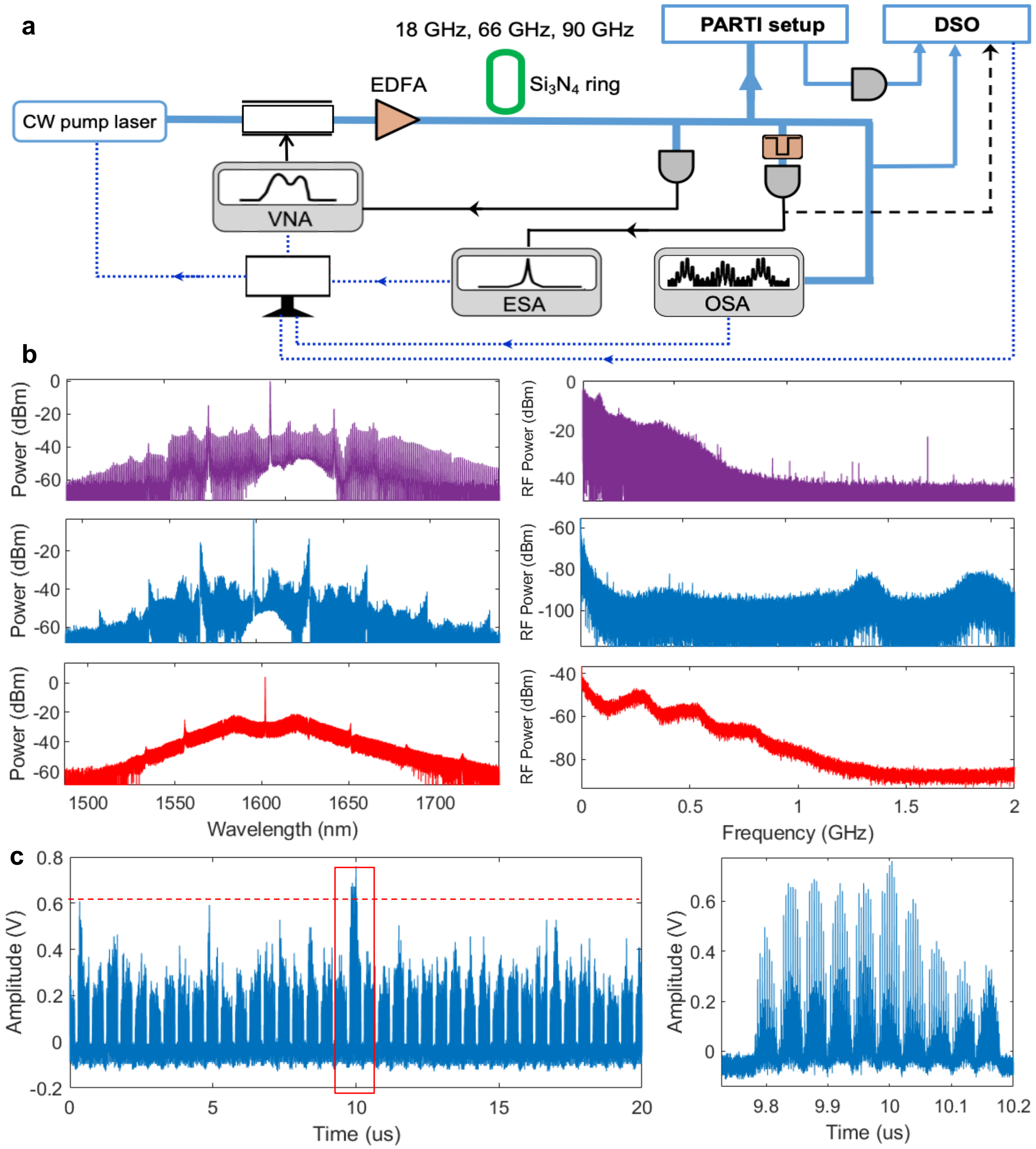

Figure 6.3. a, Schematic for simultaneous data aquisition. b, recorded optical and RF spectra of chaotic combs generated in a 90 GHz, 66 GHz and 19 GHz resonator, plotted in the top, middle and bottom panels respectively. c, example trace of the PARTI system, left panel zooms into the red box. Dashed red line indicates rogue event threshold.

different pumping wavelength. To correct this we calibrate the intensiry according to the time lens responsivity, and normalize with respect to the envelope. The sharp intensity spike at the centre of the trace is the rogue event. The threshold for rogue waves, calculated via a strict crest heights criterion (mean(H) + 8*stddev(H), where H is the distribution of all recorded wave heights from crest to noise floor), is plotted as a dashed red line in Fig. 6.3c.

6.5 Rogue wave persistence

Fig. 6.4 plot the frames with rogue waves captured by the PARTI system for different cavity FSRs. The 2D field evolution portraits are constructed by separating each round trip detected by PARTI, and stacking them together. The panel at the top corresponds to a rogue event detected in the 19 GHz cavity. We capture about 40 round trips of field evolution. We note that the rogue wave persists above the threshold (calculated via the strict crest heights criterion) for 9 cavity round trips. The resolution of the field portrait is ≈ 1 ps. The middle panel captures rogue waves in the 66 GHZ cavity, with persistence of 12 round trips. An interesting note here is that while the evolution of the overall field intensity is slow, corresponding to the significant low frequency noise recorded in the RF spectrum, the persistence of extreme events is still on a shorter time scale, corresponding to the localized regions of high frequency noise. The panel at the bottom records the persistence of an extreme events in the 90 GHz cavity. The rogue wave in this frame persists for 22 cavity round trips.

In Fig. 6.5a, we plot the simulation results for RW occurrence, notice the characteristic exponential fall off at high event intensities, characteristic of a long tailed distribution. Filtering out only the estreme events classified as rogue waves via the strict crest heights criterion, we plot the corresponding, simulated rogue wave persistence in the cavity against normalized rogue wave intensity in Fig. 6.5b. We see that as expected the rogue event intensity is directly correlated to persistence time, however there is still significant variability. and rogue wave intensity vs round trip persistence at the bottom. Fig. 6.5c plots the number of rogue events experimentally detected vs the cavity persistence time in the 19 GHz microresonator. We see that this also follows an L-

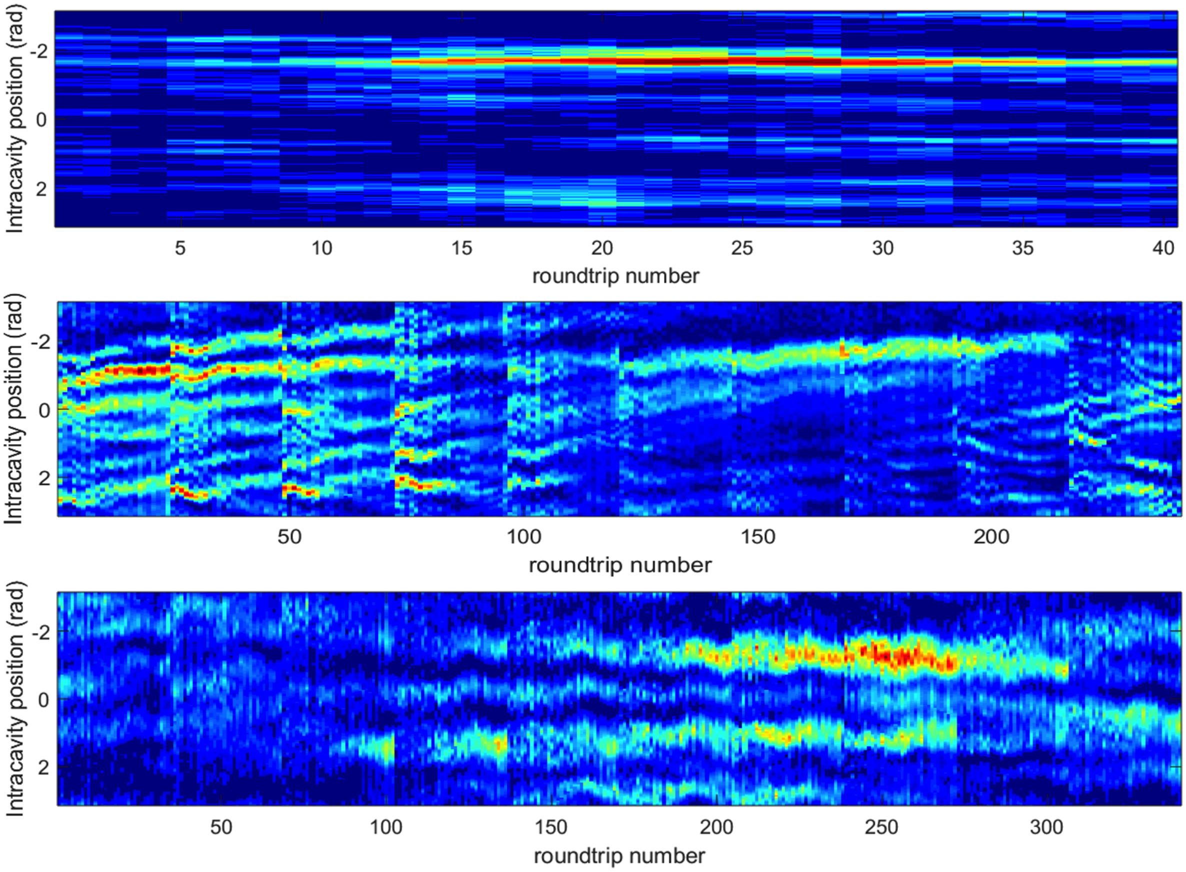

Figure 6.4. Rogue waves recorded in a 18 GHz (top panel), 66 GHz (middle panel) and 90 GHz (bottom panel) cavity. We clearly note the rogue wave evolution and persistence across multiple round trips and the

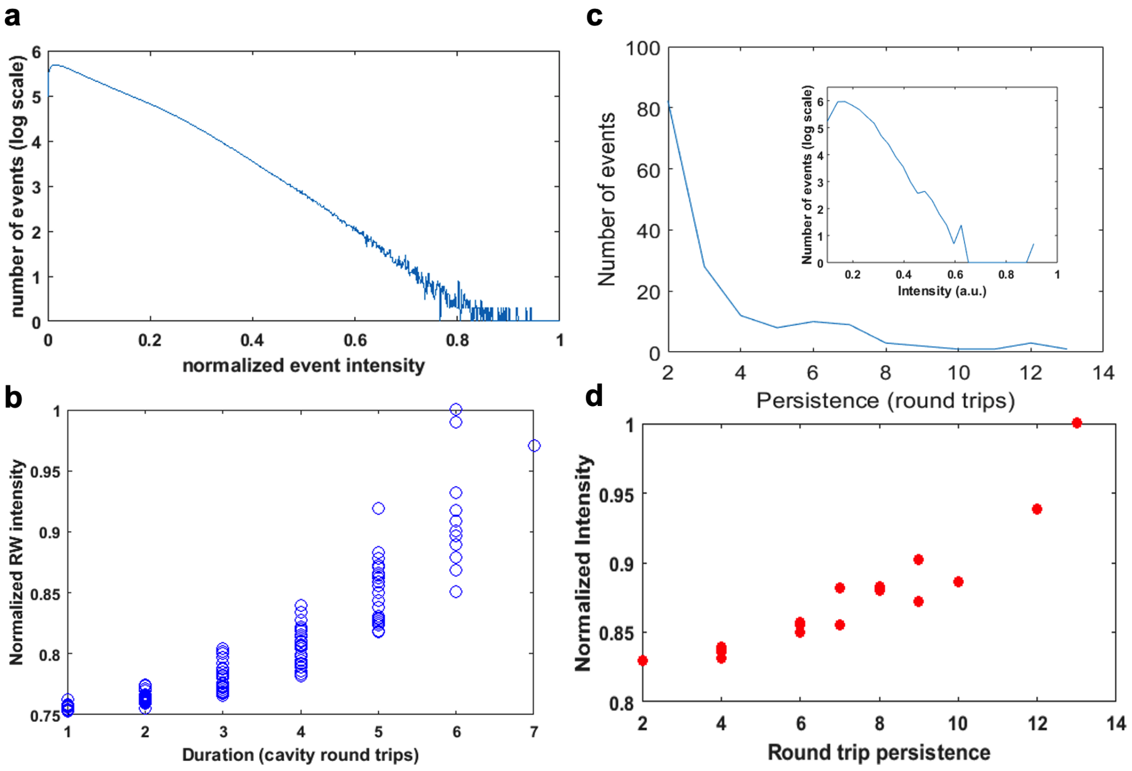

Figure 6.5. a, Simulation results for event intensity vs occurrence in a 19 GHz cavity, at a pump power of 2 W and Q of 1 million, which match the experiment). b, Simulated, normalized rogue wave intensity vs duration of persistence in a 19 GHz cavity. c, Experimental data for rogue wave occurrence in a 19 GHz cavity, plotted against duration of persistence, inset: plots the event magnitude in the intracavity field retrieved via the PASTA system vs event intensity, the peak in the distribution close to 0.9 is due to preselection of extreme events during data acquisition d, Plot of experimentally retrieved normalized rogue event intensity vs round trip persistence in a 19 GHz cavity.

shaped distribution with most rogue events only persisting for a short time, while very few persist over long durations. The inset shows the experimental distribution of crest heights in the retrieved intracavity field of the 19 GHz resonator from the PARTI setup. This also shows the characteristic long tailed distribution, matching well with Fig. 6.5a. A point to note here is that the peak in event occurrence close to 0.9 is due to bias in the operation of our system. We preselect for rogue events by triggering data acquisition on the oscilloscope only in the presence of high intensity events. The estimated skew of the rogue wave threshold due to this pre-selection is still less than 0.1%. We also plot the experimentally recorded normalized rogue wave intensity vs the round trip persistence in Fig. 6.5d, clearly showing that the parmeters are directly correlated, while still exhibiting statistical variation.

6.6 Summary

In summary we have used a novel panoramic-reconstruction temporal imaging (PARTI) system to study the evolution of the intracavity field in the chaotic regime. Specifically, we study rogue events in microresonators, which allow for an in-depth study of field evolution on the length scale of the pumped cavity, which by its nature is much shorter than a fiber cavity.. Our system achieves a high temporal resolution along with a long temporal recording length simultaneously, which allows for a comprehensive understanding of these intriguing ultrafast optical phenomena that evolve over a timescale much longer than their fine temporal details. We record rogue event persistence in 19, 66, and 90 GHz microresonators and study the distribution of RW persistence in the cavity and correlate it to RW intensity.

APPENDIX A

Comb state and locking characterization

A.1 Other comb states

The comb state is generated with a New Focus Velocity TLB-6730 as the pump laser. The pump frequency is tuned with a 2 MHz step via fine piezo control. The general multiple mode-spaced (MMS) scheme of comb formation involves the generation of several subcomb families with incommensurate spacing between them [13,131]. This is illustrated in Fig. A.2a, as we might expect, combs evolving via this scheme would, in general, produce several low frequency RF beats. The comb state we stabilize however, is one with a single offset beat and has just one other subcomb family aside from the sub-comb around the primary comb line as illustrated in Fig. A.2b. This state is not a necessary part of the comb evolution process and is only observed under the right conditions of power and detuning. Here we briefly describe several other states that we observe in our microresonator. One of the comb states we have observed, generates an equally spaced set of beats spanning around 600 MHz. This 'RF comb' is shown in Fig. A.3a, in this particular case an interesting point to note is that although multiple subcomb families exist in this state, the RF beats being equally spaced indicates a relationship between the different subcomb families. As detuning is changed this state changes to one with higher noise that does not show a regular equally spaced comb structure in the RF domain, as shown in Fig. A.3b. This state then eventually evolves into one with continuous low frequency noise, the RF spectrum at the repetition rate of such a comb is shown in Fig. A.3c. In addition, we observe states similar to the one we use for stabilization, having a strong low frequency RF beat in addition to the beat due to f_{rep}, as shown in Fig. A.3d, but exhibiting slightly different behavior with regards to degree of correlation between pump and the offset beat.

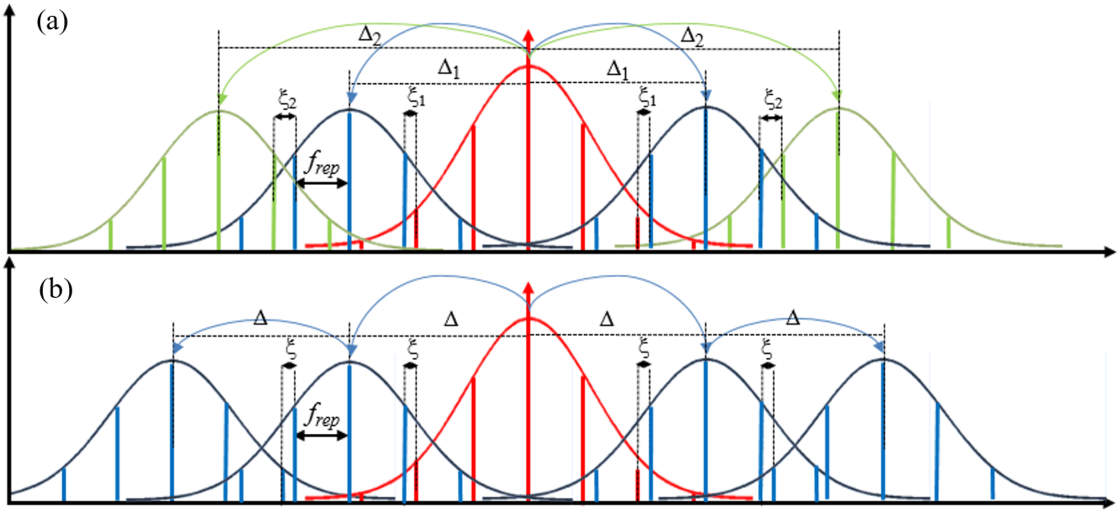

Figure A.2. **(a)** The general MMS scheme of comb formation, the two sets of subcombs, shown in blue and green belong to different families because the two sets of primary comb lines around which the subcombs form, are generated independently by the pump. The first set of primary comb lines are formed at an offset of Δ_1 from the pump and the second set are formed at an offset of Δ_2 from the pump, since Δ_2 is not a multiple of Δ_1 and neither Δ_2 nor Δ_1 need be integral multiples of the f_{rep}, there are two offset beats generated by beating of subcombs with each other, these offset beats are shown in the schematic as ξ_1 and ξ_2. Now if this idea is extended to multiple subcomb families we would expect the generation of multiple RF beatnotes, (and if the subcombs were broad enough we would also generate harmonics of the beatnotes) and this is what we experimentally observe. b, A special case of MMS comb formation that results in the generation of a single RF beat note (aside from the beat due to f_{rep}) that corresponds to the offset ξ between subcombs. Note that, in this case, only the first set of primary comb lines is formed due to modulation instability via the pump, all other primary comb lines are generated via cascaded four-wave mixing between the pump and the first set of primary comb lines, this mechanism allows for a single offset ξ, throughout the comb. We choose to stabilize this particular state due to the strong correlation between the pump frequency and ξ due to the dependence of ξ on Δ, as described in the main text.

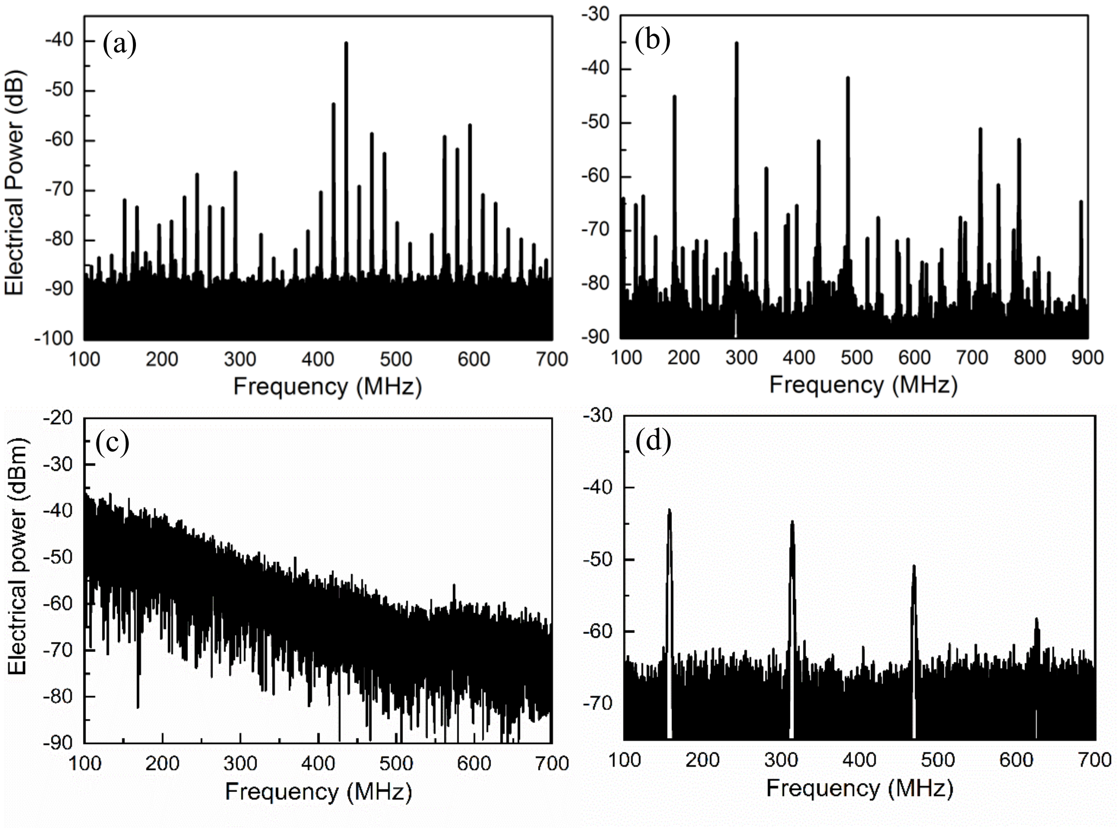

Figure A.3. **(a)** Multiple RF beats spanning 600 MHz with a spacing of 16 MHz generated by a comb state. The beats being equally spaced indicates that there is correlation between the offsets of different subcomb families. b, Multiple RF beats spanning over a GHz, generated by a comb state. Lack of defined structure to the beats suggests a general MMS scheme for the evolution of the state c, RF spectrum showing continuous low frequency noise, this state is obtained from the state in b. by changing the detuning such that the number of RF beats keeps increasing till we eventually have a ‘noise pedestal’ of continuous noise. d, RF spectrum showing a strong offset beat (breather tone) along with multiple harmonics. This state is similar to the one we stabilize; except for the fact that it is less stable to change in pump power or detuning (there is a sudden transition to another state). It also exhibits different behavior with regards to degree of correlation between pump frequency and offset beat.

A.2 Microresonator dispersion and comb spectrum

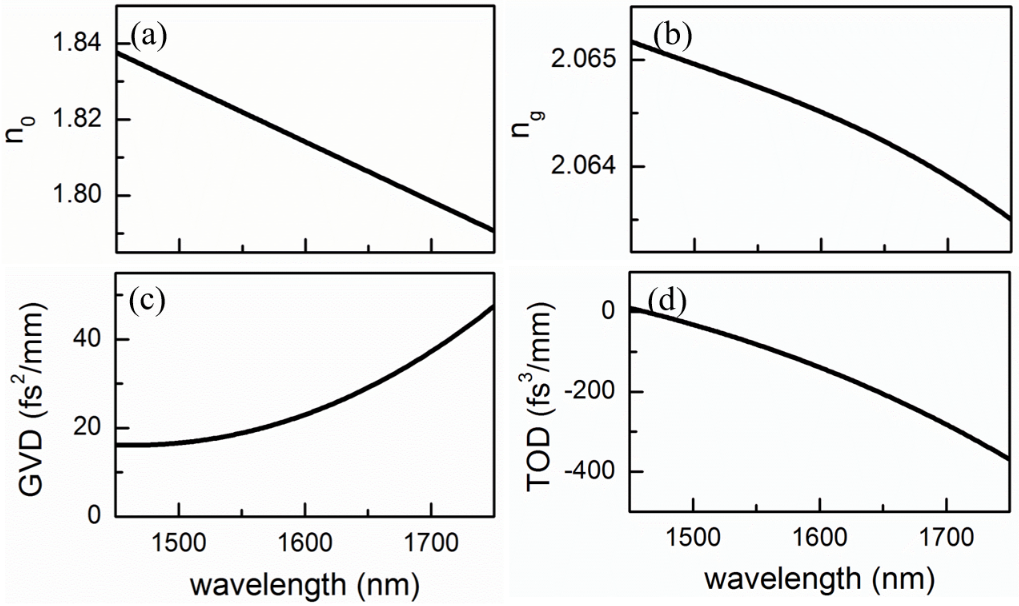

Figure A.1. Waveguide dispersion is calculated taking into account of both the material dispersion and the geometric dispersion. **(a)** Refractive index no, measured at 1.81 at pump wavelength of 1598 nm. b, Group index n_g, measured at 2.064 at the pump wavelength. c, Group velocity dispersion (GVD) measured at 23 fs^2/mm at the pump wavelength. d, Third-order dispersion (TOD) measured at 265 fs^3/mm at pump wavelength of 1598 nm.

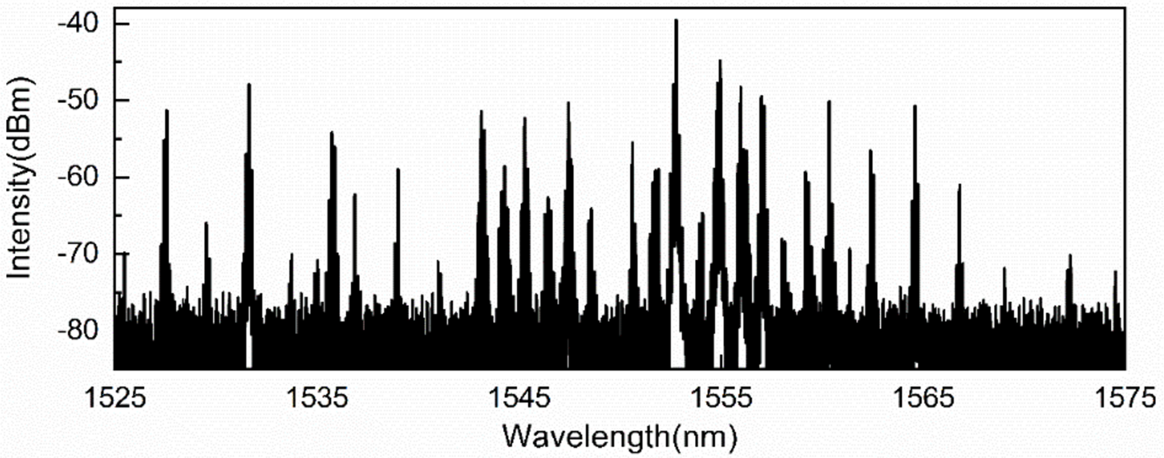

Figure A.4. Example filtered C-band frequency microcomb spectrum. Formation of primary comb lines with Δ = 1.1 nm and overlap between secondary comb lines are observed (left inset). Its electrical spectrum measures two distinct beat notes of f_{rep} = 17.9 GHz and ξ = 523.35 MHz (right inset). The highly modulated spectrum is due to mode disruptions every 4 nm, which periodically perturbs the GVD.

A.3 Derivation of the modulation instability (MI) gain peak

We investigate the intracavity MI gain and derive the frequency at which it is maximum. Equation A.1, written below describes the cavity boundary conditions and equation A.2 describes the wave propagation in the cavity when subject to chromatic dispersion and the Kerr nonlinearity [57]:

$$E^{n+1}(0,t) = \sqrt{\rho}E^{n}(L,t)\exp(i\varphi_0) + \sqrt{T}E_i, \tag{A.1}$$

$$\frac{\partial E^{n}(z,t)}{\partial z} = -i\frac{\beta_2}{2}\frac{\partial^2 E^{n}(z,t)}{\partial t^2} + i\gamma|E^{n}(z,t)|^{2}E^{n}(z,t), \tag{A.2}$$

Under the normalization $U^n = \sqrt{\gamma L}E^n$; $\kappa = \frac{z}{L}; \tau = \frac{t}{\sqrt{|\beta_2|L}}$, the NLSE is reduced to $U^n_\kappa = -i\left(\frac{\eta}{2}\right)U^n_{\tau\tau} + i|U^n|^2U^n$ where $\eta = \frac{\beta_2}{|\beta_2|}$. (To model this [51, 60, 132], here we used the more general NLSE model instead the LLE, the latter which resides under the good cavity limit and the approximation that the evolution is slow compared to round trip time.) Assume steady-state continuous wave in the cavity, one such solution is: $U^n(\kappa,\tau) = U_0\exp\left(i|U_0|^2\kappa\right)$. A periodic fluctuation generated by instability is modelled by:

$$U^n(\kappa,\tau) = \left[U_0 + v^n(\kappa)\times exp(i\Omega\tau) + v^{-n}(\kappa)\times exp(-i\Omega\tau)\right]\exp\left(i|U_0|^2\kappa\right) \tag{A.3}$$

Here Ω corresponds to the location of peak MI as will be derived subsequently. An important point to note here is that Ω may not be an exact multiple of the (normalized) f_{rep}. Substituting this in the NLSE yields after some algebra that:

$$\begin{aligned}\frac{\partial v^n}{\partial}\exp(i\Omega\tau) + \frac{\partial v^{-n}}{\partial}\exp(-i\Omega\tau) = \frac{i\eta\Omega^2}{2}\left(v^n\exp(i\Omega\tau) + v^{-n}\,exp(-i\Omega\tau)\right) + \\ i\left(\left(|U_0|^2v^n + U_0^2v^{-n*}\right)\exp(i\Omega\tau) + \left(|U_0|^2v^{-n} + U_0^2v^{n*}\right)\ exp(-i\Omega\tau)\right)\end{aligned} \tag{A.4}$$

$$\frac{\partial}{\partial}\begin{pmatrix} v^n \\ v^{-n*}\end{pmatrix} = \begin{bmatrix}\frac{i\eta\Omega^2}{2} + i|U_0|^2 & iU_0^2 \\ -i\left(U_0^*\right)^2 & \frac{-i\eta\Omega^2}{2} - i|U_0|^2\end{bmatrix}\begin{pmatrix} v^n \\ v^{-n*}\end{pmatrix}$$

The general solution to the equation above can be written as:

$$\begin{pmatrix} v^n \\ v^{-n*}\end{pmatrix} = \begin{pmatrix} a^n \\ b^n\end{pmatrix}\exp(\mu\kappa) + \begin{pmatrix} c^n \\ d^n\end{pmatrix}\exp(-\mu\kappa) \tag{A.5}$$

With eigenvalue $\mu = \Omega\sqrt{-\eta|U_0|^2 - \Omega^2/4}$ (S3) and eigenvector components satisfying:

$$\frac{a^n}{b^n} = \frac{-\left(U_0\right)^2}{\left(\frac{\eta\Omega^2}{2} + |U_0|^2 + i\mu\right)} \; ; \; \frac{d^n}{c^n} = \frac{-\left(U_0^*\right)^2}{\left(\frac{\eta\Omega^2}{2} + |U_0|^2 + i\mu\right)}$$

Now including the cavity boundary conditions (by substituting *E*_n in Supplementary Eq S1) and noting that E_{i} is a constant, we see that we can write:

$$v^{\pm(n+1)}\left(\kappa = 0\right) = \sqrt{\rho}\exp\left(i\varphi_0 + i|U_0|^2\right) v^{\pm n}\left(\kappa = 1\right) \tag{A.6}$$

Since

$$\begin{pmatrix} v^n \\ v^{-n*} \end{pmatrix} = \begin{bmatrix} 1 & 1 \\ \frac{\left(\frac{\eta\Omega^2}{2} + |U_0|^2 + i\mu\right)}{-\left(U_0\right)^2} & \frac{-\left(U_0^*\right)^2}{\left(\frac{\eta\Omega^2}{2} + |U_0|^2 + i\mu\right)} \end{bmatrix} \begin{pmatrix} a^n \\ c^n \end{pmatrix} \tag{A.7}$$

And

$$\begin{pmatrix} v^{n+1} \\ v^{-(n+1)*} \end{pmatrix} = \sqrt{\rho} \begin{bmatrix} \exp\left(i\varphi_0 + i|U_0|^2\right) & 0 \\ 0 & \exp\left(-i\varphi_0 - i|U_0|^2\right) \end{bmatrix} \begin{pmatrix} v^n \\ v^{-n*} \end{pmatrix} \tag{A.8}$$

We can write after substituting in:

$$\begin{pmatrix} a^{n+1} \\ c^{n+1} \end{pmatrix} = \frac{\sqrt{\rho}}{t^2 - |s|^2} \begin{bmatrix} -|s|^2 & st \\ t^2 & -st \end{bmatrix} \begin{bmatrix} \exp\left(i\varphi_0 + i|U_0|^2\right) & 0 \\ 0 & \exp\left(-i\varphi_0 - i|U_0|^2\right) \end{bmatrix} \begin{bmatrix} e^{\mu} & e^{-\mu} \\ te^{\mu}/s & s^*/(at) \end{bmatrix} \begin{pmatrix} a^n \\ c^n \end{pmatrix} \tag{A.9}$$

,where $s = -\left(U_0\right)^2$; $t = \frac{\eta\Omega^2}{2} + |U_0|^2 + i\mu; \vartheta = \varphi_0 + |U_0|^2$. Taking the determinant of this matrix the eigenvalues are: $q_\pm = \sqrt{\rho}\left(p \pm \sqrt{p^2 - 1}\right)$ where $p = \frac{-|s|^2\left(e^{-\mu}e^{-i\vartheta} + e^{\mu}e^{i\vartheta}\right) + t^2\left(e^{\mu}e^{-i\vartheta} + e^{-\mu}e^{i\vartheta}\right)}{2(t^2 - |s|^2)}$. Under the mean field approximation, which in this case means that $\mu \sim O\left(\varepsilon\right)$, we can approximate e^{μ} to first order as 1+, rewriting this equation $p = \cos\left(\vartheta\right) - i\mu sin\left(\vartheta\right)\frac{\left(t^2 + |s|^2\right)}{(t^2 - |s|^2)}$. Now we see that $t + |s| = \frac{-\mu^2}{2\eta\Omega^2} + i\mu$ and utilizing (S3), we can rewrite $i\mu\mu sin\left(\vartheta\right)\frac{\left(t^2 + |s|^2\right)}{(t^2 - |s|^2)}$ as $i\mu sin\left(\vartheta\right)\frac{\left(\frac{-\mu^2}{2\eta\Omega^2} + i\mu\right)}{\left(\frac{-\mu^2}{2\eta\Omega^2} + i\mu - 2|s|\right)} - i\mu sin\left(\vartheta\right)\frac{2t|s|}{\left(\frac{-\mu^2}{2\eta\Omega^2} + i\mu\right)\left(\frac{-\mu^2}{2\eta\Omega^2} + i\mu - 2|s|\right)}$ (S4) Now the first term of (S4) is of order ^{2} and is neglected while the second term reduces to $t = \frac{\eta\Omega^2}{2} + |U_0|^2 + i\mu$ and since is small, this is simply $\frac{\eta\Omega^2}{2} + |U_0|^2$. So $p = \cos\left(\vartheta\right) - \left(|U_0|^2 + \frac{\eta\Omega^2}{2}\right) sin\left(\vartheta\right)$ (S5). We note that $q_+ = \sqrt{\rho}\left(p + \sqrt{p^2 - 1}\right)$ is the (largest) eigenvalue of interest and takes its maximum for large p.

Now we write $\vartheta = 2m\pi - \delta + |U_0|^2$ where is the detuning from resonance. Applying the good cavity limit we state that both the detuning and the additional phase added per round trip due to self-phase modulation $|U_0|^2$, are small in comparison to 2. Further the good cavity limit ensures that $\rho \to 1$, we introduce the parameter = 1- where $\theta \sim O(\varepsilon)$. Subsequently (following [51]) we find that to first order the eigenvalue q_+

$$q_+ = 1 - \frac{\theta}{2} + \sqrt{4\left(\delta - \frac{\eta\Omega^2}{2}\right)|U_0|^2 - \left(\delta - \frac{\eta\Omega^2}{2}\right)^2 - 3|U_0|^4} \tag{A.10}$$

And the maxima of this eigenvalue is obtained at $\Omega_{opt} = \sqrt{2\,\eta\left(\delta - 2|U_0|^2\right)}$ which is the frequency at which MI gain is maximum. Now δ can be written as $\frac{2\pi(f_p - f_o)}{f_{rep}}$ where f_p is the pump frequency, f_{rep} is the comb spacing and f_o is the resonance frequency, f_{rep} can also be expressed as $c/(n_g L)$ and $f_o = N\frac{n_g}{n_o}f_{rep}$ where n_g is the group index and n_o is the refractive index. Furthermore $\omega = \Omega/\sqrt{|\beta_2|L}$ where ω is the frequency with respect to real time coordinates and $|U_0|^2 = \gamma L|E_o|^2$ where $|E_o|^2$ is the intracavity power, denoted by P_{int}. Putting these together we have:

$$\omega_{opt} = \sqrt{\frac{4\pi n_g\left(f_p - N\frac{n_g}{n_0}f_{rep}\right)}{\eta|\beta_2|c} - \frac{4\gamma P_{int}}{\eta|\beta_2|}} \tag{A.11}$$

This formula is intended as an approximation for the case when there is no mode interaction and close to the onset of MI. It illustrates that the breather frequency is dependent only on the two parameters P_{int} and f_p controlled by pump power and pump frequency respectively. Therefore when the pump power is locked via feedback (utilizing f_{rep} as the indicator of intracavity power), is only dependent on pump frequency f_p. The addition of periodic mode interaction and the effects of ’mode-pinning after breather comb formation introduce further complications that can be simulated in the LLE.

To perform the simulations, we first introduce a periodic mode interaction in the LLE via mode shifts (following [85]) at resonances every 4 nm. The generated comb spectrum is plotted in Fig. A.5a, we note the presence of equally spaced subcombs that are on the verge of merging similar to our generated spectrum. Fig. A.5b, plots the comb evolution with detuning swept over 100 MHz, illustrating the large stability region of our comb. We then note that the breathing frequency can in fact be seen as a slow relative phase oscillation between the pump and the first

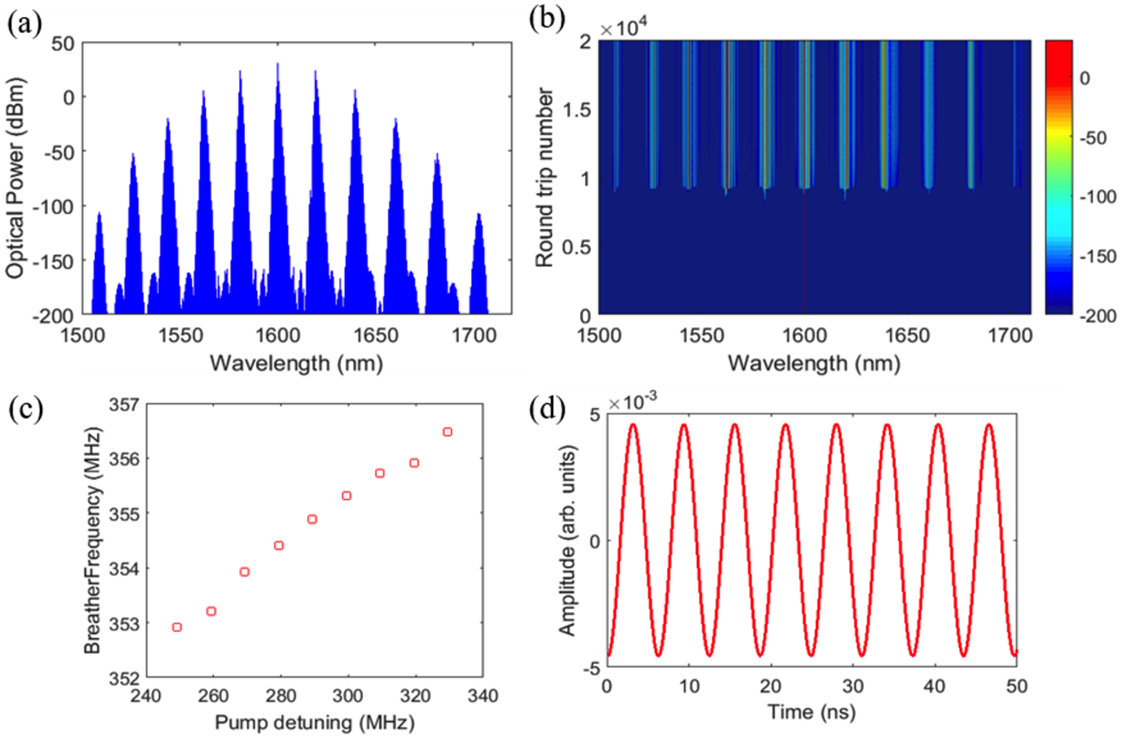

Figure A.5. **(a)** The simulated breather comb spectrum with multiple equally spaced subcombs. **(b)** Evolution of the comb spectrum in the cavity with detuning swept over 200 MHz. The spectrogram shows onset of MI at mode 20, which is disrupted in the simulation due to mode interaction and hence allows the comb to be seeded when dispersion is normal at 30 fs^2/mm. **(c)** Shows the breather frequency ξ, when pump detuning is increased and intracavity power is kept constant via a simulated PID loop. We note here that since ξ, depends both on the pump detuning and pump power, locking the power provides a direct relationship between breather frequency and pump detuning. **(d)** The slow oscillation of the relative phase between the pump and primary comb line, which manifests as the breather is plotted in time.

primary comb line as plotted in Fig. A.5d. A single cycle of this phase oscillation corresponds to a frequency of about 354 MHz, the breather frequency. In parallel to the phase, there is also a slow intensity oscillation of the comb line at the same 354 MHz that corresponds to energy being transferred from the primary lines to the pump and back. Now, finally to simulate the relationship between breather frequency and pump frequency, in conditions similar to our experiment, we simulate a PI loop to control the *intracavity power* P_{int} using only feedback to pump power. We note here (and in the main text) that since the f_{rep} is only dependent on cavity temperature [54], which in turn is entirely dependent on P_{int} (neglecting environment temperature changes), locking f_{rep} via feedback to power must necessarily lock P_{int} . This simulated loop therefore exactly corresponds to the experimentally demonstrated f_{rep} stabilization loop via pump power feedback. The PI corner and bandwidth of the simulated feedback loop is however set at 18 MHz (rather than 200 KHz), for ease of simulation to prevent unreasonably large number of round trips required for the loop to stabilize P_{int}. We subsequently ran the simulation for 5 million roundtrips with PI loop to stabilize P_{int} engaged *and* swept laser detuning while monitor change in breather frequency. Our results are plotted in Fig. A.5c, the simulated slope of change in breather frequency to change in pump detuning is $\sim$ 45 KHz/MHz.

A.4 Out-of-loop characterization

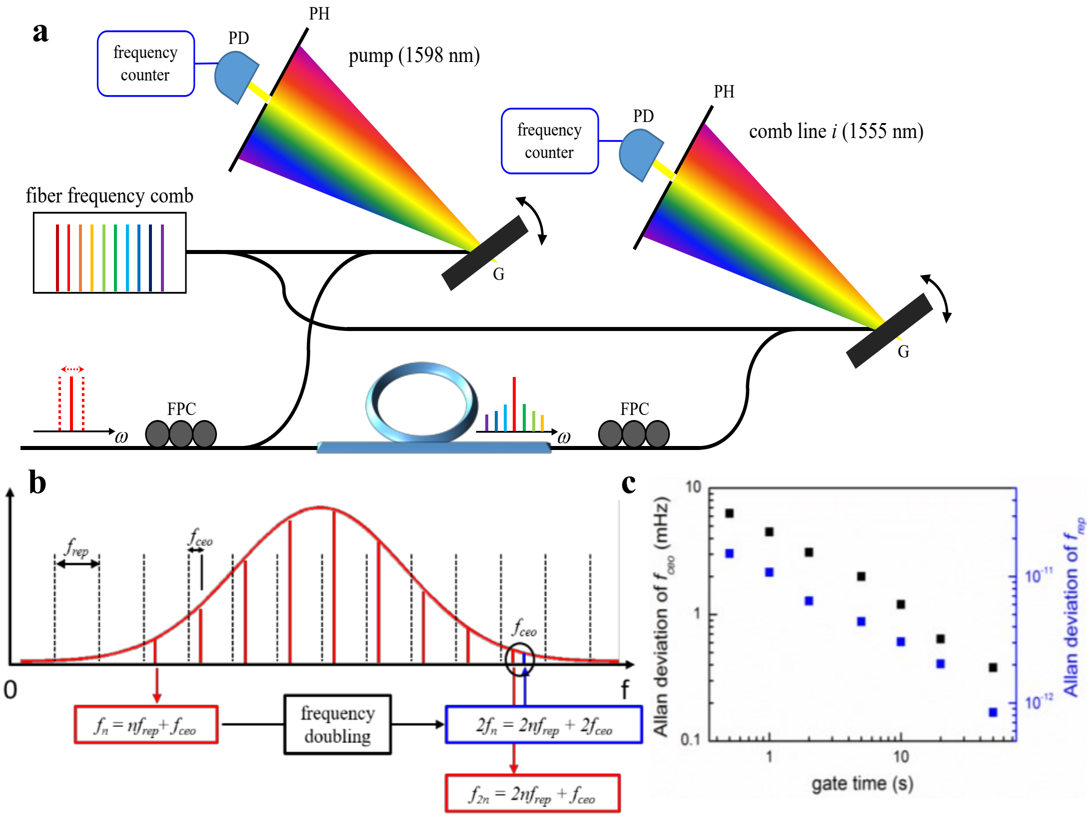

Figure A.6. **(a)** To quantify the frequency instability of the Kerr frequency comb, two comb lines (pump at 1598 nm and ith comb at 1555 nm) are compared to an independently stabilized FFC and the heterodyne beat frequencies are counted with a 10-digit, λ-type frequency counter. The FFC is referenced to a rubidium-disciplined crystal oscillator with a frequency fractional instability of 5×10^{-12} at 1 second. The gratings critically remove the unwanted reference FFC comb lines for reliable counting measurements. b, The repetition rate of the FFC ($\approx$ 250 MHz) is detected with a PD and locked to an RF local oscillator, in addition, *f-2f* interferometry is used to detect fceo and lock it to an RF reference with the same clock as that used to lock f_{rep}. c, The Allan Deviation of the fceo is plotted for the FFC in mHz and the Allan Deviation for f_{rep} is plotted relative to the carrier. As we observe from the plot, f_{rep} is the limiting factor for the stability of our reference, which is per our expectation, because of the high sensitivity of the comb line frequencies to f_{rep} due to the low optical division ratio ($\approx 10^{-6}$).

A.5 Verification of ξ across different chips and breather states

Formation of Kerr combs with a single offset beat in addition to f_{rep} is not a unique property dependent on microresonator characteristics but in fact is general and arises from the mechanics of Kerr comb generation. These combs have also been observed previously in microresonators [13,14], but with very different characteristics. In addition, to the 18 GHz comb described in the main text, we also observe a similar state in a single mode Si_3N_4 microresonator cavity with a tapered structure [56] thereby verifying the applicability of our approach across different breather comb states and chipsets. The comb spectrum is shown in Fig. A.7a. and the offset beat is measured in different comb slices, as shown in Fig. A.7b, to verify that it is truly a single offset comb state. Breather combs in general have a modulated spectrum such as in Fig. A.7a, this may limit performance in some applications such as the spectral density in dense-wavelength optical communications. However, breather solitons can provide both the breathing frequency for locking while having a smooth spectrum for various applications for further studies.

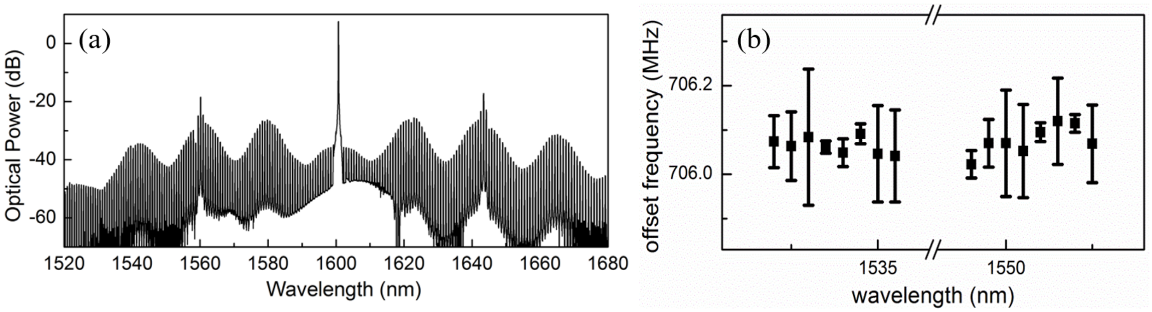

Figure A.7. **(a)** Spectrum of a comb-state, similar to the one we stabilize, generated in a single mode microresonator with a tapered structure. This comb state generates a single offset beat ξ in the RF domain in addition to the repetition rate. b, To verify that the offset frequency is uniquely defined across the whole Kerr frequency comb, we measure it at various different spectral segments with a tunable filter (0.22 nm FWHM filter bandwidth). Free-running ξ without f_{rep} stabilization ($\approx$ 700 MHz) in different spectral regions is measured to be the same within error bars of $\approx$ 200 kHz. At wavelengths where the beat notes have SNR higher than 10 dB (100 kHz RBW), 10 measurements are taken to determine the mean value of the offset frequency. The error bar of the measurement is defined as the peak-to-peak deviation from the 10 measurements.

A.6 Verification of stabilization of f_{rep} stabilization after locking ξ

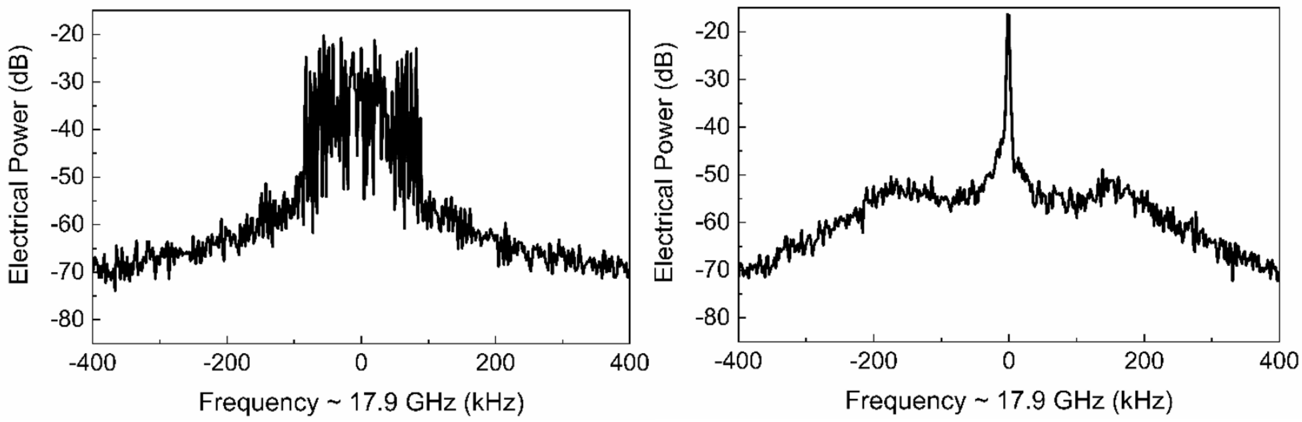

Figure A.8. **(a)** f_{rep} measured at an RBW of 1 kHz before locking ξ but after locking pump frequency, b, f_{rep} measured after locking ξ at an RBW of 1 kHz. Locking sidebands are observed at $\approx$ 200 kHz, corresponding to the PI corner of the feedback loop intended to stabilize ξ. Stabilization of f_{rep} is clearly observed subsequent to locking ξ. Furthermore, as explained in the main text, we expect the phase noise of this signal to be $\approx$ 38 dB lower than the phase noise of the locked signal ξ after division to the same carrier.

APPENDIX B

Graphene-nitride resonator tuning and fabrication

B.1 Theoretical analysis and numerical simulations of graphene-nitride microresonator tuning

B.1.1 Principle of the dispersion modulation in graphene-silicon nitride microresonator

The carrier density of graphene is tunable via an external electrical field. Let us start with describing solely the graphene layer. During the gate tuning process, conductivity of graphene is modulated, which is written as [133, 134]:

$$\sigma_g(f, E_F, \tau, T) = \sigma_{g,intra} + \sigma_{g,inter} = \frac{ie^2(2\pi f - i/\tau)}{\pi\hbar^2}\left\{\frac{1}{\left(2\pi f + \frac{i}{\tau}\right)^2}\right. \int_0^\infty \varepsilon\left[\frac{\partial f_d(\epsilon)}{\partial\epsilon} - \frac{\partial f_d(-\epsilon)}{\partial\epsilon}\right]d\epsilon - \left.\int_0^\infty \varepsilon\left[\frac{f_d(-\epsilon) - f_d(\epsilon)}{(2\pi f + i/\tau)^2 - 4(\epsilon/\hbar)^2}\right]d\epsilon\right\} \tag{B.1}$$

Specifically,

$$\sigma_{g,intra} = \frac{ie^2 E_F}{\pi\hbar\left(2\pi f + \frac{i}{\tau}\right)} \tag{B.2}$$

$$\sigma_{g,inter} = \frac{ie^2 E_F}{4\pi\hbar}\, ln\left[\frac{2|E_F| - \hbar(2\pi f + \frac{i}{\tau})}{2|E_F| + \hbar(2\pi f + \frac{i}{\tau})}\right] \tag{B.3}$$

Here E_F is the quasi Fermi level, directly determined by the external bias. f is the optical frequency, $\tau \approx 10^{-13}s$ is the carrier relaxation lifetime, Tis the temperature, $f_d(\epsilon) = (exp[(\epsilon - \mu)/k_B T] + 1)^{-1}$is the Fermi-Dirac distribution, $\hbar = 1.05 \times 10^{-34} eVs$ is the reduced Planck constant, $k_B = 1.3806505 \times 10^{-23}\ J/K$ is the Boltzmann's constant, and $e = -1.6 \times 10^{-19}C$ is the unit charge. Treating graphene as an ultrathin optical media with sheet conductivity, its effective permittivity and refractive index is determined by its complex conductivity [73, 135, 136]:

$$\begin{cases} \epsilon_g = \dfrac{-\sigma_{g,i} + i\sigma_{g,r}}{2\pi f \Delta} \\ (n_{g,r} + in_{g,i})^2 = \epsilon_{g,r} + i\epsilon_{g,i} \end{cases} \tag{B.4}$$

For the media mode $n_{g,r} > 0$ and we get the values of $n_{g,r}$ and $n_{g,i}$ as

$$\begin{cases} n_{g,r} = \dfrac{2\epsilon_{g,r}\left(\frac{\epsilon_{g,r}}{2} + \frac{\sqrt{\epsilon_{g,r}^2 - \epsilon_{g,i}^2}}{2}\right)^{1/2} - 2\left(\frac{\epsilon_{g,r}}{2} + \frac{\sqrt{\epsilon_{g,r}^2 - \epsilon_{g,i}^2}}{2}\right)^{3/2}}{\epsilon_{g,i}} \\ n_{g,i} = \left(\dfrac{\epsilon_{g,r}}{2} + \dfrac{\sqrt{\epsilon_{g,r}^2 - \epsilon_{g,i}^2}}{2}\right)^{1/2} \end{cases} \tag{B.5}$$

For propagating light, $n_{g,r}$ influences the phase velocity while $n_{g,i}$ refers to the propagation loss [137]. Based on the dispersion $n_g(f, \mu)$, the gate-tunable GVD parameter of graphene D_g can be calculated:

$$\beta_m = \left(\frac{d^m \beta}{d\omega_m}\right) \tag{B.6}$$

$$D_g = -\frac{2\pi c}{\lambda^2}\beta_2 = -\frac{\lambda}{c}\frac{d^2 n_{g,r}}{d\lambda^2} \tag{B.7}$$

Here $\omega = 2\pi c/\lambda$, m is the order, β_2 is the GVD and β_3 is the TOD. Figure S1 plots the calculated spectra of ϵ_g, n_g and D_g, for a series of Fermi levels. With increasing Fermi level the graphene dispersion is sizably tuned, from anomalous to normal, and then finally back to anomalous.

In this work, atomic layer graphene is deposited onto the silicon nitride waveguides. Standard optical parameters of silicon nitride waveguide are calculated in Figure B.2. Figure B.2a, B.2b and B.2c shows the group velocities, the GVD (β_2) and the TOD (β_3) of the silicon nitride waveguides. All the results are calculated based on TE polarization. Here the numbers marked in the figures are the width of the silicon nitride waveguides, with a fixed height 0.8 μm. The blue curves highlight the results of width = 1.2 μm, which is applied in our experiment. By using the finite-element method, Figure B.3 demonstrates the simulated $|E|$-field distributions of the silicon nitride waveguides with 1200 × 800 nm^2 core, for optical wavelength 1600 nm. Figure B.3a to B.3c are the simulated results of the TE_{01} mode while Figure B.3d to B.3f show the TM_{01} mode. In this simulation, we fix the parameters: graphene Fermi level at 0.5 eV, graphene thickness of 0.5 nm,

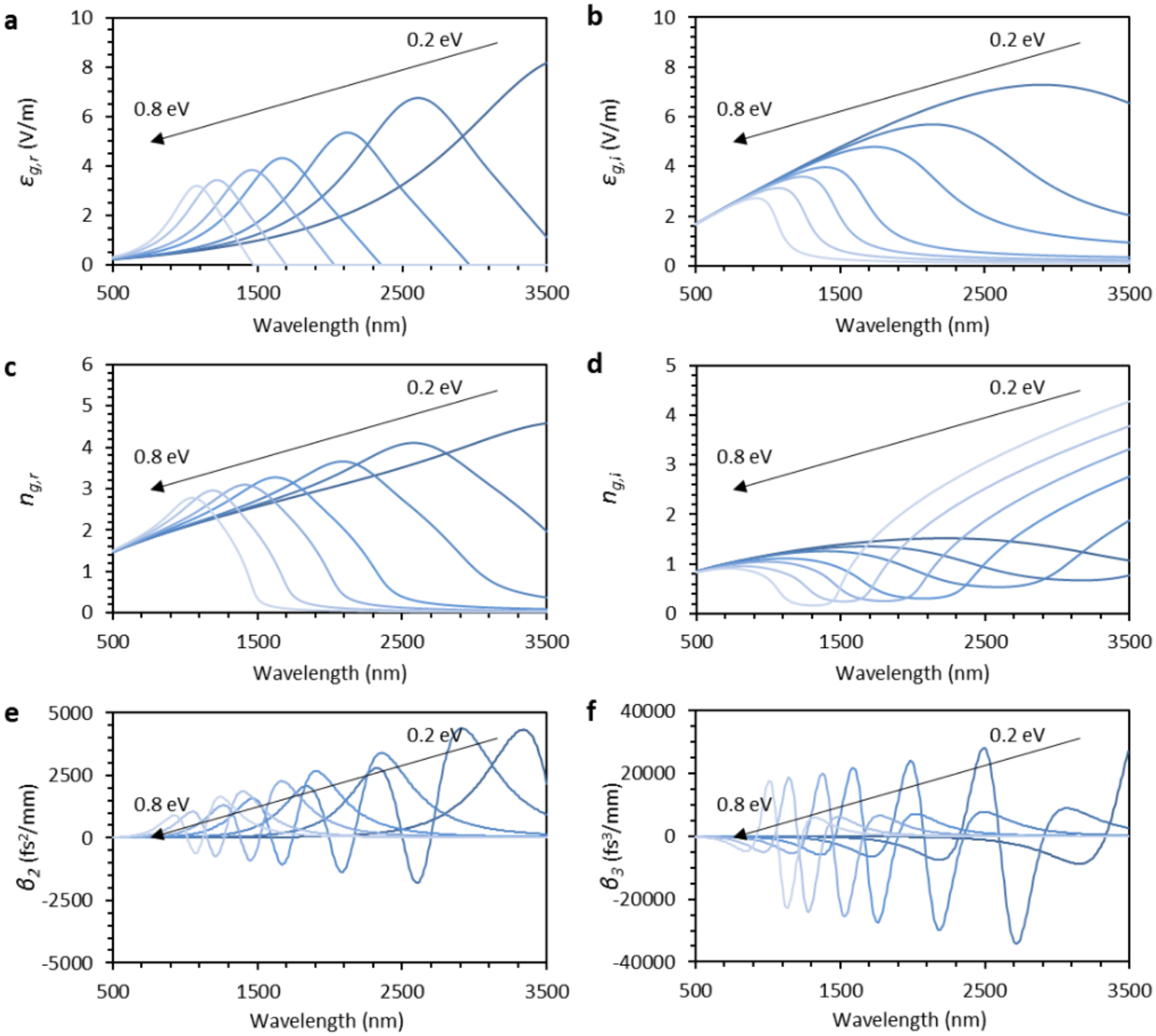

Figure B.1. a and b, Real part and imaginary part of the graphene permittivity, under varying from 0.2 eV to 0.8 eV (labeled from dark blue to light blue). c and d, Real part and imaginary part of the refractive index. e,Group velocity dispersion (GVD). f,Third-order dispersion (TOD).

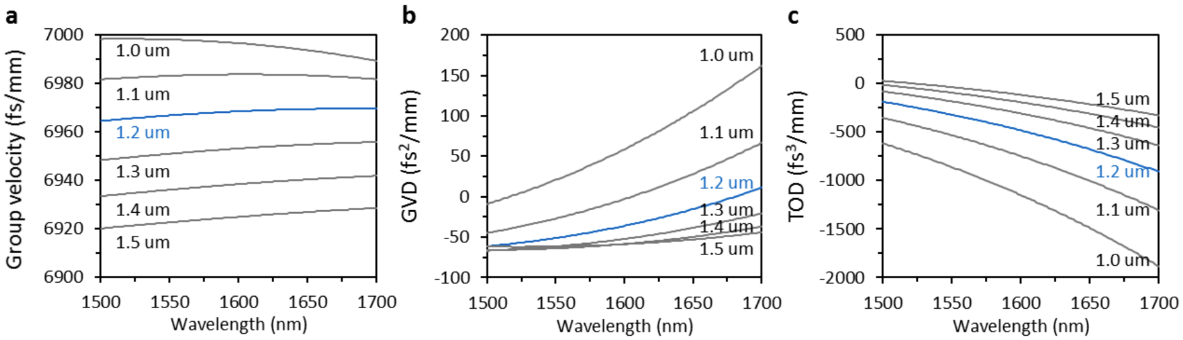

Figure B.2. a, group velocities. b, GVD. c, TOD. Waveguide height: 0.8 μm; waveguide width varies from 1.0 μm to 1.5 μm.

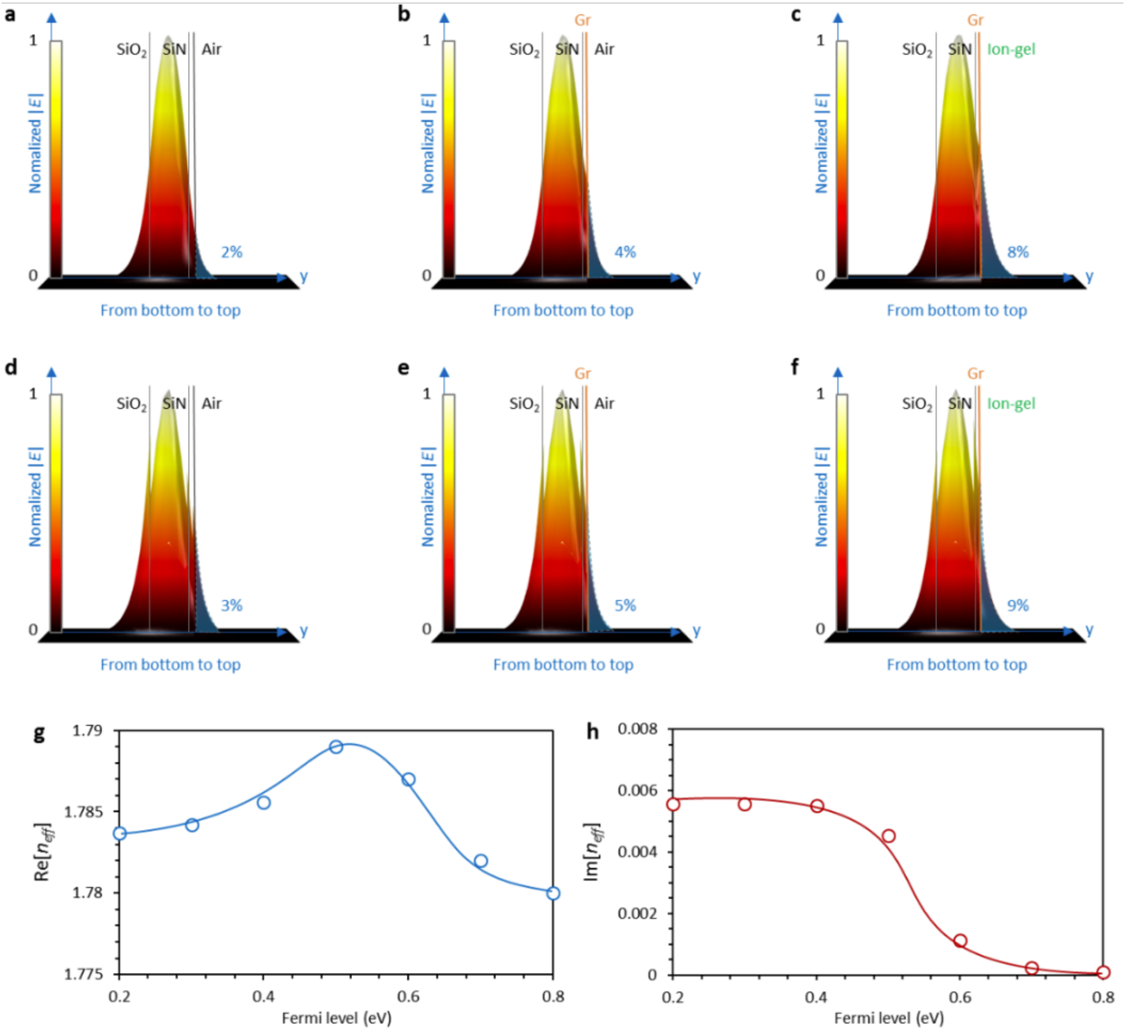

Figure B.3. a-c, TE$_{01}$mode distributions in the top etched nitride waveguide, after the graphene deposition, and after the ion-gel coverage. d-f, TM$_{01}$ mode distributions in the top etched nitride waveguide, after the graphene deposition, and after the ion-gel coverage. g-h, During Fermi level increases from 0.2 eV to 0.8 eV, real part and imaginary part of the fundamental TE$_{01}$ mode. In these simulations, Si_3N_4 cross-sectional size is $1200 \times 800\, nm^2$.

ion-gel thickness of 1 μm with refractive index of 1.420 [138], silicon nitride refractive index of 1.996, silica refractive index of 1.462. Determined by the electromagnetic boundary conditions, distributions of the TM_{01} mode are not continuous along the y-axis. For TE_{01} mode, before graphene deposition, $\approx 2\%$ mode intensity distribute in the air. Afterwards, determined by the high index of graphene (3.27+i0.65 at 0.5 eV), more mode energy ($\approx 4\%$) distributes outside, enhancing the light-graphene interaction. Finally, by covering the ion-gel on the graphene, we further increase the evanescent field distribution, up to $\approx 8\%$ overlapping above the graphene sheet. Spatial distributions of the TM_{01} mode are similar. Enhanced by the graphene and ion-gel, mode field intensity out of the nitride/oxide waveguide increases from $\approx 3\%$ to $\approx 9\%$. However, determined by the polarization dependent loss induced by scattering and absorption, Q factor of the TM_{01} mode is much lower than the TE_{01} mode.Furthermore, by modulating the n_g via gate tuning, effective index of the hybrid waveguide n_eff changes correspondingly [139,140]. Figure B.3g and B.3h plots the calculated effective index of the fundamental TE_{01} mode, at 1600 nm wavelength in the hybrid waveguide during the graphene Fermi level tuning from 0.2 eV to 0.8 eV.

To calculate the dispersion of the whole microresonator at 1600 nm wavelength, Figure B.4a shows the segmentation of the geometry. Arc lengths of L_A, L_B and L_C are $\approx$ 790 μm, $\approx$ 220 μm, and $\approx$ 90 μm respectively. We denote the respective GVDs as β_A, β_B, and β_C, separately calculated with COMSOL. Total dispersion of the microring resonator is thus written as $\beta_2 = (\beta_A L_A + \beta_B L_B + \beta_C L_C)/(L_A + L_B + L_C)$. Figure B.4b plots the calculated β_A, β_B, and β_C during the gate tuning operation, with the following three observations: (1) gate voltage does not affect β_A which is kept constant around -38 fs^2/mm. (2) due to the motion of the ions and thermal heating of the ion-gel, the refractive index of section L_B decreases slightly by $\approx$ 0.001 at 1600 nm [141], with β_B increasing slightly from $\approx$-42 fs^2/mm to $\approx$-34 fs^2/mm in linear approximation, under gate voltage tuning from 0 V to -2 V. Compared to graphene, such a GVD modification from

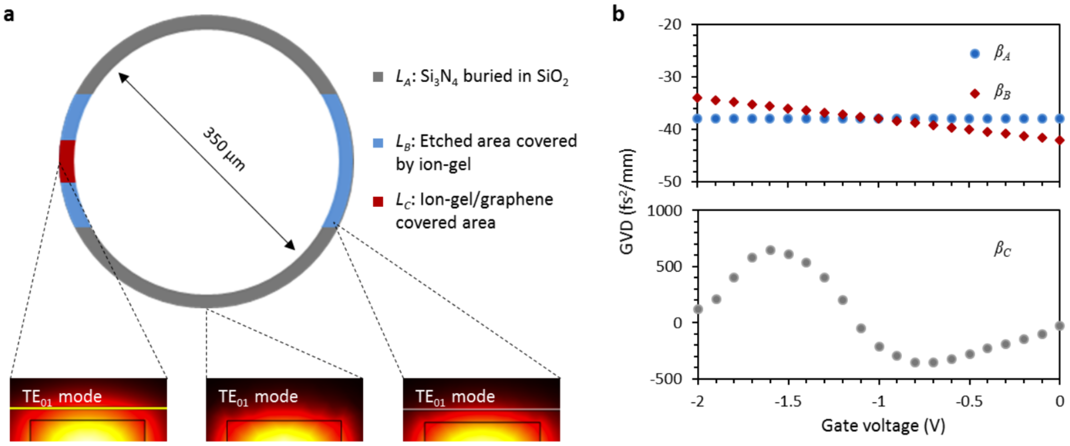

Figure B.4. a, Top-view geometry of the graphene basedmicroresonator.Three sections are marked: L_A, the nitride core buried in oxide cladding, L_B, the etched area covered by Ion-gel, L_C, the graphene heterostructured area. Inset: the TE$_{01}$ mode in the 3 sections has different spatial patterns. b, Calculated GVDs of the 3 sections.

the ion gel and nitride temperature variation is more than two orders-of-magnitude smaller. (3) for the graphene/ion-gel heterostructure, β_C oscillates dramatically compared to β_A and β_B.

Reflection or backward scattering in high Q microresonators may cause standing-wave modes [142–144]. For frequency comb generations pumped at high power, strong standing waves which may induce hole-burning should be avoided. In our graphene heterostructured nitride microresonator, because graphene's thickness is only $\approx$ 5Å and the single-mode (TE_{01}) wavevector is parallel to the graphene sheet, the scattering is negligibly weak. For example, we do not observed mode-splitting in transmission and high-resolution spectral measurements on our high Q microresonator measurements, aided by the nitride waveguide uniformity. To further support this, Figure B.5a shows our calculated reflection ratios of the TE_{01} mode, R_G, based on Fresnel equation. Determined by the Fermi level of graphene, R_G changes via gate tuning, with the highest value of R_G at 0.24$\%$ for the graphene Fermi level $|E_F|$ at $\approx$ 0.5 eV. Figure B.5b further simulates a waveform example (via COMSOL) along the microresonator, for $|E_F|$= 0.5 eV, with little reflections at the graphene/ion-gel interface.

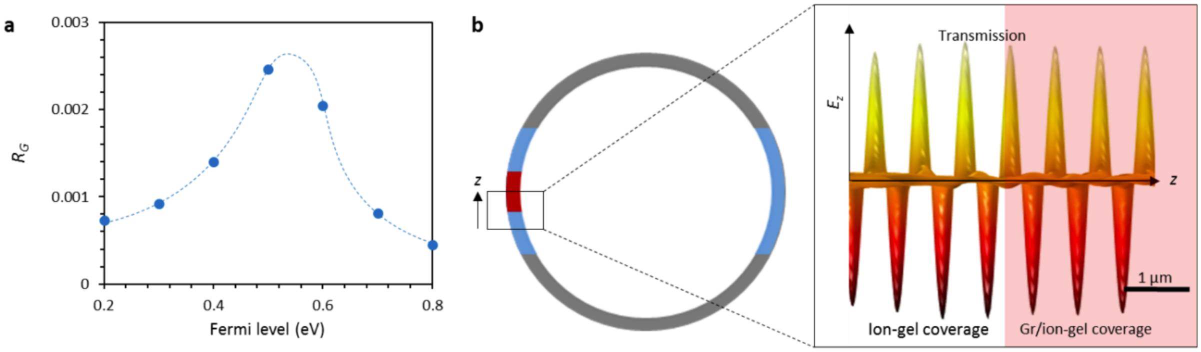

Figure B.5. a, Calculated reflection ratio at the boundary of ion-gel nitride section / heterogeneous graphene-nitride, changing in range of 0.08% to 0.24% with Fermi level tuning and gate modulation. b, Simulated spatial waveform in the microresonator. Here z shows the clockwise direction.

B.1.2 Third-order nonlinearity of graphene

It is known that graphene has a large optical nonlinearity, contributing to the four-wave mixing process [74, 145]. The nonlinear parameter γ of the graphene ring resonator could be written as $\gamma = 3Re[2\pi f\chi^{(3)}/n_{eff}cA_{eff}]$, wherein $\chi^{(3)}$ is the third-order nonlinear susceptibility and A_{eff} is the effective mode area [146]. Figure B.6 shows the γ of graphene, the silicon nitride core, and the hybrid waveguide respectively. For $|E_F|> 0.3eV$, a higher Fermi level brings a lower γ [147, 148]. Compared to silicon nitride, the third-order nonlinearity parameter of graphene is over 2 orders-of-magnitude higher. However, graphene only affects the evanescent field of the ring and hence the overall field-averaged enhancement with graphene is only slightly larger than nitride in this case: when E_F is tuned higher than 0.6 eV, γ of the hybrid waveguide is $\approx 3 \times 10^3\, m^{-1}W^{-1}$.

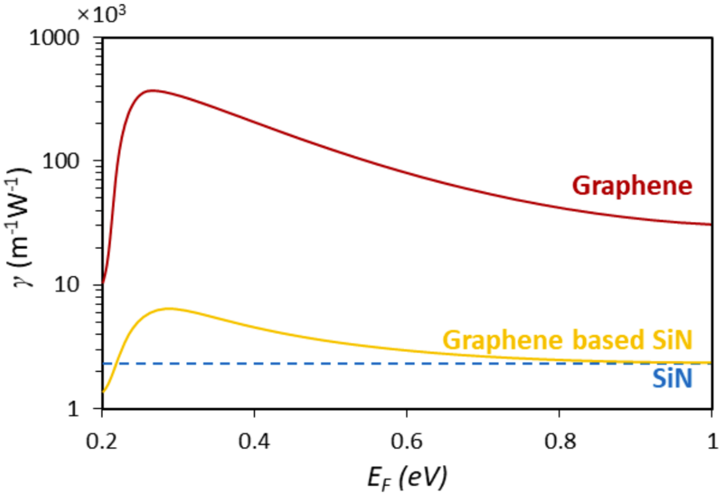

Figure B.6. Red solid line: graphene; blue dashed line: silicon nitride; gold solid line: graphene-silicon nitride hybrid.

B.1.3 Cherenkov radiation and soliton generation

Optical Cherenkov radiation, also known as dispersive wave, describes the radiation from a canonical soliton when perturbed by higher-order dispersions [28,149,150]. As shown in Figure 3.1 , not only the GVD, β_2, but also the TOD, β_3, can be tuned by changing the gate voltage to the graphene layer.Thus, the spectral peak of the Cherenkov radiation is also gate-tunable in the graphene-nitride microresonators.

For efficient energy conversion from the canonical soliton to the optical Cherenkov radiation, their propagation constants have to be matched and thus

$$\beta_s = \beta_0 + \beta_1(\omega_D - \omega_s) + \gamma P/2 = \beta_0 + \beta_1(\omega_D - \omega_s) + \sum_{N\geq 2} \frac{\beta_N(\omega_D - \omega_S)^N}{N!} = \beta_D \tag{B.8}$$

where β_S and β_D are the propagation constants of the canonical soliton and the Cherenkov radiation respectively, γ is the nonlinear coefficient, Pis the pump power, ω_S and ω_D are the center frequencies of the canonical soliton and the Cherenkov radiation respectively.Assuming the Cherenkov radiation is spectrally well separated from the canonical soliton, $\gamma P << \beta_2(\omega_D - \omega_S)^2$, the phase

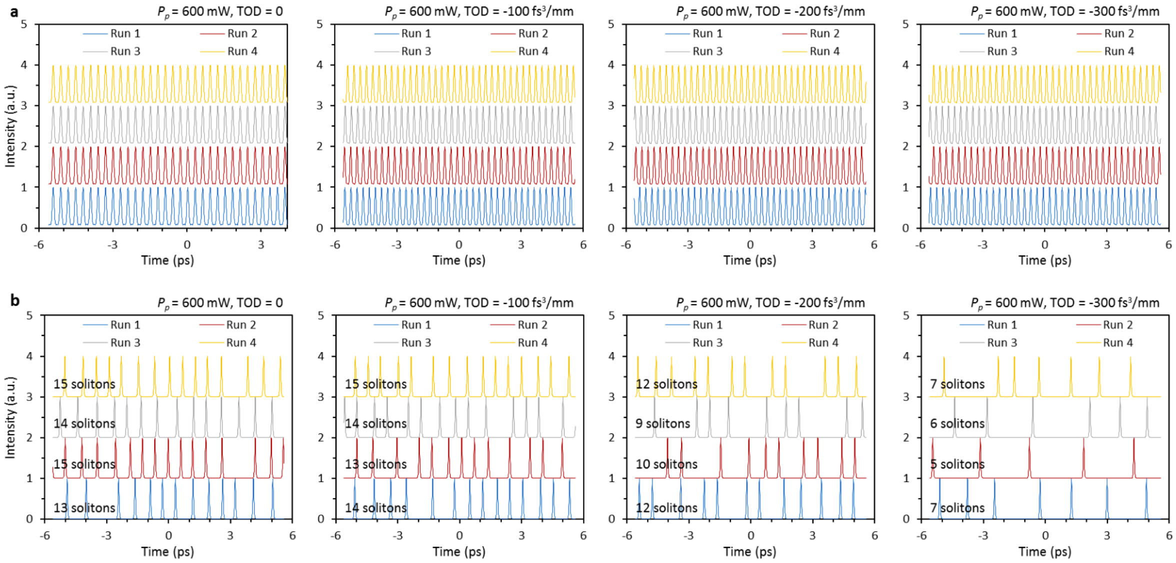

Figure B.7. a, Turing patterns. b, Final formations of the multi-solitons. In the simulations, we use on-chip pump power 600 mW, GVD -30 fs^2/mm, intrinsic Q factor 1.061×10^6, cavity length 1.1 mm, effective mode area 1 μm^2, central wavelength 1600 nm

matching condition can be simplified as

$$f_D = f_S + \frac{3}{2\pi}\frac{|\beta_2|}{\beta_3} \tag{B.9}$$

In the Kerr comb evolution, Turing patterns [84, 151], chaotic states [152] and soliton states [20, 153] appear successively. Taking advantage of the Lugiato-Lefever mean-field model [29], we show the difference of the Turing patterns before chaotic state and the finally formed solitons after chaotic state in Figure B.7. We note that when the TOD higher than -300 fs^3/mm, it is hard to generate single soliton state by using a 600 mW on-chip pump.During the pulse evolution, multi-soliton states with versatile pulse operations are essential processes, which are also timely stable, having shown great potential in applications such as harmonic sources and ultrafast information-processes [39, 130, 154].

Moreover, we demonstrate the simulated results of the Cherenkov soliton formations in Figure B.8. Here we use TOD varying from -300 fs^3/mm to -500 fs^3/mm. Figure B.7a to B.7c plot the temporal profiles of the final soliton formations. Figure B.7d to B.7f show the statistical histograms. For TOD at-300 fs^3/mm, -400 fs^3/mm and -500 fs^3/mm, possibility of single soliton generation is estimated 0%, 44%, and 67%, respectively. The simulated results imply that for a specific GMR, single soliton tends to appear with a larger TOD and a larger pump power. For the GMR, however, a larger TOD brings higher sensitivity of GVD spectrally, which then increases the difficulty for single soliton thermal stabilization.

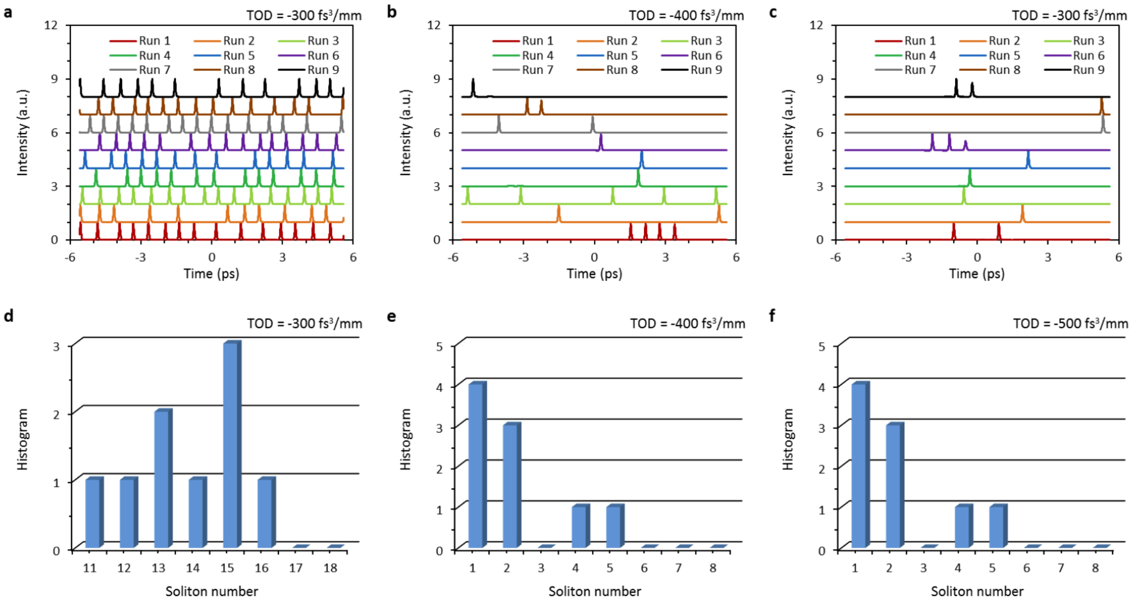

Figure B.8. a to c, Modelled soliton structures for TOD at -300 fs^3/mm, -400 fs^3/mm, and -500 fs^3/mm respectively. d to f, Occurrence distributions of the soliton numbers. In the simulations, we use a GVD of -30 fs2/mm, an intrinsic Q factor of 1.06×10^6, a cavity length of 1.1 mm, an effective mode area of 1 μm^2, and a central pump wavelength of 1600 nm.

B.2 Fabrication and baseline characterization

Figure B.9 shows the fabrication process flow of the graphene-based Si3N4 microresonators. The microresonator has a cross-sectional 1000×800 nm^2 bus waveguide and a cross-sectional 1200 $\times 800$ nm^2 core for the ring. Above the ring, there is 2500 nm thick SiO2. First, by using standard photo-lithography followed by buffered oxide etching (7 mins), we create a photoresist window above the ring and etched the SiO2 to between 100 and 400 nm thick for better graphene-light interaction and chromatic dispersion management. We note that the edge of the ring need to be well protected by ultra-thick photoresist ($\approx$ 1 mm) to prevent damage from the etching process.

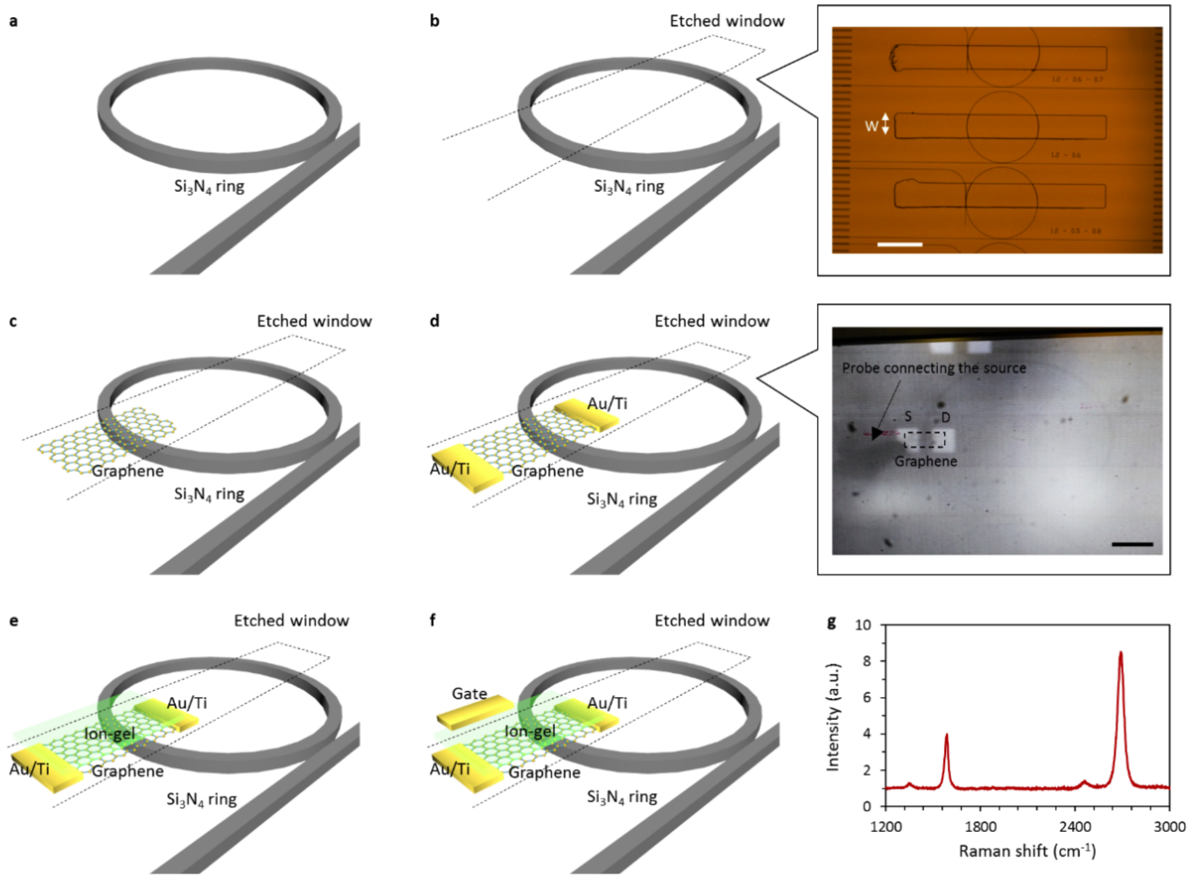

Figure B.9. a, Schematics of silicon nitride ring resonator buried in silica cladding. b, Schematics (left) and the top-view microscope image (right) of the chip after photolithography and oxide etching. Scale bar: 300 μm. c, Schematic of a monolayer graphene transferred and patterned in the etched window. d, Schematic (left) and top view image(right) of the device with source-drain electrodes integrated on graphene. Scale bar: 100 μm. e, Schematics of graphene source-drain-dielectric with a layer of ionic liquid as the gate dielectric. f, Schematics of device structure with gate electrode integrated. g, Raman spectrum of the monolayer graphene.

Inset of Figure B.9b shows the top-view image of the substrate with an etched oxide window. Secondly, we transfer a monolayer graphene on the etched window, followed by photolithography patterning and oxygen plasma etching, as shown in Figure B.9c. The graphene layer is grown by low pressure chemical vapor deposition (LPCVD) method on copper substrate and transferred using a modified transfer technique using PPC (polypropylene carbonate) as the protection layer. The LPCVD and PPC transfer here is essential to integrate high quality graphene on top of the ring. Next, as shown in Figure B.9d, we deposit source drain electrodes (Ti/Au, 70/100 nm) using photo lithography and e-beam evaporation. Here the size of the pads is 80 μm$\times$ 60 μm. Inset of Figure B.9d shows the microscope image of this step, with the chip put on the setup. Finally, we integrate ionic liquid (DEME-TFSI (N,N-diethyl-Nmethyl-N-(2-methoxyethyl) ammonium bis (trifluoromethylsulfonyl) imide, from Sigma-Aldrich) as the gate dielectric, resulting an electric double layer graphene transistor with large gate capacitance. Raman spectrum of the monolayer graphene is shown in Figure B.9g, indicating the high quality of CVD grown graphene [155].

B.3 Supplemental measurements

B.3.1 Setup for gate tunable comb generation

Figure B.10a shows the experimental setup for comb generation and modulation. A tunable laser (Santec 710) with tunable range from 1480 nm to1640 nm serves as the drive laser. It is amplified by an erbium doped fiber amplifier (EDFA, BKtel)in the L-band, working as the pump. In the experiment, the laser is tuned around 1600 nm, and the amplified power is 3.16 W (35 dBm). The pump beam is launched on to the chip via free-space. A polarization controller (PC) and a polarized beam splitter (PBS) are used to ensure the launched light is in the transverse electric (TE)mode. The graphene heterostructured microresonator (GMR) chip is fixed on a chip holder, whose temperature is controlled with a thermoelectric cooler. To tune the comb, the GMR is gated by a pair of electrical probes. For the comb spectra, the output signal is analyzed by an optical spectrum analyzer (Advantest Q8384; Yokogawa AQ6375). Figure B.10b shows the setup to gate the graphene-based resonator chip. Here, two probes connect the gate and source separately. The drive laser is launched onto the chip via optimized and matched coupling lens. Figure B.6c shows the image of the gated chip under an infrared camera; here the Au/Ti patterns deposited on the chip are the bright spots and the source and drain with graphene are marked by ‘S’ and ‘D’. A probe inserting in the ion gel (without touching the chip) works as the top gate, marked as ‘G’. In addition, here the etched window is marked by the blue dashed box and the silicon nitride resonator is marked by the red dashed ring.

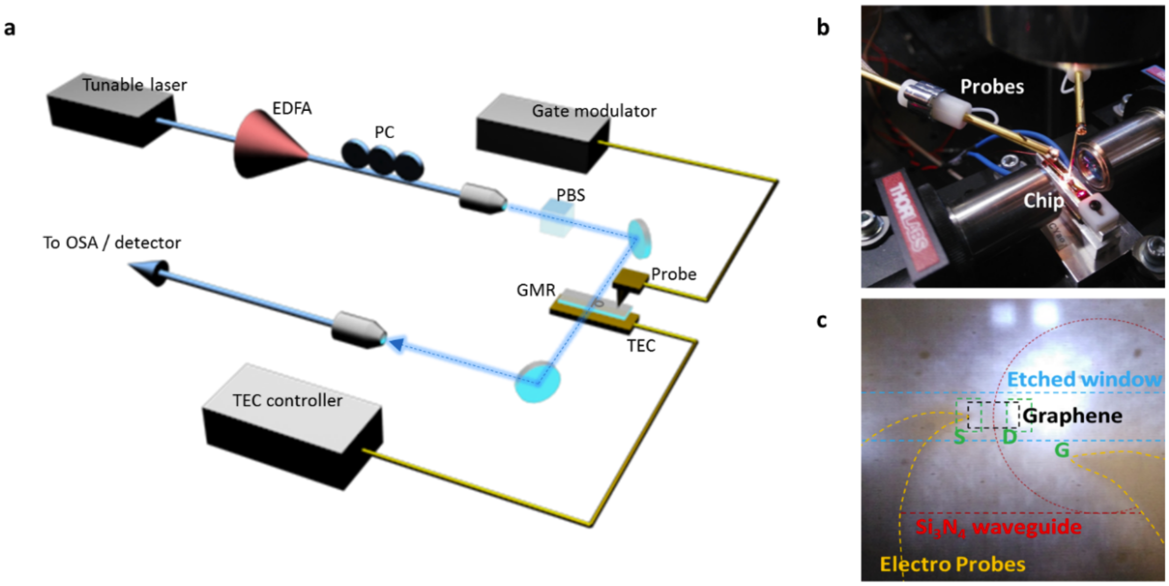

Figure B.10. a, Schematic of the experimental setup. b, Probing and aligning the graphene microring resonator chip. c, Microscope image of the probed chip in experiment, under an infrared camera. The ring resonator is covered by the ion-gel. EDFA: erbium-doped fiber amplifier. PC: polarization controller. PBS: polarization beam splitter. GMR: graphene microring chip. TEC: thermoelectric cooler for chip temperature control.

B.3.2 MZI-clocked dispersion measurement, withHCN optical transition referencing

Figure B.11shows the setup for the graphene resonator transmission and dispersion measurement [56]. The graphene microring resonator transmission is measured using a tunable laser swept through its full wavelength tuning range at 40 nm/s. Accordingly we can get its dispersion and Q factors. For accurate wavelength calibration, 1% of the laser output is directed onto a fiber-coupled hydrogen cyanide gas cell (HCN-13-100, Wavelength References) and then into a photodetector (PD 1). The graphene microring resonator and gas cell transmission are recorded during the laser sweep by a data acquisition system whose sample clock is derived from a photodetector (PD 2),monitoring the laser transmission through an unbalanced fiber Mach-Zehnder interferometer (MZI). The MZI has a determined 40 m path length difference, ensuring a measurement optical frequency sampling resolution of 5 MHz.The absolute wavelength of each sweep is determined by fitting 51 absorption features present in the gas cell transmission to determine their subsample position, assigning them to known traceable wavelengths and calculating a linear fit in order to determine the full sweep wavelength information. Each resonance is fitted with a Lorentzian lineshape unless a cluster of resonances is deemed too close to achieve a conclusive fit with a single Lorentzian. In that case, an N-Lorentzian fit is utilized where N is the number of resonances being fitted. The dispersion of the graphene ring resonator is finally determined by analyzing the wavelength dependence of the FSR.In the setup, the graphene microring resonator chip is gated by a probe.

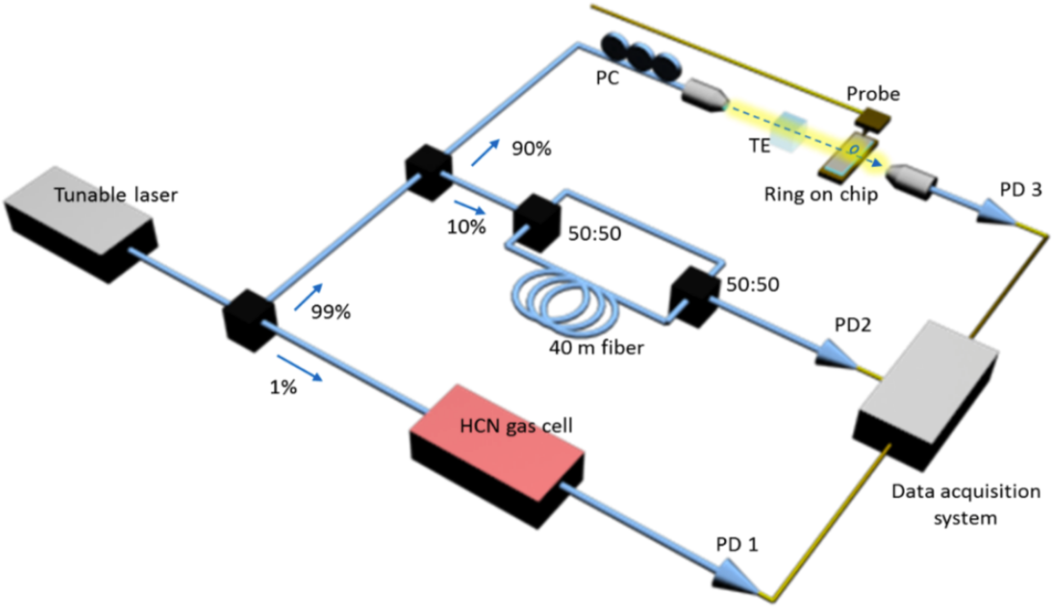

Figure B.11. The swept input laser is clocked with a highly-imbalanced MZI with 5 MHz optical frequency sampling resolution, and referenced against the optical transitions of a HCN reference gas cell. PC: polarization controller. TE: transverse electric mode. HCN: hydrogen cyanide. PD: photodetector

B.3.3 Heterodyne beat notes and autocorrelation measurements for soliton states

To measure the stability and soliton states of our frequency comb, Figure B.12a shows our optical heterodyne setup. We use a WDM to separate the C-band comb lines (1530 nm -1570 nm) and the L-band comb lines (1570 nm - 1630 nm) from the pump. The 1570 nm -1630 nm window is monitored by an OSA (Advantest AQ8384).The 1530 nm -1570 nm spectrum beats with a stable continuous-wave (CW) laser with a narrow linewidth (300kHz, New Focus), which serves as the heterodyne reference. A PC is used to optimize the pump polarization. The beatnotes are measured by a 3 GHz RF ESA (Agilent CXA 9000A). The comb signal is also measured in the time-domain, using a built optical intensity autocorrelator (AC). In this part, a 7meter long dispersion-compensated fiber (DCF)along with a15 meter long single-mode fiber is used to compensate the GVD, avoiding the pulse broadening. Figure B.12b shows the measured AC traces of our graphene based microresonator. With decreasing the pump detuning, we demonstrated the Turing patterns with dense oscillation but low extinction ratio (<3 dB), high noise state, and stable soliton states.

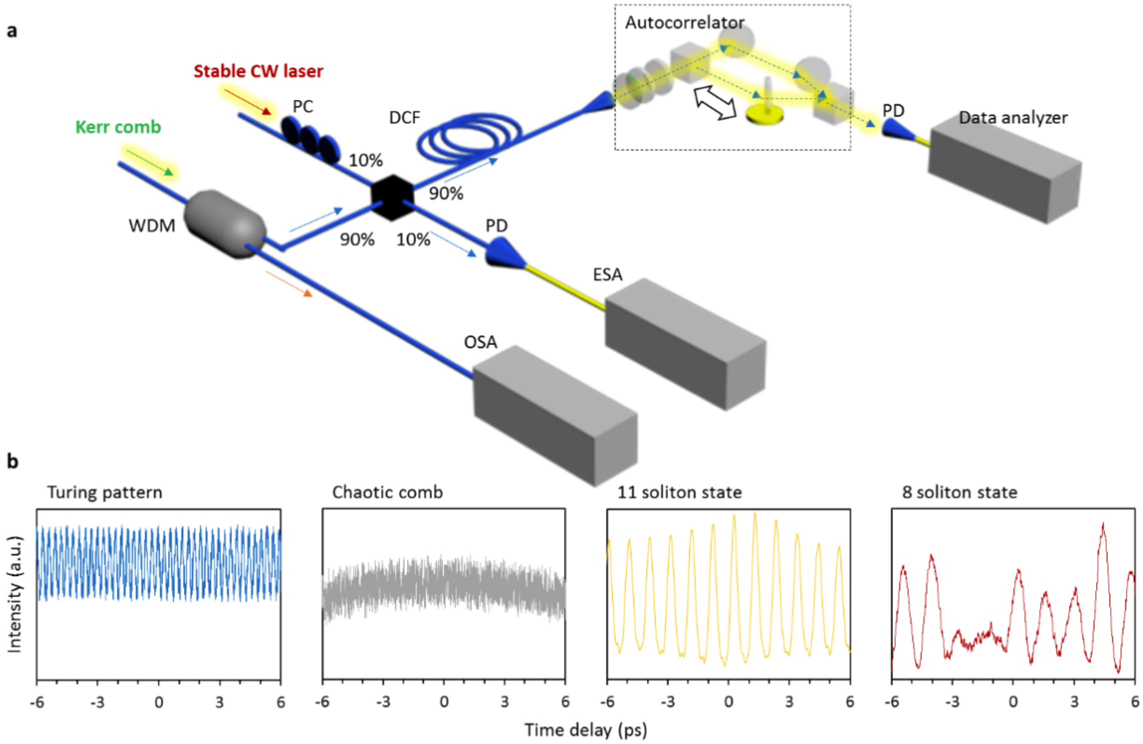

Figure B.12. a, Setup: PC: polarization controller. DCF: dispersion-compensated fiber. WDM: wavelength-division multiplexer. PD: photodetector; OSA: Optical spectrum analyzer; ESA: Electric spectrum analyzer. b,Measured AC trace samples: from left to right, Turing, high noise, 11 soliton crystal and 8 soliton crystal

B.3.4 Measurement of the dispersion instability due to the ion dielectric

Figure B.13a shows the schematic sectional view when gating the graphene heterostructure. The gate probe is close to the graphene (height < 1 μm) while far away from the nitride core (distance > 10 μm). Mode field distribution ratio around the probes is less than 10^{-4}(Figure B.4), hence the carriers in the gate probe can hardly influence the mode field. During the gate voltage tuning,the ions form an electric double layer (EDL) at the liquid/graphene interface with effective capacitance thickness $\approx$ 1 nm over graphene, as shown in Figure B.13b schematically. The modulation speed of this graphene-EDL heterostructure is determined by both the capacitance dynamics and ion diffusion. Stabilized by the TEC (around 323K), the capacitance response limit is under 1 MHz, which is influenced by the diffusion coefficient of the DEME-TSFI $10^{-10}\, m^2/s$ [156, 157]. Determined by the Fick's law, diffusion time of the ions equals $x^2/2D$ approximately, here D is the diffusion coefficient, *x* is the average distance of the ion diffusion. In the micrometer-scale heterostructure, for graphene modulation in range of 0.59 eV to 0.62 eV, diffusion time is hundreds of nanoseconds. Moreover, to verify the GVD modulation is induced mainly by graphene rather than ionic motion, we measured the GVD influenced by the ion-gel only. The setup is shown in Figure B.13c. Here a microfiber based Mach-Zehnder interferometer (MZI) is applied to check the GVD modification. The microfiber is embedded in the ion, but far away enough from the electrodes. The diameter of the microfiber is controlled as $\approx$ 3 μm, ensuring $\approx$ 8% mode field overlapping in the ion-gel, similar to our graphene based heterostructure. GVD of the MZI is optimized at $\approx$-47 fs^2/mm. By checking the FSR non-equidistance [155], we plot correlation of the gate voltage and the GVD, in Figure B.13d. GVD modification induced by the ion motion is measured to be two orders-of-magnitude smaller than in the graphene-SiN heterostructure.

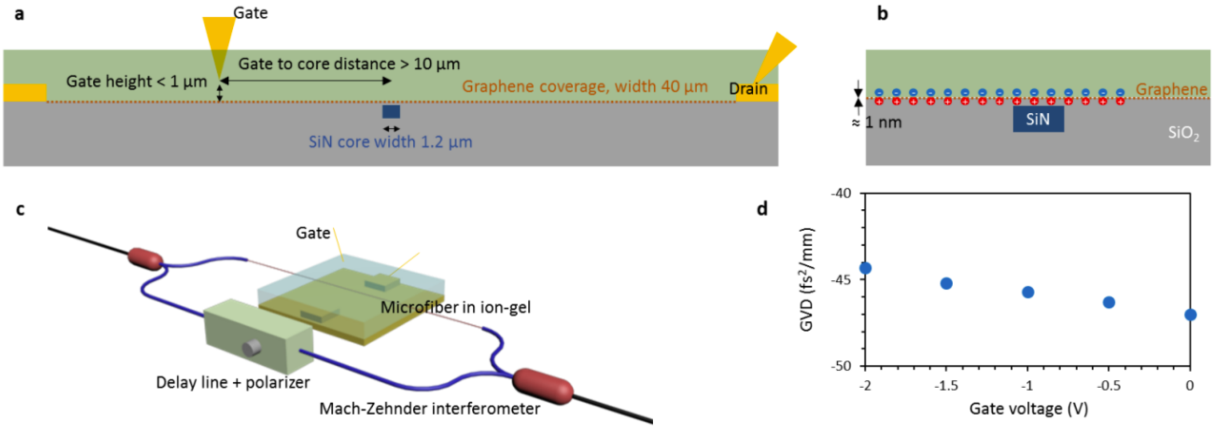

Figure B.13. a, Cross-sectional view of the heterogeneous graphene-nitride structure. b, Schematic diagram of the electric double layer on graphene/ion-gel interface. c, Mach-Zehnder setup for GVD measurement on the ion motion effects, without graphene. d, GVD modification induced by gating the ion-gel.

APPENDIX C

Ultrafast spectral analysis of breathers and chaos in frequency microcombs

C.1 Characteristics of the 17.9 GHz microresonator

Figure C.1A shows a cross-section scanning electron micrograph of the microresonator waveguide, with an estimated 82° to 88° slope of the vertical sidewalls. (Woollam M-2000 ellipsometer) and then fitted with the Sellmeier equation assuming a single absorption resonance in the ultraviolet. Figure C.1B shows the modeled free spectral range (FSR) of the first two TE modes of the microresonator. While the fundamental mode features a FSR of 17.9 GHz, the TE2 mode has a slightly lower FSR and thus the resonances of the TE2 family approaches that of the fundamental family about every 4 nm ($\frac{FSR^2}{\Delta FSR} = 460GHz$). The mode interaction when the resonances are close leads to local disruption of the phase matching condition. Figures C.1C and C.1D show the modeled group velocity dispersion (β_2, GVD) and third order dispersion (β_3, TOD).

C.2 Setup schematic of the 250-MHz parametric spectro-temporal analyzer

The experimental setup shown in Figure C.1 consists of two stages of four-wave mixing (FWM), labeled in yellow. In the first stage, the input or the SUT is mixed with a swept pump marked in the upper red box. The swept pump is generated by sending the output of a fiber-based femtosecond mode-locked laser (MLL; Menlo Systems) through a bandpass filter centered at 1556 nm with 1.5-nm bandwidth, and subsequently propagating the resulting signal through a carefully tuned length of dispersive fiber. In this experiment our dispersive fiber element consists of two spools of dispersion-compensating fiber (-1.35 ns/nm) and a spool of single-mode fiber (170 ps/nm). EDFA1 and EDFA2 are low-noise pre-amplifiers to compensate the losses in the fibers. The filter after EDFA2 suppresses the amplified spontaneous emission (ASE) noise and the filtered pulse is then amplified by a high-power EDFA to around 200 mW to generate the swept pump. Subsequently, the swept pump and input signal are combined by WDM3 and then launched together into a 50-m HNLF.

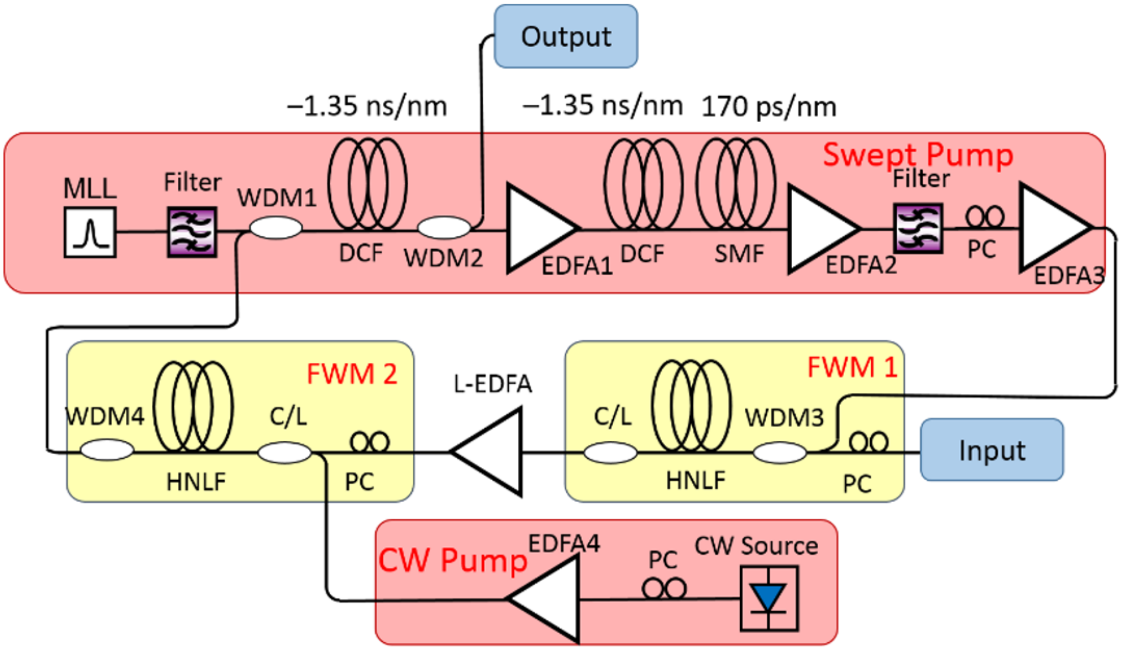

Figure C.1. PASTA is built on the principle of spatio-temporal duality, and replicates in the temporal domain, a *2f* spatial Fourier imaging system. In this architecture we use two FWM stages to write a linear chirp onto the SUT and then pass the output waveform to a dispersive fiber with GDD equaling half the pump GDD. Therefore at the output of this system we retrieve the Fourier transform of the SUT at a high frame rate. MLL, mode-locked fiber laser frequency comb that functions as the pump for the FWM process which writes a linear chirp onto the signal; DCF, dispersion compensating fiber; WDM, wavelength division multiplexer; SMF, single-mode fiber; EDFA, erbium-doped fiber amplifier; PC, polarization controller; HNLF, highly nonlinear fiber; C/L, C-band and L-band wavelength division multiplexer; CW, continuous wave; FWM, four-wave mixing.

The corresponding spectrum is shown in Figure C.2, where a continuous-wave (CW) signal at 1540 nm from a laser diode is used as an example. A secondary mode of the laser diode is not entirely suppressed, but it has no measurable influence on the system performance. As plotted in

Figure C.2, an idler twice as wide as the swept pump is generated around 1575 nm, which is then filtered out by the C/L band coupler. The filtered idler is amplified by a low-power L-band EDFA before being launched into the second stage of FWM, which is pumped by a CW laser generated from the lower red box in Figure C.1. A CW source centered at 1556 is amplified by EDFA4 to around 200 mW and then combined with the filtered idler from first stage-FWM through another C/L-band coupler. As shown in the FWM spectrum of the second stage in Figure C.2B, the idler from the first-stage FWM serves as the signal and is converted to the original wavelength range around 1540 nm. The converted idler from the second-stage FWM is then filtered out by WDM4 and is sent through the same spool of dispersion-compensating fiber (DCF) utilized in the swept-pump generation. The arrangement for the dispersive fibers employed in the system guarantees that the output group delay dispersion (GDD) is exactly one half of the pump GDD, so that the system functions as a temporal *2f* system. To achieve this, the spool of single-mode fiber (SMF) is used to compensate the deviation of pump GDD from ideal value owing to the dispersion slope of DCF. WDM1 and WDM2 are used to combine and separate the idler and the filtered femtosecond MLL. Finally, the output is extracted from WDM2 and is sent to a photodetector whose output is recorded by a high-speed real-time oscilloscope.

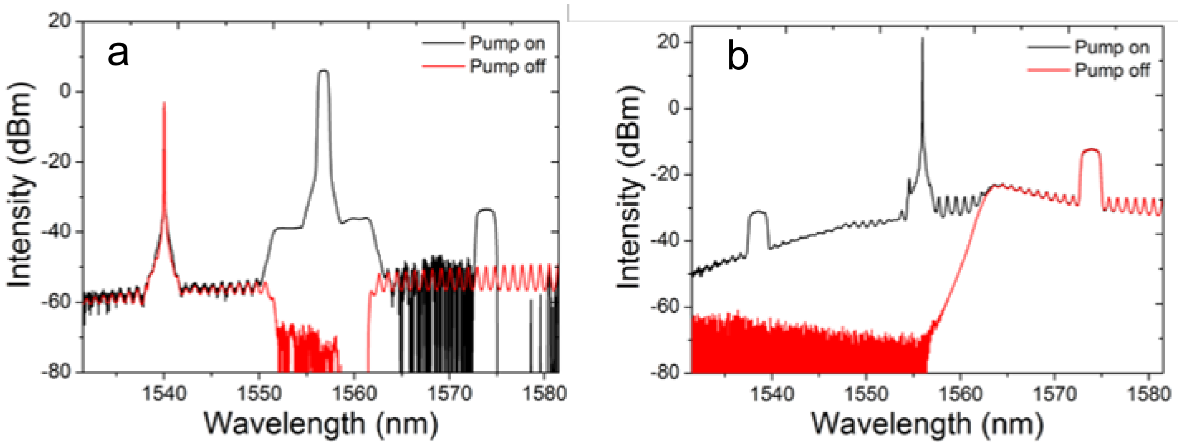

Figure C.2. (A) The filtered swept pump is around 1556 nm and is generated from a fs fiber mode-locked laser. The spectrum on the left around 1540 nm is the SUT, which in our case is a filtered spectral window from the microresonator frequency comb. As can be observed an idler twice as wide as the swept pump was generated around 1575 nm. This idler retains the signal spectral information with a linear chirp written onto it (derived from the swept pump). (B) The second stage of FWM is utilized in our architecture for convenience and ease of stability as the output from the second stage switches the sign of the chirp and facilitates the use of the same DCF used to chirp the swept pump. This reduces thermal effects in the system and also reduces the length of fiber necessary. Here the pump is a CW laser diode around 1556 nm and amplified to 200 mW. The output of stage 1 then mixes with the CW pump and an idler is generated around 1538 nm. The idler is then sent through a dispersive fiber and a high-speed PD to retrieve the Fourier transform of the original signal.

C.3 Characterization of the 250-MHz parametric spectro-temporal analyzer

To demonstrate the measurement range, the wavelength of the input signal was tuned from 1540 nm to 1545 nm and the corresponding temporal output waveform was recorded and shown in Figure C.3A. When the wavelength is shifted by 0.5 nm, the output pulse shifted by about 675 ps along the time axis, indicating a wavelength-to-time mapping ratio of about 1.35 ns/nm. The envelope of the pulse intensities across the measurement range reflects the spectral responsivity of the system, which is determined by the conversion efficiency in both stages of FWM and the gain spectra of the EDFAs involved. The intensities of the measured spectral components can be calibrated according to the spectral responsivity, if necessary [158, 159]. The zoom-in of the pulse shape at 1542 nm is shown in Figure C.3B as an example. The 3-dB pulsewidth is as narrow as 30 ps by using a 38-GHz photodetector and a 25-GHz oscilloscope. Therefore, the spectral resolution of the PASTA can be calculated to be 30 (ps) / 1.35 (ns/nm) = 22 pm.

In addition to the measurement range and spectral resolution, the temporal intensity stability of the system is also characterized. The femtosecond MLL used to generate the swept pump is repetition-rate stabilized at 250 MHz and therefore a femtosecond pulse is generated every 4 ns as shown in Figure C.4A. The corresponding peak intensity stability that took into account 10,000 periods is depicted by the histogram in Figure C.4B and the ratio between standard deviation to mean value (std/mean) of the Gaussian distribution is about 2%, which indicates very high stability of the femtosecond MLL. The frame rate of the PASTA system is in accordance with the femtosecond MLL. Therefore, when a single-wavelength CW signal is measured, PASTA would

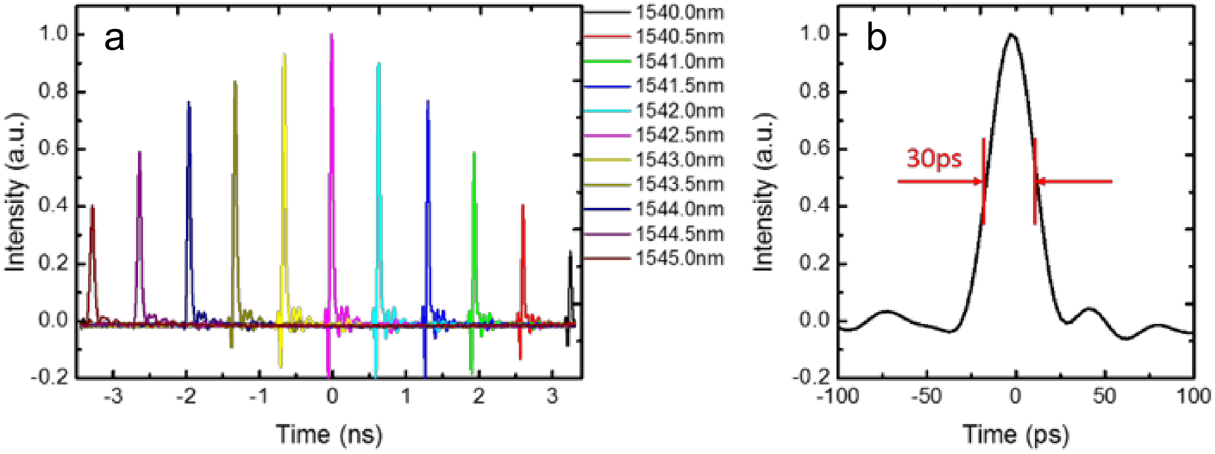

Figure C.3. (A) To demonstrate the measurement range, the wavelength of the input signal was tuned from 1540 nm to 1545 nm and the corresponding temporal responsivities for 11 different wavelengths is plotted. When the wavelength is shifted by 0.5 nm, the output pulse shifted by about 675 ps along the time axis, indicating a wavelength-to-time mapping ratio of about 1.35ns/nm. b, Impulse response at 1542 nm. The 3-dB pulsewidth is as narrow as 30 ps when using a 38-GHz photodetector and a 25-GHz oscilloscope. Therefore, the spectral resolution of the PASTA can be calculated as 30 (ps) / 1.35 (ns/nm) = 22 pm.

sample the signal at 250 MHz frame rate and output a short pulse in each frame, as shown in Figure C.4C. As observed in the corresponding peak intensity histogram generated from PASTA in Figure C.4D, the std/mean increased to 8.6%.

Neglecting the temporal intensity fluctuation of the CW signal, the degradation of the temporal stability of the final output compared to the femtosecond MLL can be mainly attributed to the signal-to-noise (SNR) degradation during repeated amplification and the FWM conversions. The std/mean value for measuring a CW signal represents the stability of the PASTA system and, at the same time, indicates the detection sensitivity in relation to spectral intensity fluctuation. More intuitively, the intensity fluctuation of the SUT can be directly observed from the waveform of the PASTA output as long as the fluctuation range is larger than 8.6%. Moreover, as it will be shown later, periodic fluctuations with even smaller intensities can also be revealed from the Fourier transform of the temporal waveform of the PASTA output.

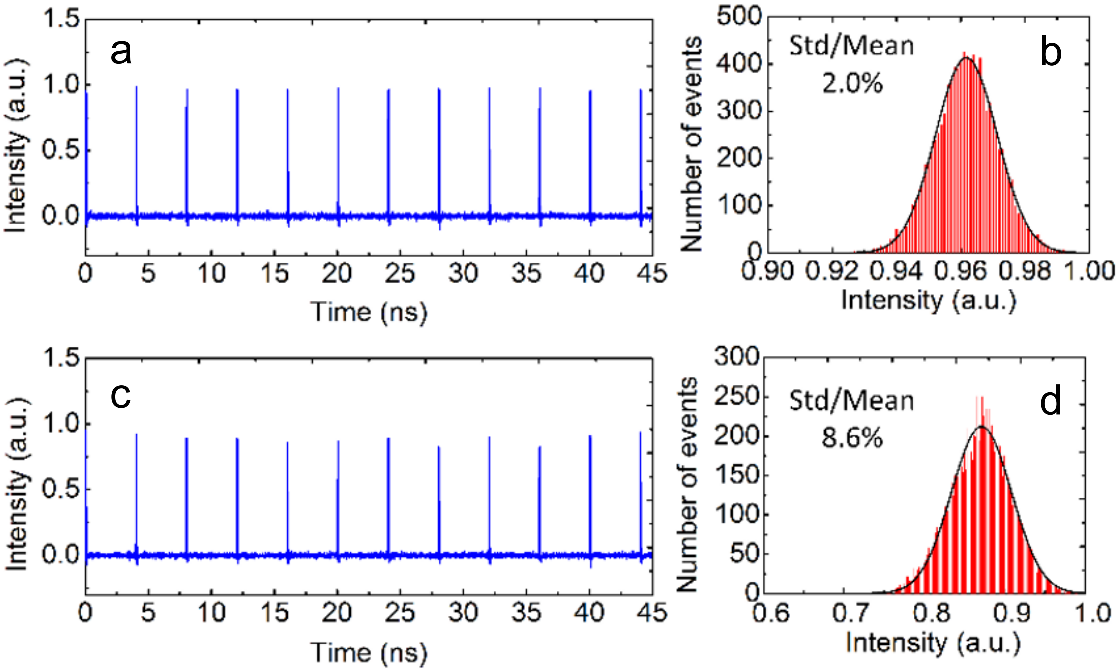

Figure C.4. (A) To demonstrate the measurement range, the wavelength of the input signal was tuned from 1540 nm to 1545 nm and the corresponding temporal responsivities for 11 different wavelengths is plotted. When the wavelength is shifted by 0.5 nm, the output pulse shifted by about 675 ps along the time axis, indicating a wavelength-to-time mapping ratio of about 1.35ns/nm. b, Impulse response at 1542 nm. The 3-dB pulsewidth is as narrow as 30 ps when using a 38-GHz photodetector and a 25-GHz oscilloscope. Therefore, the spectral resolution of the PASTA can be calculated as 30 (ps) / 1.35 (ns/nm) = 22 pm.

C.4 Signal processing of the pulse and wave extremes

To extract the local maxima of the pulses, the time series were first processed to filter out high-frequency oscillations. Figure C.5A presents a fast Fourier transform (FFT) spectrum of a sample real-time series. All frequency components above 1 GHz are removed from the spectrum, as shown in red. A zoomed in version of this spectrum is plotted in Figure C.5B. Figures C.5B and C.5C compare the raw time series with the signal obtained from an inverse Fourier transform of the filtered spectrum, showing that the shape of the pulses is preserved despite the low cutoff frequency of the filtering.

In order to study the pulses, a combination of wave and crest heights is used: the noise is represented by wave heights, hence the amplitude difference between a local maximum and its lowest neighboring local minimum [99,160,161]. The pulses are represented by their crest heights, defined as the amplitude of the highest maximum within a pulse above the mean value of the time trace. As discussed below, a stricter definition of crest heights, where all maxima within the pulses are taken into account, is discussed and yields a higher threshold for rogue waves without affecting the conclusions.

As pulses can contain several local maxima, two definitions of crest heights are possible: either considering only the largest maximum in a pulse, or all its local maxima. The first definition gives a simple representation of the pulses and describes accurately their amplitude. The second allows for a stricter identification of extreme events: considering the amplitude of all maxima within a pulse yields a larger significant height, thus a larger threshold for rogue waves and fewer rare events. This criterion will be referred to as maxima heights to distinguish it from the definition of crest heights given in the main text.

Figures C.6A and C.6B present the evolution of crest and maxima heights, respectively, as well as their corresponding thresholds for rogue wave. The horizontal dashed with lines show the value of the global threshold calculated for the whole time series, and the solid white lines show the evolution of the threshold within a 20 μs window. While maxima heights yield a larger global threshold of 0.45, instead of 0.35 for the crest heights, a large number of extreme events are still

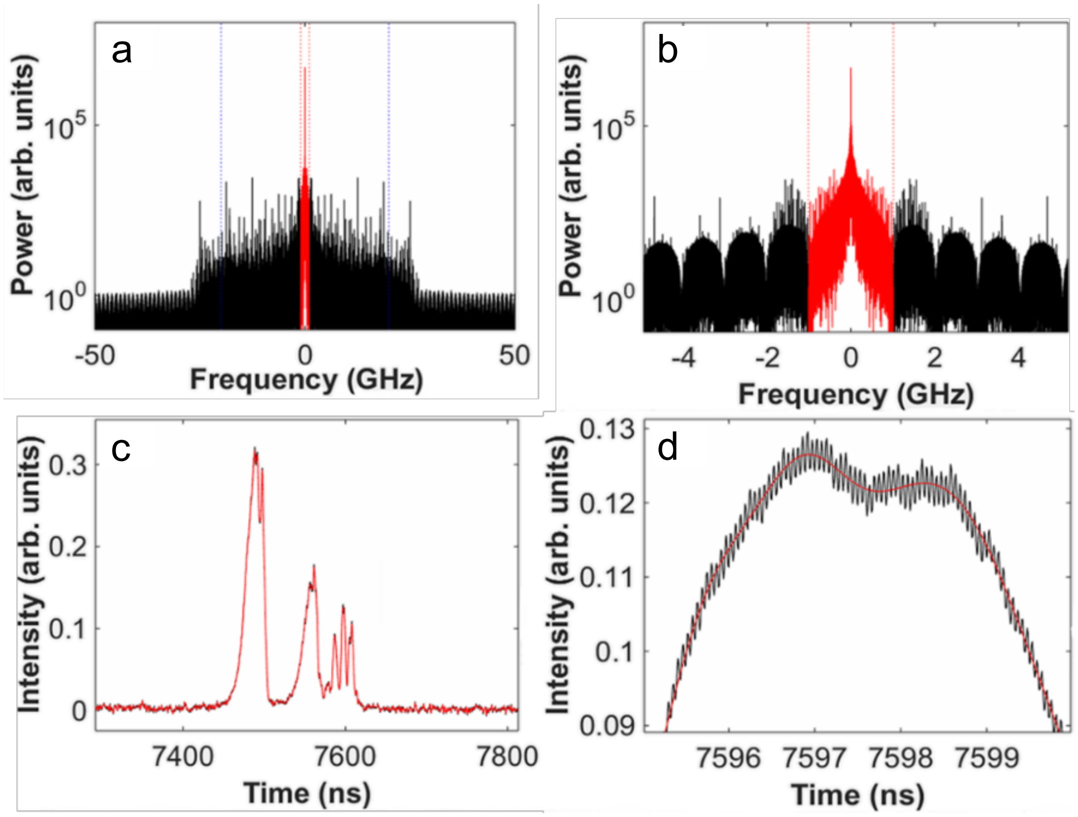

Figure C.5. (A) Fast Fourier transform (FFT) spectrum of the waveform (black) and the remaining spectrum after the filtering (red). (B) Zoom-in of the spectrum in panel A, only the frequency components marked in red are considered. (C) Example of the temporal waveform before (black) and after (red) the filtering. The significant overlap is expected as most of the power is concentrated in the low frequency modes. (D) Zoomed in temporal waveform before (in black) and after (in red) filtering.

found above this threshold. The evolution of both thresholds overs time is also rather similar as shown in Figure C.6C. The main difference is found around a time of 1.785 ms, where a large pulse similar to the one described in Figure 4.6F is observed. Considering only the amplitude of the peak of the pulse fails to represent accurately such a pulse, which should render the neighboring pulses less likely to be considered as rogue. When considering maxima heights, the threshold for rogue waves exhibits a sudden increase to up to 1.16 close to the middle of this event. As a consequence, pulses with maxima heights above 0.45 but below 1.16 should in fact not be considered as extreme events within the 20 μs window at this time, since they are shadowed by a much larger extreme event.

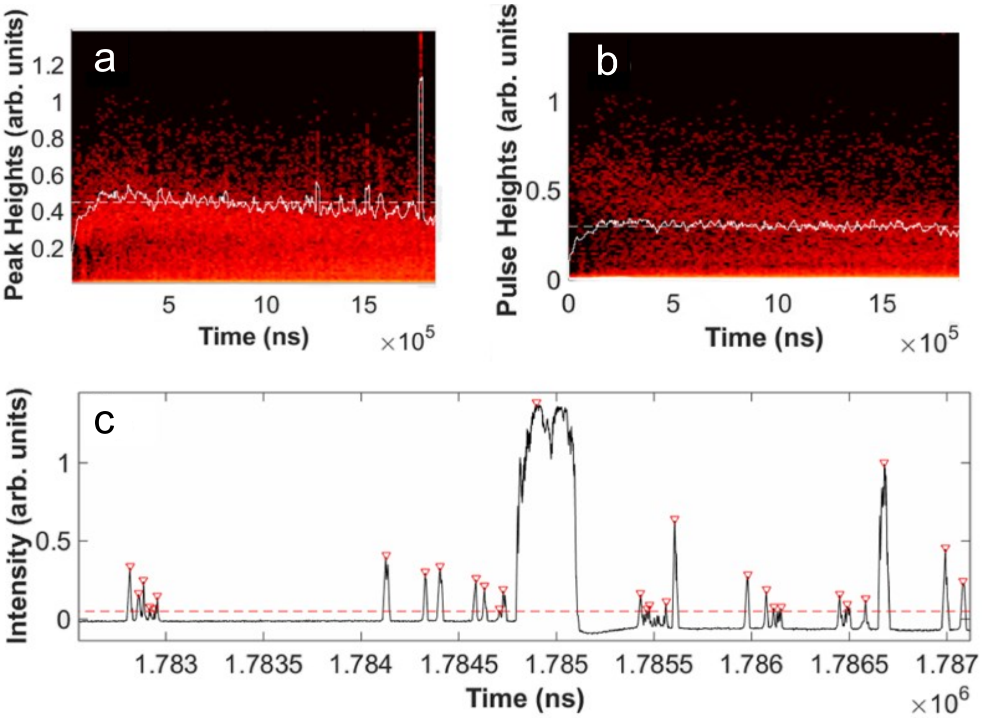

Figure C.6. (A) Rogue wave threshold evolution under the crest height approach. (B) Rogue wave threshold evolution under the maxima height approach. (C) Zoom-in of the temporal waveform at the position that induces the drastic difference between the two approaches.

REFERENCES

[1] T. Udem, R. Holzwarth, and T. W. Hänsch, "Optical frequency metrology," *Nature*, vol. 416, pp. 233–237, Mar. 2002. Number: 6877 Publisher: Nature Publishing Group.

[2] S. A. Diddams, J. C. Bergquist, S. R. Jefferts, and C. W. Oates, "Standards of Time and Frequency at the Outset of the 21st Century," *Science*, vol. 306, pp. 1318–1324, Nov. 2004. Publisher: American Association for the Advancement of Science Section: Special Reviews.

[3] B. Piglosiewicz, S. Schmidt, D. J. Park, J. Vogelsang, P. Groß, C. Manzoni, P. Farinello, G. Cerullo, and C. Lienau, "Carrier-envelope phase effects on the strong-field photoemission of electrons from metallic nanostructures," *Nature Photonics*, vol. 8, pp. 37–42, Jan. 2014. Number: 1 Publisher: Nature Publishing Group.

[4] F. Krausz and M. I. Stockman, "Attosecond metrology: from electron capture to future signal processing," *Nature Photonics*, vol. 8, pp. 205–213, Mar. 2014. Number: 3 Publisher: Nature Publishing Group.

[5] S. A. Diddams, D. J. Jones, J. Ye, S. T. Cundiff, J. L. Hall, J. K. Ranka, R. S. Windeler, R. Holzwarth, T. Udem, and T. W. Hänsch, "Direct Link between Microwave and Optical Frequencies with a 300 THz Femtosecond Laser Comb," *Physical Review Letters*, vol. 84, pp. 5102–5105, May 2000. Publisher: American Physical Society.

[6] A. Wirth, M. T. Hassan, I. Grguraš, J. Gagnon, A. Moulet, T. T. Luu, S. Pabst, R. Santra, Z. A. Alahmed, A. M. Azzeer, V. S. Yakovlev, V. Pervak, F. Krausz, and E. Goulielmakis, "Synthesized Light Transients," *Science*, vol. 334, pp. 195–200, Oct. 2011. Publisher: American Association for the Advancement of Science Section: Research Article.

[7] P. Del'Haye, O. Arcizet, A. Schliesser, R. Holzwarth, and T. J. Kippenberg, "Full Stabilization of a Microresonator-Based Optical Frequency Comb," *Physical Review Letters*, vol. 101, p. 053903, July 2008. Publisher: American Physical Society.

[8] J. Lim, S.-W. Huang, A. K. Vinod, P. Mortazavian, M. Yu, D.-L. Kwong, A. A. Savchenkov, A. B. Matsko, L. Maleki, and C. W. Wong, "Stabilized chip-scale Kerr frequency comb via a high-Q reference photonic microresonator," *Optics Letters*, vol. 41, pp. 3706–3709, Aug. 2016. Publisher: Optical Society of America.

[9] D. J. Jones, S. A. Diddams, J. K. Ranka, A. Stentz, R. S. Windeler, J. L. Hall, and S. T. Cundiff, "Carrier-Envelope Phase Control of Femtosecond Mode-Locked Lasers and Direct Optical Frequency Synthesis," *Science*, vol. 288, pp. 635–639, Apr. 2000. Publisher: American Association for the Advancement of Science Section: Research Article.

[10] J. Ye and S. T. Cundiff, eds., *Femtosecond Optical Frequency Comb: Principle, Operation and Applications*. Springer US, 2005.

[11] P. Del'Haye, A. Schliesser, O. Arcizet, T. Wilken, R. Holzwarth, and T. J. Kippenberg, "Optical frequency comb generation from a monolithic microresonator," *Nature*, vol. 450, pp. 1214–1217, Dec. 2007. Number: 7173 Publisher: Nature Publishing Group.

[12] J. Yang, S.-W. Huang, Z. Xie, M. Yu, D.-L. Kwong, and C. W. Wong, "Coherent satellites in multispectral regenerative frequency microcombs," *Communications Physics*, vol. 3, pp. 1–9, Jan. 2020. Number: 1 Publisher: Nature Publishing Group.

[13] T. Herr, K. Hartinger, J. Riemensberger, C. Y. Wang, E. Gavartin, R. Holzwarth, M. L. Gorodetsky, and T. J. Kippenberg, "Universal formation dynamics and noise of Kerr-frequency combs in microresonators," *Nature Photonics*, vol. 6, pp. 480–487, July 2012. Number: 7 Publisher: Nature Publishing Group.

[14] S. B. Papp, P. Del'Haye, and S. A. Diddams, "Parametric seeding of a microresonator optical frequency comb," *Optics Express*, vol. 21, pp. 17615–17624, July 2013. Publisher: Optical Society of America.

[15] P. Del'Haye, S. B. Papp, and S. A. Diddams, "Hybrid Electro-Optically Modulated Microcombs," *Physical Review Letters*, vol. 109, p. 263901, Dec. 2012. Publisher: American Physical Society.

[16] P. Del'Haye, K. Beha, S. B. Papp, and S. A. Diddams, "Self-Injection Locking and Phase-Locked States in Microresonator-Based Optical Frequency Combs," *Physical Review Letters*, vol. 112, p. 043905, Jan. 2014. Publisher: American Physical Society.

[17] D. J. Moss, R. Morandotti, A. L. Gaeta, and M. Lipson, "New CMOS-compatible platforms based on silicon nitride and Hydex for nonlinear optics," *Nature Photonics*, vol. 7, pp. 597–607, Aug. 2013. Number: 8 Publisher: Nature Publishing Group.

[18] K. Saha, Y. Okawachi, B. Shim, J. S. Levy, R. Salem, A. R. Johnson, M. A. Foster, M. R. E. Lamont, M. Lipson, and A. L. Gaeta, "Modelocking and femtosecond pulse generation in chip-based frequency combs," *Optics Express*, vol. 21, pp. 1335–1343, Jan. 2013. Publisher: Optical Society of America.

[19] S. B. Papp, K. Beha, P. Del'Haye, F. Quinlan, H. Lee, K. J. Vahala, and S. A. Diddams, "Microresonator frequency comb optical clock," *Optica*, vol. 1, pp. 10–14, July 2014. Publisher: Optical Society of America.

[20] T. Herr, V. Brasch, J. D. Jost, C. Y. Wang, N. M. Kondratiev, M. L. Gorodetsky, and T. J. Kippenberg, "Temporal solitons in optical microresonators," *Nature Photonics*, vol. 8, pp. 145–152, Feb. 2014. Number: 2 Publisher: Nature Publishing Group.

[21] S.-W. Huang, H. Zhou, J. Yang, J. McMillan, A. Matsko, M. Yu, D.-L. Kwong, L. Maleki, and C. Wong, "Mode-Locked Ultrashort Pulse Generation from On-Chip Normal Dispersion Microresonators," *Physical Review Letters*, vol. 114, p. 053901, Feb. 2015. Publisher: American Physical Society.

[22] S.-W. Huang, A. K. Vinod, J. Yang, M. Yu, D.-L. Kwong, and C. W. Wong, "Quasi-phase-matched multispectral Kerr frequency comb," *Optics Letters*, vol. 42, pp. 2110–2113, June 2017. Publisher: Optical Society of America.

[23] Y.-S. Jang, H. Liu, J. Yang, M. Yu, D.-L. Kwong, and C. W. Wong, "Nanometric Precision Distance Metrology via Hybrid Spectrally Resolved and Homodyne Interferometry in a Single Soliton Frequency Microcomb," *Physical Review Letters*, vol. 126, p. 023903, Jan. 2021. Publisher: American Physical Society.

[24] Y. Li, S.-W. Huang, B. Li, H. Liu, J. Yang, A. K. Vinod, K. Wang, M. Yu, D.-L. Kwong, H.-T. Wang, K. K.-Y. Wong, and C. W. Wong, "Real-time transition dynamics and stability of chip-scale dispersion-managed frequency microcombs," *Light: Science & Applications*, vol. 9, p. 52, Apr. 2020. Number: 1 Publisher: Nature Publishing Group.

[25] X. Xue, Y. Xuan, Y. Liu, P.-H. Wang, S. Chen, J. Wang, D. E. Leaird, M. Qi, and A. M. Weiner, "Mode-locked dark pulse Kerr combs in normal-dispersion microresonators," *Nature Photonics*, vol. 9, pp. 594–600, Sept. 2015. Number: 9 Publisher: Nature Publishing Group.

[26] S.-W. Huang, J. Yang, J. Lim, H. Zhou, M. Yu, D.-L. Kwong, and C. W. Wong, "A low-phase-noise 18 GHz Kerr frequency microcomb phase-locked over 65 THz," *Scientific Reports*, vol. 5, p. 13355, Aug. 2015. Number: 1 Publisher: Nature Publishing Group.

[27] D. T. Spencer, T. Drake, T. C. Briles, J. Stone, L. C. Sinclair, C. Fredrick, Q. Li, D. Westly, B. R. Ilic, A. Bluestone, N. Volet, T. Komljenovic, L. Chang, S. H. Lee, D. Y. Oh, M.-G. Suh, K. Y. Yang, M. H. P. Pfeiffer, T. J. Kippenberg, E. Norberg, L. Theogarajan, K. Vahala, N. R. Newbury, K. Srinivasan, J. E. Bowers, S. A. Diddams, and S. B. Papp, "An optical-frequency synthesizer using integrated photonics," *Nature*, vol. 557, pp. 81–85, May 2018. Number: 7703 Publisher: Nature Publishing Group.

[28] V. Brasch, M. Geiselmann, T. Herr, G. Lihachev, M. H. P. Pfeiffer, M. L. Gorodetsky, and T. J. Kippenberg, "Photonic chip–based optical frequency comb using soliton Cherenkov radiation," *Science*, vol. 351, pp. 357–360, Jan. 2016. Publisher: American Association for the Advancement of Science Section: Report.

[29] S.-W. Huang, J. Yang, M. Yu, B. H. McGuyer, D.-L. Kwong, T. Zelevinsky, and C. W. Wong, "A broadband chip-scale optical frequency synthesizer at 2.7 × 10-16 relative uncertainty," *Science Advances*, vol. 2, p. e1501489, Apr. 2016. Publisher: American Association for the Advancement of Science Section: Research Article.

[30] V. Brasch, E. Lucas, J. D. Jost, M. Geiselmann, and T. J. Kippenberg, "Self-referenced photonic chip soliton Kerr frequency comb," *Light: Science & Applications*, vol. 6, pp. e16202–e16202, Jan. 2017. Number: 1 Publisher: Nature Publishing Group.

[31] C. Zhang, C.-K. Huang, K. A. Marsh, C. E. Clayton, W. B. Mori, and C. Joshi, "Ultrafast optical field–ionized gases—A laboratory platform for studying kinetic plasma instabilities," *Science Advances*, vol. 5, p. eaax4545, Sept. 2019. Publisher: American Association for the Advancement of Science Section: Research Article.

[32] Q. Li, T. C. Briles, D. A. Westly, T. E. Drake, J. R. Stone, B. R. Ilic, S. A. Diddams, S. B. Papp, and K. Srinivasan, "Stably accessing octave-spanning microresonator frequency combs in the soliton regime," *Optica*, vol. 4, pp. 193–203, Feb. 2017. Publisher: Optical Society of America.

[33] B. Stern, X. Ji, Y. Okawachi, A. L. Gaeta, and M. Lipson, "Battery-operated integrated frequency comb generator," *Nature*, vol. 562, pp. 401–405, Oct. 2018. Number: 7727 Publisher: Nature Publishing Group.

[34] H. Zhou, Y. Geng, W. Cui, S.-W. Huang, Q. Zhou, K. Qiu, and C. Wei Wong, "Soliton bursts and deterministic dissipative Kerr soliton generation in auxiliary-assisted microcavities," *Light: Science & Applications*, vol. 8, p. 50, May 2019. Number: 1 Publisher: Nature Publishing Group.

[35] B. Yao, S.-W. Huang, Y. Liu, A. K. Vinod, C. Choi, M. Hoff, Y. Li, M. Yu, Z. Feng, D.-L. Kwong, Y. Huang, Y. Rao, X. Duan, and C. W. Wong, "Gate-tunable frequency combs in graphene–nitride microresonators," *Nature*, vol. 558, pp. 410–414, June 2018. Number: 7710 Publisher: Nature Publishing Group.

[36] C. Bao, L. Zhang, A. Matsko, Y. Yan, Z. Zhao, G. Xie, A. M. Agarwal, L. C. Kimerling, J. Michel, L. Maleki, and A. E. Willner, "Nonlinear conversion efficiency in Kerr frequency comb generation," *Optics Letters*, vol. 39, pp. 6126–6129, Nov. 2014. Publisher: Optical Society of America.

[37] T. Ideguchi, S. Holzner, B. Bernhardt, G. Guelachvili, N. Picqué, and T. W. Hänsch, "Coherent Raman spectro-imaging with laser frequency combs," *Nature*, vol. 502, pp. 355–358, Oct. 2013. Number: 7471 Publisher: Nature Publishing Group.

[38] S. T. Cundiff and A. M. Weiner, "Optical arbitrary waveform generation," *Nature Photonics*, vol. 4, pp. 760–766, Nov. 2010. Number: 11 Publisher: Nature Publishing Group.

[39] P. Marin-Palomo, J. N. Kemal, M. Karpov, A. Kordts, J. Pfeifle, M. H. P. Pfeiffer, P. Trocha, S. Wolf, V. Brasch, M. H. Anderson, R. Rosenberger, K. Vijayan, W. Freude, T. J. Kippenberg, and C. Koos, "Microresonator-based solitons for massively parallel coherent optical communications," *Nature*, vol. 546, pp. 274–279, June 2017. Number: 7657 Publisher: Nature Publishing Group.

[40] Y. Geng, X. Huang, W. Cui, Y. Ling, B. Xu, J. Zhang, X. Yi, B. Wu, S.-W. Huang, K. Qiu, C. W. Wong, and H. Zhou, "Terabit optical OFDM superchannel transmission via coherent carriers of a hybrid chip-scale soliton frequency comb," *Optics Letters*, vol. 43, pp. 2406–2409, May 2018. Publisher: Optical Society of America.

[41] C.-H. Li, A. J. Benedick, P. Fendel, A. G. Glenday, F. X. Kärtner, D. F. Phillips, D. Sasselov, A. Szentgyorgyi, and R. L. Walsworth, "A laser frequency comb that enables radial velocity measurements with a precision of 1 cm s -1," *Nature*, vol. 452, pp. 610–612, Apr. 2008. Number: 7187 Publisher: Nature Publishing Group.

[42] E. Obrzud, M. Rainer, A. Harutyunyan, M. H. Anderson, J. Liu, M. Geiselmann, B. Chazelas, S. Kundermann, S. Lecomte, M. Cecconi, A. Ghedina, E. Molinari, F. Pepe, F. Wildi, F. Bouchy, T. J. Kippenberg, and T. Herr, "A microphotonic astrocomb," *Nature Photonics*, vol. 13, pp. 31–35, Jan. 2019. Number: 1 Publisher: Nature Publishing Group.

[43] M.-G. Suh, X. Yi, Y.-H. Lai, S. Leifer, I. S. Grudinin, G. Vasisht, E. C. Martin, M. P. Fitzgerald, G. Doppmann, J. Wang, D. Mawet, S. B. Papp, S. A. Diddams, C. Beichman, and K. Vahala, "Searching for exoplanets using a microresonator astrocomb," *Nature Photonics*, vol. 13, pp. 25–30, Jan. 2019. Number: 1 Publisher: Nature Publishing Group.

[44] T. C. Briles, J. R. Stone, T. E. Drake, D. T. Spencer, C. Fredrick, Q. Li, D. Westly, B. R. Ilic, K. Srinivasan, S. A. Diddams, and S. B. Papp, "Interlocking Kerr-microresonator frequency combs for microwave to optical synthesis," *Optics Letters*, vol. 43, pp. 2933–2936, June 2018. Publisher: Optical Society of America.

[45] N. Kuse, T. C. Briles, S. B. Papp, and M. E. Fermann, "Control of Kerr-microresonator optical frequency comb by a dual-parallel Mach-Zehnder interferometer," *Optics Express*, vol. 27, pp. 3873–3883, Feb. 2019. Publisher: Optical Society of America.

[46] T. E. Drake, T. C. Briles, J. R. Stone, D. T. Spencer, D. R. Carlson, D. D. Hickstein, Q. Li, D. Westly, K. Srinivasan, S. A. Diddams, and S. B. Papp, "Terahertz-Rate Kerr-Microresonator Optical Clockwork," *Physical Review X*, vol. 9, p. 031023, Aug. 2019. Publisher: American Physical Society.

[47] M. T. Hummon, S. Kang, D. G. Bopp, Q. Li, D. A. Westly, S. Kim, C. Fredrick, S. A. Diddams, K. Srinivasan, V. Aksyuk, and J. E. Kitching, "Photonic chip for laser stabilization to an atomic vapor with $10^{\&\#x2212;11}$ instability," *Optica*, vol. 5, pp. 443–449, Apr. 2018. Publisher: Optical Society of America.

[48] L. Stern, J. R. Stone, S. Kang, D. C. Cole, M.-G. Suh, C. Fredrick, Z. Newman, K. Vahala, J. Kitching, S. A. Diddams, and S. B. Papp, "Direct Kerr frequency comb atomic spectroscopy and stabilization," *Science Advances*, vol. 6, p. eaax6230, Feb. 2020. Publisher: American Association for the Advancement of Science Section: Research Article.

[49] A. Coillet, Z. Qi, I. V. Balakireva, G. Lin, C. R. Menyuk, and Y. K. Chembo, "On the transition to secondary Kerr combs in whispering-gallery mode resonators," *Optics Letters*, vol. 44, pp. 3078–3081, June 2019. Publisher: Optical Society of America.

[50] A. Kumar, S. Huang, J. Yang, M. Yu, D. Kwong, and C. W. Wong, "Internally phase stabilized Kerr frequency comb," in *2017 Conference on Lasers and Electro-Optics (CLEO)*, pp. 1–2, May 2017.

[51] S. Coen and M. Haelterman, "Modulational Instability Induced by Cavity Boundary Conditions in a Normally Dispersive Optical Fiber," *Physical Review Letters*, vol. 79, pp. 4139–4142, Nov. 1997. Publisher: American Physical Society.

[52] L. Lugiato, F. Prati, and M. Brambilla, *Nonlinear Optical Systems*. Cambridge: Cambridge University Press, 2015.

[53] T. Hansson and S. Wabnitz, "Dynamics of microresonator frequency comb generation: models and stability," *Nanophotonics*, vol. 5, pp. 231–243, June 2016. Publisher: De Gruyter Open Section: Nanophotonics.

[54] J. R. Stone, T. C. Briles, T. E. Drake, D. T. Spencer, D. R. Carlson, S. A. Diddams, and S. B. Papp, "Thermal and Nonlinear Dissipative-Soliton Dynamics in Kerr-Microresonator Frequency Combs," *Physical Review Letters*, vol. 121, p. 063902, Aug. 2018.

[55] Y. Liu, Y. Xuan, X. Xue, P.-H. Wang, S. Chen, A. J. Metcalf, J. Wang, D. E. Leaird, M. Qi, and A. M. Weiner, "Investigation of mode coupling in normal-dispersion silicon nitride microresonators for Kerr frequency comb generation," *Optica*, vol. 1, pp. 137–144, Sept. 2014. Publisher: Optical Society of America.

[56] S.-W. Huang, H. Liu, J. Yang, M. Yu, D.-L. Kwong, and C. W. Wong, "Smooth and flat phase-locked Kerr frequency comb generation by higher order mode suppression," *Scientific Reports*, vol. 6, p. 26255, May 2016. Number: 1 Publisher: Nature Publishing Group.

[57] A. S. Raja, A. S. Voloshin, H. Guo, S. E. Agafonova, J. Liu, A. S. Gorodnitskiy, M. Karpov, N. G. Pavlov, E. Lucas, R. R. Galiev, A. E. Shitikov, J. D. Jost, M. L. Gorodetsky, and T. J. Kippenberg, "Electrically pumped photonic integrated soliton microcomb," *Nature Communications*, vol. 10, p. 680, Feb. 2019. Number: 1 Publisher: Nature Publishing Group.

[58] A. S. Raja, A. S. Raja, J. Liu, J. Liu, N. Volet, N. Volet, R. N. Wang, J. He, E. Lucas, R. Bouchandand, P. Morton, J. Bowers, and T. J. Kippenberg, "Chip-based soliton microcomb module using a hybrid semiconductor laser," *Optics Express*, vol. 28, pp. 2714–2721, Feb. 2020. Publisher: Optical Society of America.

[59] Y. K. Chembo, "Kerr optical frequency combs: theory, applications and perspectives," *Nanophotonics*, vol. 5, pp. 214–230, June 2016. Publisher: De Gruyter Open Section: Nanophotonics.

[60] A. Pasquazi, M. Peccianti, L. Razzari, D. J. Moss, S. Coen, M. Erkintalo, Y. K. Chembo, T. Hansson, S. Wabnitz, P. Del'Haye, X. Xue, A. M. Weiner, and R. Morandotti, "Microcombs: A novel generation of optical sources," *Physics Reports*, vol. 729, pp. 1–81, Jan. 2018.

[61] J. Alnis, A. Schliesser, C. Y. Wang, J. Hofer, T. J. Kippenberg, and T. W. Hänsch, "Thermal-noise-limited crystalline whispering-gallery-mode resonator for laser stabilization," *Physical Review A*, vol. 84, p. 011804, July 2011. Publisher: American Physical Society.

[62] T. M. Fortier, M. S. Kirchner, F. Quinlan, J. Taylor, J. C. Bergquist, T. Rosenband, N. Lemke, A. Ludlow, Y. Jiang, C. W. Oates, and S. A. Diddams, "Generation of ultrastable microwaves via optical frequency division," *Nature Photonics*, vol. 5, pp. 425–429, July 2011. Number: 7 Publisher: Nature Publishing Group.

[63] J. Millo, M. Abgrall, M. Lours, E. M. L. English, H. Jiang, J. Guéna, A. Clairon, M. E. Tobar, S. Bize, Y. Le Coq, and G. Santarelli, "Ultralow noise microwave generation with fiber-based optical frequency comb and application to atomic fountain clock," *Applied Physics Letters*, vol. 94, p. 141105, Apr. 2009. Publisher: American Institute of Physics.

[64] A. Bartels, S. A. Diddams, C. W. Oates, G. Wilpers, J. C. Bergquist, W. H. Oskay, and L. Hollberg, "Femtosecond-laser-based synthesis of ultrastable microwave signals from optical frequency references," *Optics Letters*, vol. 30, pp. 667–669, Mar. 2005. Publisher: Optical Society of America.

[65] J. J. McFerran, E. N. Ivanov, A. Bartels, G. Wilpers, C. W. Oates, S. A. Diddams, and L. Hollberg, "Low-noise synthesis of microwave signals from an optical source," *Electronics Letters*, vol. 41, pp. 650–651, May 2005. Publisher: IET Digital Library.

[66] A. K. Vinod, S. W. Huang, J. Yang, M. Yu, D.-L. Kwong, and C. W. Wong, "Optical Clocks via Breather Stabilization in Chip-Scale Frequency Combs," in *2019 Conference on Lasers and Electro-Optics (CLEO)*, pp. 1–2, May 2019. ISSN: 2160-8989.

[67] G. Moille, X. Lu, A. Rao, Q. Li, D. A. Westly, L. Ranzani, S. B. Papp, M. Soltani, and K. Srinivasan, "Kerr-Microresonator Soliton Frequency Combs at Cryogenic Temperatures," *Physical Review Applied*, vol. 12, p. 034057, Sept. 2019. Publisher: American Physical Society.

[68] Q.-F. Yang, X. Yi, K. Y. Yang, and K. Vahala, "Stokes solitons in optical microcavities," *Nature Physics*, vol. 13, pp. 53–57, Jan. 2017. Number: 1 Publisher: Nature Publishing Group.

[69] P. Del'Haye, A. Coillet, T. Fortier, K. Beha, D. C. Cole, K. Y. Yang, H. Lee, K. J. Vahala, S. B. Papp, and S. A. Diddams, "Phase-coherent microwave-to-optical link with a self-referenced microcomb," *Nature Photonics*, vol. 10, pp. 516–520, Aug. 2016. Number: 8 Publisher: Nature Publishing Group.

[70] F. Wang, Y. Zhang, C. Tian, C. Girit, A. Zettl, M. Crommie, and Y. R. Shen, "Gate-Variable Optical Transitions in Graphene," *Science*, vol. 320, pp. 206–209, Apr. 2008. Publisher: American Association for the Advancement of Science Section: Report.

[71] Z. Q. Li, E. A. Henriksen, Z. Jiang, Z. Hao, M. C. Martin, P. Kim, H. L. Stormer, and D. N. Basov, "Dirac charge dynamics in graphene by infrared spectroscopy," *Nature Physics*, vol. 4, pp. 532–535, July 2008. Number: 7 Publisher: Nature Publishing Group.

[72] F. Bonaccorso, Z. Sun, T. Hasan, and A. C. Ferrari, "Graphene photonics and optoelectronics," *Nature Photonics*, vol. 4, pp. 611–622, Sept. 2010. Number: 9 Publisher: Nature Publishing Group.

[73] A. Vakil and N. Engheta, "Transformation Optics Using Graphene," *Science*, vol. 332, pp. 1291–1294, June 2011. Publisher: American Association for the Advancement of Science Section: Report.

[74] T. Gu, N. Petrone, J. F. McMillan, A. van der Zande, M. Yu, G. Q. Lo, D. L. Kwong, J. Hone, and C. W. Wong, “Regenerative oscillation and four-wave mixing in graphene optoelectronics,” *Nature Photonics*, vol. 6, pp. 554–559, Aug. 2012. Number: 8 Publisher: Nature Publishing Group.

[75] M. Liu, X. Yin, E. Ulin-Avila, B. Geng, T. Zentgraf, L. Ju, F. Wang, and X. Zhang, “A graphene-based broadband optical modulator,” *Nature*, vol. 474, pp. 64–67, June 2011. Number: 7349 Publisher: Nature Publishing Group.

[76] C. T. Phare, Y.-H. Daniel Lee, J. Cardenas, and M. Lipson, “Graphene electro-optic modulator with 30 GHz bandwidth,” *Nature Photonics*, vol. 9, pp. 511–514, Aug. 2015. Number: 8 Publisher: Nature Publishing Group.

[77] F. H. L. Koppens, T. Mueller, P. Avouris, A. C. Ferrari, M. S. Vitiello, and M. Polini, “Photodetectors based on graphene, other two-dimensional materials and hybrid systems,” *Nature Nanotechnology*, vol. 9, pp. 780–793, Oct. 2014. Number: 10 Publisher: Nature Publishing Group.

[78] A. N. Grigorenko, M. Polini, and K. S. Novoselov, “Graphene plasmonics,” *Nature Photonics*, vol. 6, pp. 749–758, Nov. 2012. Number: 11 Publisher: Nature Publishing Group.

[79] S. Chakraborty, O. P. Marshall, T. G. Folland, Y.-J. Kim, A. N. Grigorenko, and K. S. Novoselov, “Gain modulation by graphene plasmons in aperiodic lattice lasers,” *Science*, vol. 351, pp. 246–248, Jan. 2016. Publisher: American Association for the Advancement of Science Section: Report.

[80] Y. Xu, Z. Lin, X. Zhong, X. Huang, N. O. Weiss, Y. Huang, and X. Duan, “Holey graphene frameworks for highly efficient capacitive energy storage,” *Nature Communications*, vol. 5, p. 4554, Aug. 2014. Number: 1 Publisher: Nature Publishing Group.

[81] A. Das, S. Pisana, B. Chakraborty, S. Piscanec, S. K. Saha, U. V. Waghmare, K. S. Novoselov, H. R. Krishnamurthy, A. K. Geim, A. C. Ferrari, and A. K. Sood, “Monitoring dopants by Raman scattering in an electrochemically top-gated graphene transistor,” *Nature Nanotechnology*, vol. 3, pp. 210–215, Apr. 2008. Number: 4 Publisher: Nature Publishing Group.

[82] C. Javerzac-Galy, A. Kumar, R. D. Schilling, N. Piro, S. Khorasani, M. Barbone, I. Goykhman, J. B. Khurgin, A. C. Ferrari, and T. J. Kippenberg, “Excitonic Emission of Monolayer Semiconductors Near-Field Coupled to High-Q Microresonators,” *Nano Letters*, vol. 18, pp. 3138–3146, May 2018. Publisher: American Chemical Society.

[83] V. Sorianello, M. Midrio, G. Contestabile, I. Asselberghs, J. Van Campenhout, C. Huyghebaert, I. Goykhman, A. K. Ott, A. C. Ferrari, and M. Romagnoli, “Graphene–silicon phase modulators with gigahertz bandwidth,” *Nature Photonics*, vol. 12, pp. 40–44, Jan. 2018. Number: 1 Publisher: Nature Publishing Group.

[84] S.-W. Huang, J. Yang, S.-H. Yang, M. Yu, D.-L. Kwong, T. Zelevinsky, M. Jarrahi, and C. W. Wong, "Globally Stable Microresonator Turing Pattern Formation for Coherent High-Power THz Radiation On-Chip," *Physical Review X*, vol. 7, p. 041002, Oct. 2017. Publisher: American Physical Society.

[85] D. C. Cole, E. S. Lamb, P. Del'Haye, S. A. Diddams, and S. B. Papp, "Soliton crystals in Kerr resonators," *Nature Photonics*, vol. 11, pp. 671–676, Oct. 2017. Number: 10 Publisher: Nature Publishing Group.

[86] M. T. Pearce, A. Agarwala, and D. S. Fisher, "Stabilization of extensive fine-scale diversity by ecologically driven spatiotemporal chaos," *Proceedings of the National Academy of Sciences*, vol. 117, pp. 14572–14583, June 2020. Publisher: National Academy of Sciences Section: Biological Sciences.

[87] J. Halatek and E. Frey, "Rethinking pattern formation in reaction–diffusion systems," *Nature Physics*, vol. 14, pp. 507–514, May 2018. Number: 5 Publisher: Nature Publishing Group.

[88] V. Bratanov, F. Jenko, and E. Frey, "New class of turbulence in active fluids," *Proceedings of the National Academy of Sciences*, vol. 112, pp. 15048–15053, Dec. 2015. Publisher: National Academy of Sciences Section: Physical Sciences.

[89] K. E. Strecker, G. B. Partridge, A. G. Truscott, and R. G. Hulet, "Formation and propagation of matter-wave soliton trains," *Nature*, vol. 417, pp. 150–153, May 2002. Number: 6885 Publisher: Nature Publishing Group.

[90] Y. S. Kivshar and M. Peyrard, "Modulational instabilities in discrete lattices," *Physical Review A*, vol. 46, pp. 3198–3205, Sept. 1992. Publisher: American Physical Society.

[91] C. Sun, S. Jia, C. Barsi, S. Rica, A. Picozzi, and J. W. Fleischer, "Observation of the kinetic condensation of classical waves," *Nature Physics*, vol. 8, pp. 470–474, June 2012. Number: 6 Publisher: Nature Publishing Group.

[92] B. W. J. McNeil and N. R. Thompson, "X-ray free-electron lasers," *Nature Photonics*, vol. 4, pp. 814–821, Dec. 2010. Number: 12 Publisher: Nature Publishing Group.

[93] S. Kumar, J. P. Strachan, and R. S. Williams, "Chaotic dynamics in nanoscale NbO 2 Mott memristors for analogue computing," *Nature*, vol. 548, pp. 318–321, Aug. 2017. Number: 7667 Publisher: Nature Publishing Group.

[94] H.-O. Peitgen, H. Jürgens, and D. Saupe, *Chaos and Fractals: New Frontiers of Science*. Springer, 2nd ed. 2004. softcover reprint of the original 2nd ed. 2004 edition ed., May 2012.

[95] A. M. Turing, "The chemical basis of morphogenesis," *Philosophical Transactions of the Royal Society of London. Series B, Biological Sciences*, vol. 237, pp. 37–72, Aug. 1952. Publisher: Royal Society.

[96] K. Goda and B. Jalali, "Dispersive Fourier transformation for fast continuous single-shot measurements," *Nature Photonics*, vol. 7, pp. 102–112, Feb. 2013. Number: 2 Publisher: Nature Publishing Group.

[97] B. Li, S.-W. Huang, Y. Li, C. W. Wong, and K. K. Y. Wong, "Panoramic-reconstruction temporal imaging for seamless measurements of slowly-evolved femtosecond pulse dynamics," *Nature Communications*, vol. 8, p. 61, July 2017. Number: 1 Publisher: Nature Publishing Group.

[98] L. A. Lugiato and R. Lefever, "Spatial Dissipative Structures in Passive Optical Systems," *Physical Review Letters*, vol. 58, pp. 2209–2211, May 1987. Publisher: American Physical Society.

[99] J. M. Dudley, F. Dias, M. Erkintalo, and G. Genty, "Instabilities, breathers and rogue waves in optics," *Nature Photonics*, vol. 8, pp. 755–764, Oct. 2014. Number: 10 Publisher: Nature Publishing Group.

[100] H. Mori and Y. Kuramoto, *Dissipative Structures and Chaos*. Berlin Heidelberg: Springer-Verlag, 1998.

[101] A. Coillet and Y. K. Chembo, "Routes to spatiotemporal chaos in Kerr optical frequency combs," *Chaos: An Interdisciplinary Journal of Nonlinear Science*, vol. 24, p. 013113, Jan. 2014. Publisher: American Institute of Physics.

[102] A. B. Matsko, W. Liang, A. A. Savchenkov, and L. Maleki, "Chaotic dynamics of frequency combs generated with continuously pumped nonlinear microresonators," *Optics Letters*, vol. 38, pp. 525–527, Feb. 2013. Publisher: Optical Society of America.

[103] D. R. Solli, G. Herink, B. Jalali, and C. Ropers, "Fluctuations and correlations in modulation instability," *Nature Photonics*, vol. 6, pp. 463–468, July 2012. Number: 7 Publisher: Nature Publishing Group.

[104] A. J. Scroggie, W. J. Firth, G. S. McDonald, M. Tlidi, R. Lefever, and L. A. Lugiato, "Pattern formation in a passive Kerr cavity," *Chaos, Solitons & Fractals*, vol. 4, pp. 1323–1354, Aug. 1994.

[105] T. Miyaji, I. Ohnishi, and Y. Tsutsumi, "Bifurcation analysis to the Lugiato–Lefever equation in one space dimension," *Physica D: Nonlinear Phenomena*, vol. 239, pp. 2066–2083, Nov. 2010.

[106] N. Akhmediev and A. Ankiewicz, "Three Sources and Three Component Parts of the Concept of Dissipative Solitons," in *Dissipative Solitons: From Optics to Biology and Medicine*, Lecture Notes in Physics, pp. 1–28, Berlin, Heidelberg: Springer, 2008.

[107] D. R. Solli, C. Ropers, P. Koonath, and B. Jalali, "Optical rogue waves," *Nature*, vol. 450, pp. 1054–1057, Dec. 2007. Number: 7172 Publisher: Nature Publishing Group.

[108] H. Zhou, S.-W. Huang, X. Li, J. F. McMillan, C. Zhang, K. K.-Y. Wong, M. Yu, G.-Q. Lo, D.-L. Kwong, K. Qiu, and C. W. Wong, "Real-time dynamics and cross-correlation gating spectroscopy of free-carrier Drude slow-light solitons," *Light: Science & Applications*, vol. 6, pp. e17008–e17008, June 2017. Number: 6 Publisher: Nature Publishing Group.

[109] T. J. Kippenberg, A. L. Gaeta, M. Lipson, and M. L. Gorodetsky, “Dissipative Kerr solitons in optical microresonators,” *Science*, vol. 361, Aug. 2018. Publisher: American Association for the Advancement of Science Section: Review.

[110] A. L. Gaeta, M. Lipson, and T. J. Kippenberg, “Photonic-chip-based frequency combs,” *Nature Photonics*, vol. 13, pp. 158–169, Mar. 2019. Number: 3 Publisher: Nature Publishing Group.

[111] Y. C. Tong, L. Y. Chan, and H. K. Tsang, “Fibre dispersion or pulse spectrum measurement using a sampling oscilloscope,” *Electronics Letters*, vol. 33, pp. 983–985, May 1997. Publisher: IET Digital Library.

[112] M. A. Muriel, J. Azaña, and A. Carballar, “Real-time Fourier transformer based on fiber gratings,” *Optics Letters*, vol. 24, pp. 1–3, Jan. 1999. Publisher: Optical Society of America.

[113] P. V. Kelkar, F. Coppinger, A. S. Bhushan, and B. Jalali, “Time-domain optical sensing,” *Electronics Letters*, vol. 35, pp. 1661–1662, Sept. 1999. Publisher: IET Digital Library.

[114] C. Bao, J. A. Jaramillo-Villegas, Y. Xuan, D. E. Leaird, M. Qi, and A. M. Weiner, “Observation of Fermi-Pasta-Ulam Recurrence Induced by Breather Solitons in an Optical Microresonator,” *Physical Review Letters*, vol. 117, p. 163901, Oct. 2016. Publisher: American Physical Society.

[115] H. Guo, E. Lucas, M. H. Pfeiffer, M. Karpov, M. Anderson, J. Liu, M. Geiselmann, J. D. Jost, and T. J. Kippenberg, “Intermode Breather Solitons in Optical Microresonators,” *Physical Review X*, vol. 7, p. 041055, Dec. 2017. Publisher: American Physical Society.

[116] C. Bao, L. Zhang, L. C. Kimerling, J. Michel, and C. Yang, “Soliton breathing induced by stimulated Raman scattering and self-steepening in octave-spanning Kerr frequency comb generation,” *Optics Express*, vol. 23, pp. 18665–18670, July 2015. Publisher: Optical Society of America.

[117] P. Del’Haye, A. Coillet, W. Loh, K. Beha, S. B. Papp, and S. A. Diddams, “Phase steps and resonator detuning measurements in microresonator frequency combs,” *Nature Communications*, vol. 6, p. 5668, Jan. 2015. Number: 1 Publisher: Nature Publishing Group.

[118] D. Pierangeli, M. Flammini, L. Zhang, G. Marcucci, A. Agranat, P. Grinevich, P. Santini, C. Conti, and E. DelRe, “Observation of Fermi-Pasta-Ulam-Tsingou Recurrence and Its Exact Dynamics,” *Physical Review X*, vol. 8, p. 041017, Oct. 2018. Publisher: American Physical Society.

[119] M. Guasoni, J. Garnier, B. Rumpf, D. Sugny, J. Fatome, F. Amrani, G. Millot, and A. Picozzi, “Incoherent Fermi-Pasta-Ulam Recurrences and Unconstrained Thermalization Mediated by Strong Phase Correlations,” *Physical Review X*, vol. 7, p. 011025, Mar. 2017. Publisher: American Physical Society.

[120] P. A. E. M. Janssen, “Modulational instability and the Fermi-Pasta-Ulam recurrence,” *The Physics of Fluids*, vol. 24, pp. 23–26, Jan. 1981. Publisher: American Institute of Physics.

[121] H. Guo, M. Karpov, E. Lucas, A. Kordts, M. H. P. Pfeiffer, V. Brasch, G. Lihachev, V. E. Lobanov, M. L. Gorodetsky, and T. J. Kippenberg, "Universal dynamics and deterministic switching of dissipative Kerr solitons in optical microresonators," *Nature Physics*, vol. 13, pp. 94–102, Jan. 2017. Number: 1 Publisher: Nature Publishing Group.

[122] C. Guedes Soares, Z. Cherneva, and E. Antão, "Characteristics of abnormal waves in North Sea storm sea states," *Applied Ocean Research*, vol. 25, pp. 337–344, May 2004.

[123] Y. Chembo Kouomou, P. Colet, L. Larger, and N. Gastaud, "Chaotic Breathers in Delayed Electro-Optical Systems," *Physical Review Letters*, vol. 95, p. 203903, Nov. 2005. Publisher: American Physical Society.

[124] V. V. Mirnov, A. J. Lichtenberg, and H. Guclu, "Chaotic breather formation, coalescence, and evolution to energy equipartition in an oscillatory chain," *Physica D: Nonlinear Phenomena*, vol. 157, pp. 251–282, Oct. 2001.

[125] M. Hopkin, "Sea snapshots will map frequency of freak waves," *Nature*, vol. 430, pp. 492–492, July 2004. Number: 6999 Publisher: Nature Publishing Group.

[126] A. F. J. Runge, C. Aguergaray, N. G. R. Broderick, and M. Erkintalo, "Raman rogue waves in a partially mode-locked fiber laser," *Optics Letters*, vol. 39, pp. 319–322, Jan. 2014. Publisher: Optical Society of America.

[127] M. A. Foster, R. Salem, D. F. Geraghty, A. C. Turner-Foster, M. Lipson, and A. L. Gaeta, "Silicon-chip-based ultrafast optical oscilloscope," *Nature*, vol. 456, pp. 81–84, Nov. 2008. Number: 7218 Publisher: Nature Publishing Group.

[128] D. H. Broaddus, M. A. Foster, O. Kuzucu, A. C. Turner-Foster, K. W. Koch, M. Lipson, and A. L. Gaeta, "Temporal-imaging system with simple external-clock triggering," *Optics Express*, vol. 18, pp. 14262–14269, June 2010. Publisher: Optical Society of America.

[129] P. Suret, R. E. Koussaifi, A. Tikan, C. Evain, S. Randoux, C. Szwaj, and S. Bielawski, "Single-shot observation of optical rogue waves in integrable turbulence using time microscopy," *Nature Communications*, vol. 7, p. 13136, Oct. 2016. Number: 1 Publisher: Nature Publishing Group.

[130] P. Grelu and N. Akhmediev, "Dissipative solitons for mode-locked lasers," *Nature Photonics*, vol. 6, pp. 84–92, Feb. 2012. Number: 2 Publisher: Nature Publishing Group.

[131] M. Yu, J. K. Jang, Y. Okawachi, A. G. Griffith, K. Luke, S. A. Miller, X. Ji, M. Lipson, and A. L. Gaeta, "Breather soliton dynamics in microresonators," *Nature Communications*, vol. 8, p. 14569, Feb. 2017. Number: 1 Publisher: Nature Publishing Group.

[132] Y. K. Chembo, D. Gomila, M. Tlidi, and C. R. Menyuk, "Theory and applications of the Lugiato-Lefever Equation," *The European Physical Journal D*, vol. 71, p. 299, Nov. 2017.

[133] S. A. Mikhailov and K. Ziegler, "New Electromagnetic Mode in Graphene," *Physical Review Letters*, vol. 99, p. 016803, July 2007. Publisher: American Physical Society.

[134] G. W. Hanson, "Dyadic Green's functions and guided surface waves for a surface conductivity model of graphene," *Journal of Applied Physics*, vol. 103, p. 064302, Mar. 2008. Publisher: American Institute of Physics.

[135] S. Lee, "Colloidal superlattices for unnaturally high-index metamaterials at broadband optical frequencies," *Optics Express*, vol. 23, pp. 28170–28181, Nov. 2015. Publisher: Optical Society of America.

[136] L. Yang, C. Pei, A. Shen, C. Zhao, Y. Li, X. Li, H. Yu, Y. Li, X. Jiang, and J. Yang, "An all-optical modulation method in sub-micron scale," *Scientific Reports*, vol. 5, p. 9206, Mar. 2015. Number: 1 Publisher: Nature Publishing Group.

[137] B. C. Yao, Y. J. Rao, Z. N. Wang, Y. Wu, J. H. Zhou, H. Wu, M. Q. Fan, X. L. Cao, W. L. Zhang, Y. F. Chen, Y. R. Li, D. Churkin, S. Turitsyn, and C. W. Wong, "Graphene based widely-tunable and singly-polarized pulse generation with random fiber lasers," *Scientific Reports*, vol. 5, p. 18526, Dec. 2015. Number: 1 Publisher: Nature Publishing Group.

[138] S. Seki, S. Tsuzuki, K. Hayamizu, Y. Umebayashi, N. Serizawa, K. Takei, and H. Miyashiro, "Comprehensive Refractive Index Property for Room-Temperature Ionic Liquids," *Journal of Chemical & Engineering Data*, vol. 57, pp. 2211–2216, Aug. 2012. Publisher: American Chemical Society.

[139] V. Sorianello, G. D. Angelis, T. Cassese, M. Midrio, M. Romagnoli, M. Mohsin, M. Otto, D. Neumaier, I. Asselberghs, J. V. Campenhout, and C. Huyghebaert, "Complex effective index in graphene-silicon waveguides," *Optics Express*, vol. 24, pp. 29984–29993, Dec. 2016. Publisher: Optical Society of America.

[140] W. Du, E.-P. Li, and R. Hao, "Tunability Analysis of a Graphene-Embedded Ring Modulator," *IEEE Photonics Technology Letters*, vol. 26, pp. 2008–2011, Oct. 2014. Conference Name: IEEE Photonics Technology Letters.

[141] A. T. Bollinger, G. Dubuis, J. Yoon, D. Pavuna, J. Misewich, and I. Božović, "Superconductor–insulator transition in La 2 - x Sr x CuO 4 at the pair quantum resistance," *Nature*, vol. 472, pp. 458–460, Apr. 2011. Number: 7344 Publisher: Nature Publishing Group.

[142] K. Srinivasan and O. Painter, "Linear and nonlinear optical spectroscopy of a strongly coupled microdisk–quantum dot system," *Nature*, vol. 450, pp. 862–865, Dec. 2007. Number: 7171 Publisher: Nature Publishing Group.

[143] S. Gröblacher, K. Hammerer, M. R. Vanner, and M. Aspelmeyer, "Observation of strong coupling between a micromechanical resonator and an optical cavity field," *Nature*, vol. 460, pp. 724–727, Aug. 2009. Number: 7256 Publisher: Nature Publishing Group.

[144] J. Zhu, S. K. Ozdemir, Y.-F. Xiao, L. Li, L. He, D.-R. Chen, and L. Yang, "On-chip single nanoparticle detection and sizing by mode splitting in an ultrahigh- Q microresonator," *Nature Photonics*, vol. 4, pp. 46–49, Jan. 2010. Number: 1 Publisher: Nature Publishing Group.

[145] E. Hendry, P. J. Hale, J. Moger, A. K. Savchenko, and S. A. Mikhailov, “Coherent Nonlinear Optical Response of Graphene,” *Physical Review Letters*, vol. 105, p. 097401, Aug. 2010. Publisher: American Physical Society.

[146] Y. Wu, B. C. Yao, Q. Y. Feng, X. L. Cao, X. Y. Zhou, Y. J. Rao, Y. Gong, W. L. Zhang, Z. G. Wang, Y. F. Chen, and K. S. Chiang, “Generation of cascaded four-wave-mixing with graphene-coated microfiber,” *Photonics Research*, vol. 3, pp. A64–A68, Apr. 2015. Publisher: Optical Society of America.

[147] K. J. A. Ooi, L. K. Ang, and D. T. H. Tan, “Waveguide engineering of graphene’s nonlinearity,” *Applied Physics Letters*, vol. 105, p. 111110, Sept. 2014. Publisher: American Institute of Physics.

[148] K. Alexander, N. A. Savostianova, S. A. Mikhailov, B. Kuyken, and D. Van Thourhout, “Electrically Tunable Optical Nonlinearities in Graphene-Covered SiN Waveguides Characterized by Four-Wave Mixing,” *ACS Photonics*, vol. 4, pp. 3039–3044, Dec. 2017. Publisher: American Chemical Society.

[149] D. V. Skryabin and A. V. Gorbach, “Colloquium: Looking at a soliton through the prism of optical supercontinuum,” *Reviews of Modern Physics*, vol. 82, pp. 1287–1299, Apr. 2010. Publisher: American Physical Society.

[150] M. Erkintalo, Y. Q. Xu, S. G. Murdoch, J. M. Dudley, and G. Genty, “Cascaded Phase Matching and Nonlinear Symmetry Breaking in Fiber Frequency Combs,” *Physical Review Letters*, vol. 109, p. 223904, Nov. 2012. Publisher: American Physical Society.

[151] A. Coillet, I. Balakireva, R. Henriet, K. Saleh, L. Larger, J. M. Dudley, C. R. Menyuk, and Y. K. Chembo, “Azimuthal Turing Patterns, Bright and Dark Cavity Solitons in Kerr Combs Generated With Whispering-Gallery-Mode Resonators,” *IEEE Photonics Journal*, vol. 5, pp. 6100409–6100409, Aug. 2013. Conference Name: IEEE Photonics Journal.

[152] S. Wabnitz, “Suppression of interactions in a phase-locked soliton optical memory,” *Optics Letters*, vol. 18, pp. 601–603, Apr. 1993. Publisher: Optical Society of America.

[153] P. Parra-Rivas, D. Gomila, M. A. Matías, S. Coen, and L. Gelens, “Dynamics of localized and patterned structures in the Lugiato-Lefever equation determine the stability and shape of optical frequency combs,” *Physical Review A*, vol. 89, p. 043813, Apr. 2014. Publisher: American Physical Society.

[154] M. Peccianti, A. Pasquazi, Y. Park, B. E. Little, S. T. Chu, D. J. Moss, and R. Morandotti, “Demonstration of a stable ultrafast laser based on a nonlinear microcavity,” *Nature Communications*, vol. 3, p. 765, Apr. 2012. Number: 1 Publisher: Nature Publishing Group.

[155] Y. Liu, R. Cheng, L. Liao, H. Zhou, J. Bai, G. Liu, L. Liu, Y. Huang, and X. Duan, “Plasmon resonance enhanced multicolour photodetection by graphene,” *Nature Communications*, vol. 2, p. 579, Dec. 2011. Number: 1 Publisher: Nature Publishing Group.

[156] T. Fujimoto and K. Awaga, "Electric-double-layer field-effect transistors with ionic liquids," *Physical Chemistry Chemical Physics*, vol. 15, pp. 8983–9006, May 2013. Publisher: The Royal Society of Chemistry.

[157] T. Sato, T. Morinaga, S. Marukane, T. Narutomi, T. Igarashi, Y. Kawano, K. Ohno, T. Fukuda, and Y. Tsujii, "Novel Solid-State Polymer Electrolyte of Colloidal Crystal Decorated with Ionic-Liquid Polymer Brush," *Advanced Materials*, vol. 23, no. 42, pp. 4868–4872, 2011. _eprint: https://onlinelibrary.wiley.com/doi/pdf/10.1002/adma.201101983.

[158] B. Li, Y. Wei, J. Kang, C. Zhang, and K. K. Y. Wong, "Parametric spectrotemporal analyzer based on four-wave mixing Bragg scattering," *Optics Letters*, vol. 43, pp. 1922–1925, Apr. 2018. Publisher: Optical Society of America.

[159] L. Chen, Y. Duan, H. Zhou, X. Zhou, C. Zhang, and X. Zhang, "Real-time broadband radio frequency spectrum analyzer based on parametric spectro-temporal analyzer (PASTA)," *Optics Express*, vol. 25, pp. 9416–9425, Apr. 2017. Publisher: Optical Society of America.

[160] A. Benetazzo, F. Ardhuin, F. Bergamasco, L. Cavaleri, P. V. Guimarães, M. Schwendeman, M. Sclavo, J. Thomson, and A. Torsello, "On the shape and likelihood of oceanic rogue waves," *Scientific Reports*, vol. 7, p. 8276, Aug. 2017. Number: 1 Publisher: Nature Publishing Group.

[161] A. Mathis, L. Froehly, S. Toenger, F. Dias, G. Genty, and J. M. Dudley, "Caustics and Rogue Waves in an Optical Sea," *Scientific Reports*, vol. 5, p. 12822, Aug. 2015. Number: 1 Publisher: Nature Publishing Group.